FINAL TECHNICAL REPORT
MAY 21 - NOVEMBER 20, 1991

DEFINITION OF THE UNSTEADY VORTEX FLOW OVER A WING/BODY CONFIGURATION

S.G Liou, B. deBry, J. Lenakos, J. Caplin, N.M. Komerath
School of Aerospace Engineering
Georgia Institute of Technology
Atlanta, GA 30332-0150.
404-894-3017

GITAER 91-6

NOVEMBER 20, 1991

Table of Contents

Nomenclature

b	Model wing span
f	frequency, Hz
f_{NQ}	Nyquist frequency
f_{LO}	Low-pass frequency
G(f)	Spectral density function
H	Helicity, defined as scalar product of local velocity and vorticity vectors
H_O	Reference helicity, based on freestream velocity and wing span
U_∞	Freestream velocity
U	Streamwise component of local velocity, positive toward downstream
U_{mean}	Averaged streamwise component of local velocity
U_{rms}	Streamwise component of local root-mean-square velocity
V	Spanwise component of local velocity, positive toward right as viewing upstream
V_{rms}	Spanwise component of local root-mean-square velocity
W	Vertical component of local velocity, positive upward
W_{rms}	Vertical component of local root-mean-square velocity
X	Model streamwise coordinate along body axis, positive toward rear with origin at body nose-tip.
Y	Model spanwise coordinate, positive toward left as viewing upstream
ΔY	Difference of Y position in vortex trajectory
y	Local spanwise coordinate, positive toward left as viewing upstream with origin at centerline on the wing surface
Z	Model vertical coordinate, positive upward
ΔZ	Difference of Z position in vortex trajectory
z	Local vertical coordinate, positive upward

Greek

α Model angle of attack

ω Vorticity

ω_O Reference vorticity, based on freestream velocity and wing span

Abbreviation

HW   Hot-wire

LDV   Laser Doppler Velocimeter

LHS   Left-hand-side, viewing upstream

RHS   Right-hand-side, viewing upstream

RMS   Root-mean-square

SUMMARY

A problem of current interest in computational aerodynamics is the prediction of unsteady vortex flows over aircraft at high angles of attack. A six-month experimental effort was conducted at the John J. Harper Wind Tunnel to acquire qualitative and quantitative information on the unsteady vortex flow over a generic wing-body configuration at high angles of attack. A double-delta flat-plate wing with beveled edges was combined with a slender sharp-nosed body-of-revolution fuselage to form the generic configuration. This configuration produces a strong attached leading edge vortex on the wing, as well as sharply-peaked flow velocity spectra above the wing. While it thus produces flows with several well-defined features of current interest, the model was designed for efficiency of representation in computational codes. A moderate number of surface pressure ports and two unsteady pressure sensors were used to study the pressure distribution over the wing and body surface at high angles of attack; the unsteady pressure sensing did not succeed because of inadequate signal-to-noise ratio. A pulsed copper vapor laser sheet was used to visualize the vortex flow over the model, and vortex trajectories, burst locations, mutual induction of vortex systems from the forebody, strake, and wing, were quantified. Laser Doppler velocimetry was used to quantify all 3 components of the time-averaged velocity in 3 data planes perpendicular to the freestream direction. Statistics of the instantaneous velocity were used to study intermittency and fluctuation intensity. Hot-film anemometry was used to study the fluctuation energy content in the velocity field, and the spectra of these fluctuations. In addition, a successful attempt was made to measure velocity spectra, component by component, using laser velocimetry, and these were compared with spectra measured by hot-film anemometry at several locations.

DEFINITION OF THE UNSTEADY VORTEX FLOW OVER A WING/BODY CONFIGURATION

S.G Liou[1], B. deBry[2], J. Lenakos[3], J. Caplin[2], N.M. Komerath[4]
School of Aerospace Engineering
Georgia Institute of Technology
Atlanta, GA 30332-0150.

1. INTRODUCTION

At high angles of attack the highly swept leading edge extensions, the sharp wing leading edge, and slender fuselage forebodies of modern high-speed aircraft generate vortices which produce substantial increases in lift and may be used to perform some maneuvers. High-Speed Civil Transport designs, on the other hand, may expect to encounter the high-α environment as well, because of the need to reduce landing speed. Many modern designs have control surfaces set away from the longitudinal plane of symmetry, so that these surfaces are immersed, partly or totally, in the vortex flow coming off the wings under such flight conditions. This has some significant benefits, but also appears to cause some severe problems.

Over the past two years, the Georgia Institute of Technology has conducted detailed studies on F-15 models[1,2] to define the high angle of attack flow environment of the vertical tails. Measurements and data found in the literature showed that the flow field develops sharply-peaked spectra in the vicinity of the vertical tails. The dominant frequency showed accurate Strouhal scaling to the observed oscillation frequencies on the full-scale vertical tails. Similar phenomena were also observed above the vertical tails of the F-18 outside the severe burst-vortex buffeting region. These results led to the preliminary testing of a generic, highly swept wing/body configuration[2]. It was found that this configuration exhibits similar sharp-peaked spectra in the region where the vertical tails would be mounted. This proved that the occurrence of such sharp peak spectra are fluid dynamic in origin and do not depend on such geometric details as inlets, or on feedback from the tails.

1: Post-Doctoral Fellow

2: Graduate Research Assistant

3: Undergraduate Student

4: Associate Professor

Computation of unsteady high-α flows over entire configurations is a current objective of computational fluid dynamics[3,4]. Measurements cannot be obtained at all possible flight conditions, so that computer simulations are needed to fill in the gaps and enable first-principles-based prediction at the preliminary design stage. However, before confident use of these numerical tools can be made, the computer codes must be fine tuned and validated. Validation requires multi-faceted data sets, so that the causes of problems can be tracked down conclusively. Thus, there arose a separate need for high-quality, detailed data to prove the predictions of the computational codes. These considerations provided motivation for the present research to obtain quantitative data on vortex behavior and velocity field over a configuration amenable to efficient computation. It also allows for the study of the development of quasi-periodic unsteadiness in the flow above a swept-wing configuration at high angles of attack.

It is quite expensive to run computational codes which can resolve unsteady velocity fluctuations and explore their nature in the high angle-of-attack flowfield. If such codes must be validated using data from realistic aircraft configurations, a great deal of resources must be devoted to accurate modeling of the detailed geometry of such configurations. These detract from resources which can otherwise be devoted to resolving flow features accurately. Thus we used a configuration which would produce the flow features of interest, yet requires minimal computational resources. Happily, such a configuration is also less expensive and more efficient to build, instrument, and use for flowfield measurements.

2. FACILITY

All the tests were performed in John J. Harper Wind Tunnel at Georgia Tech, which is a closed loop tunnel with a seven by nine foot test section. The tunnel is powered by a 600 hp motor, which can generate continuous air flow with speed up to 175 mph. Honeycomb and fine-mesh screen were installed in the settling chamber to assure good flow quality. A variety of flow diagnostic systems are available in the facility, which make multi-faceted study of the subject possible. A diagram of the facility is shown in Fig. 2.1.

3. EXPERIMENTAL PROCEDURES

3.1 Model Construction

The design of the generic wing/body model was determined based on several reasons listed below:

1) The shape originated with a small wooden model with flat-plate aluminum wings tested a few years ago[5] at the 42" low turbulence tunnel at the School of Aerospace Engineering. This shape was chosen because we had already obtained preliminary data on it and confirmed the existence of quasi-periodic velocity fluctuations above it, and because it was representative of a "generic" supersonic civil transport. The double-swept delta wing, consisting of a sharply-swept strake extension in front of the delta wing, was chosen. The strake will generate a strong attached vortex, which can be visualized for a considerable distance over the wing and is likely to exhibit vortex burst phenomena. A large leading edge vortex structure will be produced by the delta wing. Previous measurements have shown that such configurations will generate quasi-periodic velocity fluctuations in the downstream portion of the wing flowfield, as well as near the vertical tail. Therefore, this simplified model will provide a comparison toward a better understanding of this unsteady vortex flowfield.

2) More efficient computation can be achieved with simple configuration because of the reduction of resources devoted to complex modeling. It is more suitable at the initial development and validation stage of the code.

The generic wing/body model, scaled up 1.5 times from the small wooden model, was built at the machine shop at the School of Aerospace Engineering. Fig3.1 shows the geometry and dimensions of the model. The wing section was made of steel plate for rigidity at high angle of attack. The upper surface of the wing is flat with the lower surface being beveled. The thickness of the wing is 0.25 inch. This leaves a space of 0.125 inch between upper and lower surface, which allows the installation of 1/16" stainless steel tubes and Kulite pressure transducers for static and dynamic pressure measurements. Aluminum pipe was used for the body with forebody and aft-body being turned from wood and hollowed out inside. The wing surface was painted flat black to reduce laser scattering, and a fluorescent orange strip was added along the edges to make the model outline visible in a darkened test section. The model can also be dismantled and tested as wing-alone, or body-alone, besides the full wing-body.

The model was mounted on a sliding platform through a supporting mechanism, (camera tripod head) which allowed adjustment of pitch, roll, and yaw angles. The

3

platform rode on two rails fixed on the tunnel floor, and was moved using a lead screw driven by a computer-controlled stepper motor. The traverse mechanism was calibrated. Fig.3.2 shows a sketch of the model inside the test section.

3.2 Onset Velocity Field

Hot-wire anemometry was used to measure the turbulence intensity at several locations upstream of the model location in the test section. Smoke wires used for the flow visualization were also installed, so that their effects on the flow field could be checked. Measurements were made at two freestream speeds (20 ft/sec and 50 ft/sec), at which most of the later tests were conducted. Results showed that the turbulent intensity in both cases was in the range of 0.1 to 0.2%.

3.3 Laser Sheet Flow Visualization

Flow visualization was performed first in order to determine the vortex trajectory and understand the flow field features. The results were then used to help choose the measuring planes and locations for the subsequent tests. During the flow visualization, the model was moved at constant speed through the light sheet. Smoke patterns over the model surface were recorded using a video camera fixed downstream of the test section, inside the tunnel. Tests were repeated for several angles of attack (10,15,20,25 deg.). Freestream speed was chosen to be 20 ft/sec based on the picture quality from the video camera and the time that the smoke wire could last. As wind speed increased, seeding particles from the smoke wires mixed up more rapidly and produced a more uniformly distributed environment, which made the vortex structure difficult to distinguish on the video. At higher speeds, this happened too quickly to permit traversal of the whole model through the light sheet before the image quality became unusable. Tests with different wind speeds at the same angle of attack were therefore conducted to check the effect of speed on vortex trajectory. Model deflection under different speeds was also checked to determine the angle of attack correction required.

Light sheet set up

The light source for the flow visualization was a 30 watt copper vapor pulsed laser. The beam from the laser was coupled into an optical fiber and sent to the sheet generator to form a thin sheet. Initially, the light sheet was sent in from the upper window of the test section. Later it was moved above the roof of the wind tunnel and pointed down so that the sheet was symmetric about the model axis. Fig.3.3 shows the set up inside the tunnel.

4

Seeding

Five horizontal nichrome wires were strung across the upstream end of the test section. A cotton thread was wound loosely over each wire, and painted with molten wax. A power amplifier outside the test section allowed the operator to control the current through the wires and thus the smoke generation. The smoke could be made to last from several seconds to several minutes depending upon the current applied.

Recording and analysis

The flow images were captured by a Sony V-101 Hi8 camcorder placed inside the wind tunnel and downstream of the model. The video output was transmitted to a Panasonic AG1460 video recorder and recorded onto VHS tape. Before each test started, a piece of cardboard marked with one inch square grid was held in the light sheet plane (with the laser off). This was recorded on videotape with the camcorder fixed in position. After removing the cardboard, the model was positioned so that the tip of the nose barely touched the laser sheet plane.

The test results were analyzed on an Apple Macintosh II computer with a RasterOps 364 Colorboard frame grabber/display unit. Images were digitized onto Mac II through the FrameGrabber software provided by RasterOps. A calibration grid was generated on the computer with a drawing program (Deneba CANVAS 2.0), and compared with the digitized image of the recorded grid to assure accuracy. The grid was then overlaid on each digitized image, and the vortex core location was marked onto the grid. When a clear vortex core could no longer be seen due to vortex bursting at aft stations of the model, the approximate center of the vortical flow structure was marked. When all the marks were collected, the CANVAS software and an in-house code were used to measure the distances between the mark and the reference nosetip. The position of the cross-flow plane with respect to the nosetip was measured using the time display on each digitized image, since the model was moving at a constant speed. The (X, Y, Z) coordinates of each mark with respect to the body axes were thus determined, and the trajectory of the center of the vortex system was plotted.

3.4 Flow Field Spectral Analysis

A hot-film anemometer (TSI Model 1210-20 sensor) was used to study the spectra of velocity fluctuations at different locations , with varying speeds and angles of attack. The purpose of this study was to determine whether a dominant frequency exists above the

wing or close to the possible location of vertical tail, and how it varies with different test conditions.

Data acquisition and processing

A single-film sensor was calibrated before the test to obtain the non-linear relation between output voltage and freestream speed determined from the pitot-static probe. During the test, the signal from the anemometer was sent through two channels into the 16-bit high speed Preston analog-to-digital converter attached to the HP1000 A700 computer system. The signal to the first channel was digitized without modification except for a low-pass anti-aliasing filter and provided the full raw information. The same signal was also routed through a T connector and high-pass filtered set at 0.1 Hz, so that the steady part was discarded. The fluctuating part was then amplified at a desired gain so that the signal level was optimized for accurate digitization. This signal was then low-pass filtered, before sampling through second channel. Each sample block consisted of 512 samples, which were converted to units of velocity using the full non-linear calibration results. At each measuring point, 100 such sample blocks were used to find stable, averaged auto-spectra of the velocity fluctuation, and the spectra were obtained with higher bandwidth to ensure that high frequency phenomena were not being missed. It should be noted that the hot-film sensor cannot distinguish contributions from different velocity components, and cannot resolve flow reversal, if any.

3.5 Velocity Field Mapping

The LDV system used here is a 5 Watt Argon ion laser with frequency shifter and a 3-axis computerized traverse. The traverse has a range of 48"x30"x30", sufficient to cover the aircraft model without moving and realigning the LDV. Although the LDV is a two component system, it was set up for one component measurement in this case. The complexity involved in the alignment of two component system and the quality of the signals made it far more efficient to measure one component at a time. The price paid is that Reynolds' stresses and other joint statistics are out of reach. The U and W velocity components were acquired by rotating the optics through 90 degrees as needed. However, the third component, V, required a new design of the model support mechanism to roll the model 90 degrees in order to complete the measurements. Positional accuracy in this measurement process is essentially the same as the measuring volume size: approximately 0.1 mm at all points, assuming the traverse coordinates were linked to the body axis coordinates and were checked before and after each run.

Seeding particles were generated by atomizing mineral oil downstream of the test section. The data rate during the measurements was in the neighborhood of 3000 per second for most of the measuring points. Three measuring planes were chosen to define the flowfield in front of the strake-wing junction, over the wing and at the trailing edge of the wing, where vertical tails might be located. Fig.3.4 shows the location and area covered for these three measuring planes with respect to the model. An increment of 0.5 inch was used for the grid at station 2 and 3, while a finer increment of 0.25 inch was used for grid at station 1. At each measuring point, 10000 data were sampled and averaged to find the mean and rms (root-mean-square) values.

3.6 Static Pressure Measurement

The static pressure measurement over the wing surface can provide numerical codes with validation data for loading predictions. It also can be correlated with flow visualization and velocity data to portray a better picture of the flow field. Forty-one pressure taps were installed on the model as shown in Fig.3.6. Each tap was connected to the 48-channel Scanivalve switch with plastic Tygon tubing, and then the Barocell pressure transducer. Leak checks were performed prior to the test to ensure correct pressure readings. An in-house computer program was used to step through the scanivalve channels. At each pressure tap, the software checked the readings and optimized the amplification on the signla conditionere for optimal accuracy. Delays were built into this code to ensure that readings were acquired only after the pneumatic switching transients had died down. One hundred data blocks with 500 values per block were sampled and averaged to find the Cp value at each pressure tap. These tests were repeated for 4 angles of attack (10,15,25,35 deg.) under 3 different freestream speeds (20,50,80 ft/sec).

4. RESULTS AND DISCUSSION

4.1 Laser Sheet Flow Visualization

Model deflection

In order to ensure the accuracy of the model angle of attack, a model deflection test was done prior to the flow visualization. Freestream speed was increased from 20 ft/sec to 100 ft/sec. The deflection of model at each speed was measured using the video system (with the camera mounted outside the test section in this case). A single laser beam from the Argon laser was placed at the tip of the nose before the tunnel was turned on, and was moved using the stepper-motor traverse until it hit the nose again at a different speed. Fig.4.1 shows the result from this test, which indicates that no deflection happened before

50 ft/sec. Deflection increased non-linearly to 0.6 inches under 100 ft/sec, but is still negligible.

Asymmetry

All of the flow images shown in this report are copies of 8-bit gray-scale printouts from the original digitized color video. Much of the detail is lost in the process; the authors will be glad to provide color prints, videotape, and/or digitized images on disk to interested readers. Fig.4.2 shows vortex patterns above the wing, moving downstream. Contrary to appearance, it should be remembered that we are seeing a section of smoke which started out upstream as several horizontal wakes. Thus, if there were no disturbance at all, we would expect to see five distinct, slightly-thick horizontal bands. The bright spot is laser scattering off the black-painted model surface: these images were acquired with the light coming through one of the upper test section windows. The patterns are seen to be extremely asymmetric.

A variety of causes of the asymmetry were suspected and checked. Model yaw and roll angle were rechecked several times; the test section windows were removed and put back in; the probe traverse inside the test section was moved upstream and downstream with the model fixed in position; the wing was checked, and the seams were faired over with modeling wax. However, none of these resolved the problem. Finally, attention was directed to the nose. Fig.4.3 shows the result: the asymmetry clearly originated at the nose in the forebody vortex system. A minor asymmetry was observed at the very tip of the nose, and this amplified downstream due to the mutual induction effects of the vortex systems from the two sides. When the asymmetry at the nose was removed by fairing over with modeling wax, things improved vastly. Fig.4.4 and 4.5 show the vortex patterns over several different stations along the model after modification. Improvement can be clearly seen.

Vortex trajectory

As shown in Fig.4.6, two vortices appeared from the forebody early on, located on the upper side of the nose cone. At the beginning of the strake, two more vortices formed. The forebody vortices were then gradually brought downward and incorporated into the strake vortices over some finite distance, typically six inches. At the strake-wing junction, two more vortices joined the vortex system. At moderate angles of attack, a merging of the wing and strake vortices was visible; we suspect that these effects are present at other angles of attack as well. Unlike the interaction of the strake and forebody

8

vortices, where the strake vortices were dominant, the strake and wing vortices appeared to mix together rather evenly. However, the movement of the wing vortices was quite different from that of the forebody vortices. Maintaining a lower height above the model than the strake vortices, the wing vortices gradually advanced inward from the leading edge towards the strake vortices while slightly rising in height. At the instance of their superposition, the wing vortex abruptly reached a height above the strake vortex and joined with it. This occurrence took place over a distance of one inch and finished within roughly three inches, which is notably less than the previous case (the strake/forebody interaction). The final two vortices proceeded along the model continually growing in size and distance from the body centerline. At moderate to high angles of attack, the vortices became burst at a location of approximately 56% of the model length.

Figs.4.7 through 4.10 show the vortex trajectories at several angles of attack. At 10 deg., the core trajectory was marked from the strake, as the forebody vortices were no longer visible. It is at this angle where visual presence of the wing-strake vortex transition is available. Slight instability was noticed at 15 deg. The forebody-strake vortex transition, which is characterized by a drop in height and an increase in spanwise distance from the centerline, was seen to be prolonged at this angle in comparison to the other angles. At 20 deg., spanwise symmetry was very good. Abruptness of the forebody-strake vortex transition was noted as compared with 15 deg. Results at 25 deg. were very similar to those at 20 deg. except that vortex transition occurred slightly later, which might be due to the slight difference in freestream speed.

Spanwise symmetry of the vortex trajectories was compared for angles of 10,15, and 20 degrees. Results are shown in Fig.4.11 through 4.13. The trajectories were obtained totally independently. The averaged difference is found to be roughly 0.34 inch, which is quite small.

Speed comparison test

Because of the difference in freestream speed chosen for the flow visualization and LDV measurement, it is interesting to know the effect of different speeds on the vortex trajectory. To avoid smoke generator burnout (which occurred several times), only three stationary locations, where LDV measurements were performed, were chosen for the comparison test. The information shown in Fig.4.14 represents a general trend seen in the test. The figures have been curve fit and labeled according to their corresponding sides. As shown in the figures, at higher freestream velocity the vortex core formed slightly closer

9

to the centerline, and increased in spanwise distance at a faster rate than at lower speed. The maximum difference was found to be approximately eight tenths of an inch. While the difference in Z direction followed the same trend, only three tenths of an inch maximum difference was noted.

Error analysis

Human factors, model setup, and computer hardware/software limitation were all included in the analysis. The possible error in position of vortex core was then estimated as given below:

$\pm$ 0.25 inch from the nose to the forebody strake

$\pm$ 0.4 inch error in each point beyond the forebody strakes to 56% of the model

$\pm$ 1.2 inch error after 56% of the model

The last value is a function of burst vortices, which causes a greater error, because the "center" of the vortical flow must now be located by the operator.

4.2 Laser Doppler Velocimetry

Velocity field

Figure 4.15 shows all 3 velocity components measured at three different planes. Cross flow components V and W are presented in vector form with the axial component delineated by flooded contours. These figures were made using TecPlot™ on an Intel80386-class GATEWAY2000 computer, and printed on an HP laser printer. The body boundary is indicated by a white circular strip at the lower right corner with the wing surface at line z=0. It is clear that the vortical structure is the dominant feature at all the stations. However, the characteristics at stations 1 and 2 are totally different from station 3. At station 1, which was located in front of the strake-wing junction, a tightly wound vortex can be easily identified. The axial velocity inside the core region went up to almost three times the freestream speed. Underneath the vortex core, few vectors are missing, which are not because of surface scattering, but the extremely low data rate. From observations of the Doppler signal on the oscilloscope during the test, very strong fluctuations in the V component including change in direction had occurred. Flow visualization results showed that the forebody vortex had been drawn downward and into the strake vortex in this region. Yet, from the direction of velocity vectors in this region, a secondary vortex with opposite sense of rotation may exist there, which could have originated from the flow separation induced by the strong strake vortex. Therefore, the flowfield around this station was actually very complicated. Moving downstream to station

10

2, which was above the fore portion of the wing, the basic flow features were similar to station 1. However, the vortical structure seems to be flattened and enlarged with slightly decreased axial velocity, indicating that transition to vortex burst might already have begun in front of this station. Interaction between the wing leading edge vortex and strake vortex was active in this region. At station 3, located close to the trailing edge of the wing, the flow features are very different. Burst of the strake-wing vortex is obvious. All the vortices from different sources are no longer distinct, but form a large swirling vortical flow structure. Reverse flow can now be observed in the center of this vortical flow. Velocity variation at this station was much smoother than in the other two cases. One thing common to all three stations is that they all had strong downflow close to the body centerline, compared to the upflow at the wing leading edge. In addition, the center of the vortical structure for all stations compares very well with the flow visualization results if differences in freestream speed are taken into account.

Vorticity/helicity contours

Fig.4.16 shows the vorticity contours at different stations. Vortex sheet roll-up and the formation of a concentrated vortex can be clearly seen at the first two stations. A vortex with an opposite sense of rotation is observed underneath the primary vortex. The strength of the vortices at station 1 was roughly 3 times greater than at station 2. Once the vortex completely burst, as at station 3, the vortex strength dropped substantially.

A better way to visualize the vortex structure, as suggested by other researchers[4], is using helicity contours. Helicity is defined as the dot product of vorticity and velocity. Only the X component of vorticity was used in the calculation here. Fig.4.17 shows the results from this calculation. A more lucid picture of the vortex system is obtained through this method, especially for station 3, where the roll-up vortex sheet and the burst vortex can now be distinguished without ambiguity. Flow reversal causes the sign change in the central region. Such flow reversal in the burst core has been observed by Sellers et al[6]; however, their measurements on the YF-17 showed flow reversal even in the time-averaged results.

Root-mean-square velocity fluctuation

In order to understand the unsteadiness in the flowfield, which is not seen in Fig.4.15, the root-mean-square velocity fluctuations of all three components are shown separately in Fig.4.18, 4.19 and 4.20. Several interesting points can be observed: 1) fluctuation levels were higher at the first two stations, where the vortex strength was much

11

higher and interactions between vortices were so vigorous; 2) for the U component, the region of highest unsteadiness matches well with the region where the vortex core or center of the vortical structure is located; 3) however, for the V and W components, this is no longer the case. At the first two stations, the region of highest unsteadiness moved inboard and/or downward from the core/center region, which may be related to the severe interactions occurring in the area. On the contrary, the region of strongest fluctuation at station 3 moved outboard and/or upward, which may be related to the weaker vortex sheet rolled up from the leading edge and the secondary vortex formed close to the wing surface at the tip.

Histograms of velocity fluctuation

Since the strong strake-wing vortex burst upstream of the wing trailing edge, it is interesting to see whether there was intermittent motion of the burst location. Histograms of velocity components are, therefore, examined at three chosen positions at station 3, which are underneath, at, and above the burst core region. Results are shown in Fig.4.21., 4.22, and 4.23. Above the burst core, velocity fluctuations were very small, as implied by the sharp, narrow peak in the histograms, except for that of the V component. Referring to Fig.4.17c, this indicates possible moderate up/down motion of the rolled-up vortex sheet surrounding the burst region, following the pulsating or intermittent motion of the burst region. Inside the burst core region, velocity fluctuation was so high for all the components, that the probability distribution is much broader and includes both positive and negative velocity regions. For the axial component (U), there is even a 50-50 chance for positive and negative velocity occurring. No distinct bimodality is observed. However, vigorous motion of the burst core region surely existed in order to give such velocity histograms. Below the burst region, a broader distribution is still seen for all velocity components, but the flow direction is pretty consistent this time. Noticeable bimodality can be observed in the histogram of the V component, indicating intermittent flow separation above the wing surface.

4.3 Static Pressure Distribution

The chordwise static pressure distribution at six spanwise stations, as shown in Fig.4.24, was measured. The purpose of these measurements is to correlate surface pressure with other flow field data above the wing, and provide information for code validation. A few gaps at the first three spanwise stations can be seen in the figure, simply due to the reinforced supporting plates underneath the wing, which left no space for pressure taps. Tests were repeated for three freestream speeds and four angles of attack.

Fig.4.25 shows the results at different angles of attack at 50 ft/sec. At the most inboard station, the pressure distribution was very smooth for low to moderate angles of attack. The suction peak due to the strake vortex became distinct at high angle of attack, and the Cp level experienced a sudden jump, even at positions toward the trailing edge. This increase in Cp level toward the trailing edge at high angle of attack might not be caused by the suction induced from the wing-strake vortex, since the vortex bursting location will move upstream with increase of angle of attack. The true reason is not clear at this time. The vortices formed beneath the primary vortex structure, e.g. those seen in the vorticity contour plots, might play a role in this case. As we move to station 2 and 3, the suction peak close to the leading edge, corresponding to the strake-wing vortex, increases drastically for all angles of attack, and reaches a high value of 2.5 at 25 degrees. Nevertheless, the increase in peak value for 35 degrees was smaller than other angles, and it even became lower than at 15 degrees at station 3. This phenomenon proves that the transition of vortex bursting happens earlier for 35 degrees. As the vortex burst,s the pressure distribution experiences an abrupt change in slope, and dropped to a lower Cp level. At stations 4 and 5, the suction peak is highest for 15 degrees. This says that the 25 degree case has now also entered the transition, but still shows a higher suction than the 35 degrees case. Overall, the suction lift produced by the vortex system over the wing surface is highest at moderately high angles of attack (25 degrees in this case). Compared to the case at low angle of attack (10 degrees), the lift generated at high angles is always higher throughout the spanwise stations, even after experiencing vortex bursting.

Fig.4.26 shows the same results as in Fig.4.25 from a three-dimensional, global point of view. For angles of attack of 10, 15, and 25 degrees, the pressure distribution over the whole left wing surface experienced a sharp negative pressure valley induced by the vortex system along the wing leading edge, which correlated well with the results from flow visualization and velocity measurements. However, in the 35 degree case, the distribution was smoother, but at a higher Cp level. This observation implies that at 35 degrees, vortex bursting probably occurred right after the strake-wing junction, and the whole wing was covered under a big vortical flow structure.

The comparison between results under different freestream speeds at 25 degrees angle of attack is presented in Fig.4.27. Except for a small difference noticed at the leading edge locations of the most inboard spanwise station, the pressure distribution shows the same trend for all the spanwise stations with a slight increase in Cp as speed goes up.

13

This ensures that the speed effects on the flow field of the model were minimal for the range we were interested in.

4.4 Hot-film Anemometry

A hot-film anemometer was used to obtain spectral information on the model flowfield at the stations shown in Fig.4.28. Measurements under different flow speeds and angles of attack were performed for comparison purposes.

Velocity spectra

Fig.4.29 shows velocity spectra obtained at different heights above station 1 at a freestream speed of 50 ft/sec. Starting from 0.25" off the wing surface, a sharp peak at about 48 Hz can be easily identified with a spectral density level at around 1.5. As the sensor was moved up with one inch increments, several peaks in the neighborhood of 50 Hz began to show up. The highest peak shifted between 40-60 Hz with similar spectral level, despite the presence of a spike at an extremely low frequency. Once it reached and went above the height of 5.25", the peak centered around 50 Hz reappeared, and the spectral level dropped quickly from 1.5 to 0.011. After referring to the velocity data, it is not surprising to notice that the region with multiple peaks is coincident with the region where the burst vortex was located, and higher velocity fluctuation on all three components was present.

As we move upstream to station 6, at the fore portion of the wing, a broadband spectrum is seen in Fig4.30, with a peak centered roughly around 150 Hz. The height of this measuring point was 3.25" above the surface, which is right over the concentrated vortex at this station. Moving further upstream to station 4, which was right after the strake-wing junction, once again we have a broadband spectrum as shown in Fig.4.31. However, the peak frequency can no longer be distinguished. Based on the observations mentioned above, *it appears that a clear, dominant peak frequency can only be easily identified at locations after the vortex bursting, where no concentrated vortex exists in the flow field.* Otherwise, the vigorous interaction and merging between vortices causes the flow field to become so turbulent that no particular peak frequency can be seen.

Variation of the dominant frequency with freestream speed

Because of the existence of a well defined dominant frequency at station 1 above the burst vortex, it is interesting to see how this frequency will vary with changes in freestream speed. Fig.4.32 shows the velocity spectrum at the same measuring point with

freestream speeds varying from 20 ft/sec to 100 ft/sec. At low speeds, a very sharp peak at the dominant frequency can be picked up. As speed increases, the peak broadens somewhat, but it is still possible to choose the centered frequency. All the peaks chosen are plotted against the freestream speed, and are shown in Fig.4.33. The result indicates that a fairly linear relationship exists between the dominant frequency and freestream speed, as seen in previous work[1,2].

Variation of dominant frequency with angle of attack

Fig.4.34 shows the velocity spectrum measured at a fixed height above the wing surface at station 1 at different angles of attack. Except for the case of 25 degrees, at which the dominant frequency can be easily identified, multiple peaks are found in all the other cases. The highest peak frequency can still be roughly chosen, and falls in the range of 30-50 Hz. The spectral density level increases rapidly as the angle of attack increases. Following the interpretation mentioned in the section on "velocity spectra", it can be said that the dominant frequency stays roughly the same with change in angle of attack, since the measuring point actually moved from 2-3" above the burst vortex region to probably the center of the region as the angle of attack went up. This does not agree with previous data, where the dominant frequency was seen to drop as angle of attack increased[1,2].

Spectral analysis with LDV signal

Since the hot-film sensor cannot differentiate the flow direction, the spectral information thus obtained will include the contribution from all the velocity components. Therefore, spectral analysis with the analog voltage output in time domain from the LDV counter processor was tried. The digital data coming from the LDV was sent into a 12-bit D/A converter. The result is a voltage value which stayed constant until changed by the next data value, and thus the signal takes on the appearance of a series of "steps". If the data rate is high enough, this signal can be passed through a low-pass filter, yielding a reliable turbulence signal. This technique requires data rate that is high enough for the sampling rate chosen, which did not pose any problem, since we had data rates on the order of a few thousand per second, while the frequency range of interest was below 100 Hz. Hence, success was achieved. Fig.4.35 shows the results measured above the burst vortex at station 1. The dominant frequency is found to be around 45-50 Hz, with a secondary peak located at about 15-20 Hz. The W velocity component has the highest spectral density level, which is 40 times over the U component, and 12 times over the V component, and the level of the secondary peak is about two third of the primary peak. Fig.4.36 shows the results measured at the same station but inside the burst region. The same dominant

frequency is identified from all three components. However, the spectral density level is now more comparable between components, but is still lower than at the previous location. From the last two figures, it is shown that the LDV signal can be used for spectral analysis and gives the correct dominant frequency, component by component without ambiguity. However, it is less sensitive than the hot-film anemometer to the smaller turbulent structure in the flow field, which in some cases may be desirable.

5. CONCLUSIONS

1. The flow field above a generic wing/body model at high angle of attack has been extensively documented using laser sheet flow visualization, laser velocimetry, hot-film anemometry and static pressure measurements. As a result, a multi-faceted data set is now available for the development of computational methods on a configuration of simple geometry.

2. The vortices from the forebody are seen to merge into the concentrated strake vortices, which in turn merge with the wing leading edge vortices. This process is visible on the videotape at low angle of attack. Mutual induction of the vortex systems is also visible, so that the vortex system above the wing actually consists of three difference vortices revolving around each other.

3. The symmetry of the vortex system is very sensitive to the shape at the nosetip. Any small asymmetry at the nose is amplified dramatically due to the induction effect between the vortices on the two sides. The asymmetric systems remain steady under steady model attitude. After the nose was faired by trial and error using modeling wax, symmetry was improved drastically.

4. At moderate to high angles of attack, the vortex system over the wing was found to burst at location roughly 56% of the model length.

5. Three components of velocity were measured at 3 stations, which were ahead of the strake-wing junction, fore part of the wing and close to the wing trailing edge. The vortical structure is the dominant feature at all stations. However, at station 1, a strong concentrated strake vortex formed, with axial velocity inside the core going up to 3 times the freestream speed. At station 2, the vortical structure appeared flattened and enlarged with slightly decrease in axial velocity, indicating the onset of transition to vortex bursting. At station 3, well past the vortex burst location, only a large vortical structure existed with flow reversal noted in the center region.

6. The velocity fluctuation was examined using the contour plots of root-mean-square (rms) velocity for all 3 components. High fluctuation levels were found at the first two

stations, where vortex strength was much higher and interactions between vortices were so vigorous.

7. No clear bimodality can be seen in the velocity histograms. However, the results do suggest strong unsteady motion of the burst core region at the station close to the trailing of the wing.

8. A sharp negative pressure valley induced by the vortex system over the wing can be seen along the leading edge of the wing in the surface pressure distribution, which correlated well with other data obtained from flow visualization and LDV measurements. At much higher angles of attack, the pressure distribution became more smooth, but still with higher Cp level.

9. Upon vortex bursting, a sharp change of slope in chordwise pressure distribution occurred with reduced Cp level. However, at high angle of attack, even after the vortex burst happened, the suction experienced was still higher than that produced under unburst condition at low angle of attack.

10. Velocity spectra measured at the station close to wing trailing edge show that a dominant frequency existed in the flow field. The value of this frequency changes slightly in a narrow range as the measuring point moved up and went through the burst core region.

11. As the measuring point moved upstream, the dominant frequency increased. However, the spectrum shows more broadband turbulence, with the peak frequency getting harder and harder to identify.

12. The dominant frequency found at the trailing edge station scales linearly with freestream speed at fixed angle of attack.

13. No clear change in peak frequency was found with change in model angle of attack, besides the change in shape of the spectrum.

14. The analog signal from LDV counter processor was used successfully in spectral analysis, and compared well with the spectrum obtained from hot-film anemometer. This provides the ability to do the spectral analysis component by component without directional ambiguity.

ACKNOWLEDGEMENTS

6. REFERENCES

1. Komerath, N.M., McMahon, H.M., Schwartz, R.A., Liou, S.G., Kim, J.M., *"Flowfield Measurements Over a Fighter at High Angles of Attack"*. AIAA Paper 90-1431, 16th Ground Testing Conference, Seattle, WA, June '90.

2. Komerath, N.M., Schwartz, R.A., Percival, S., Kim, J.M., *"Unsteady Vortex Flow Measurements Over Twin-Tailed Aircraft at High Angles of Attack"*. AIAA91-0279, Jan.'91.

3.Edwards, J.W., *"Assessment of Computational Prediction of Tail Buffeting"*. NASA TM 101613, Jan.'90.

4. Schiff, L.B., Cummings, R.M., Sorenson, R.L., Rizk, Y.M., *"Numerical Simulation of High-Incidence Flow Over the F-18 Fuselage Forebody"*. AIAA 89-0339, Jan. 89.

5. Hellsten, C.P., "Supersonic Bizjet Wind Tunnel Model". Drawings and Model constructed for the Senior AE Design Course, May 1986.

6. Sellers, W.L., Meyers, J.F., Hepner, T.E., *"LDV Surveys Over a Fighter Model at Moderate to High Angles of Attack"*. SAE TP Series 88-1448, Oct. 88.

FINAL   TECHNICAL   REPORT

JOHN J. HARPER 7' X 9' WIND TUNNEL
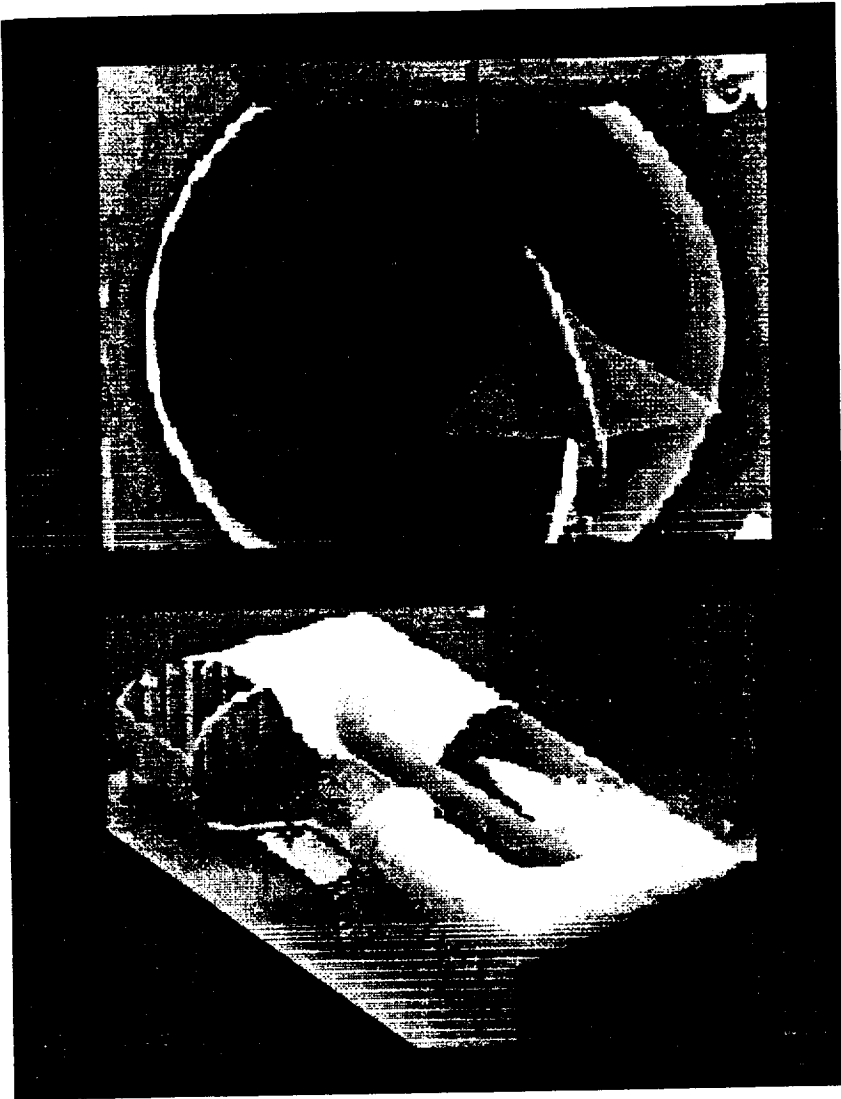
0-220 ft/sec

0.2 % turbulence

Closed return

6 - d.o.f. balance

h.p. air supply

Laser velocimeter

Laser sheet

Pressure sensing

Hot-wire / hot-film

Spectral analysis

Digital Imaging

Fig.2.1 Picture of John J. Harper 7'X9' wind tunnel

Side View

Top View

Fuselage diameter is 3 inches.

Wing leading and trailing edges have 18 degree bevel on lower surface.

10.50

45.00

13.00

9.00

12.34

1.50

74.7°

59.4°

14.0°

22.65
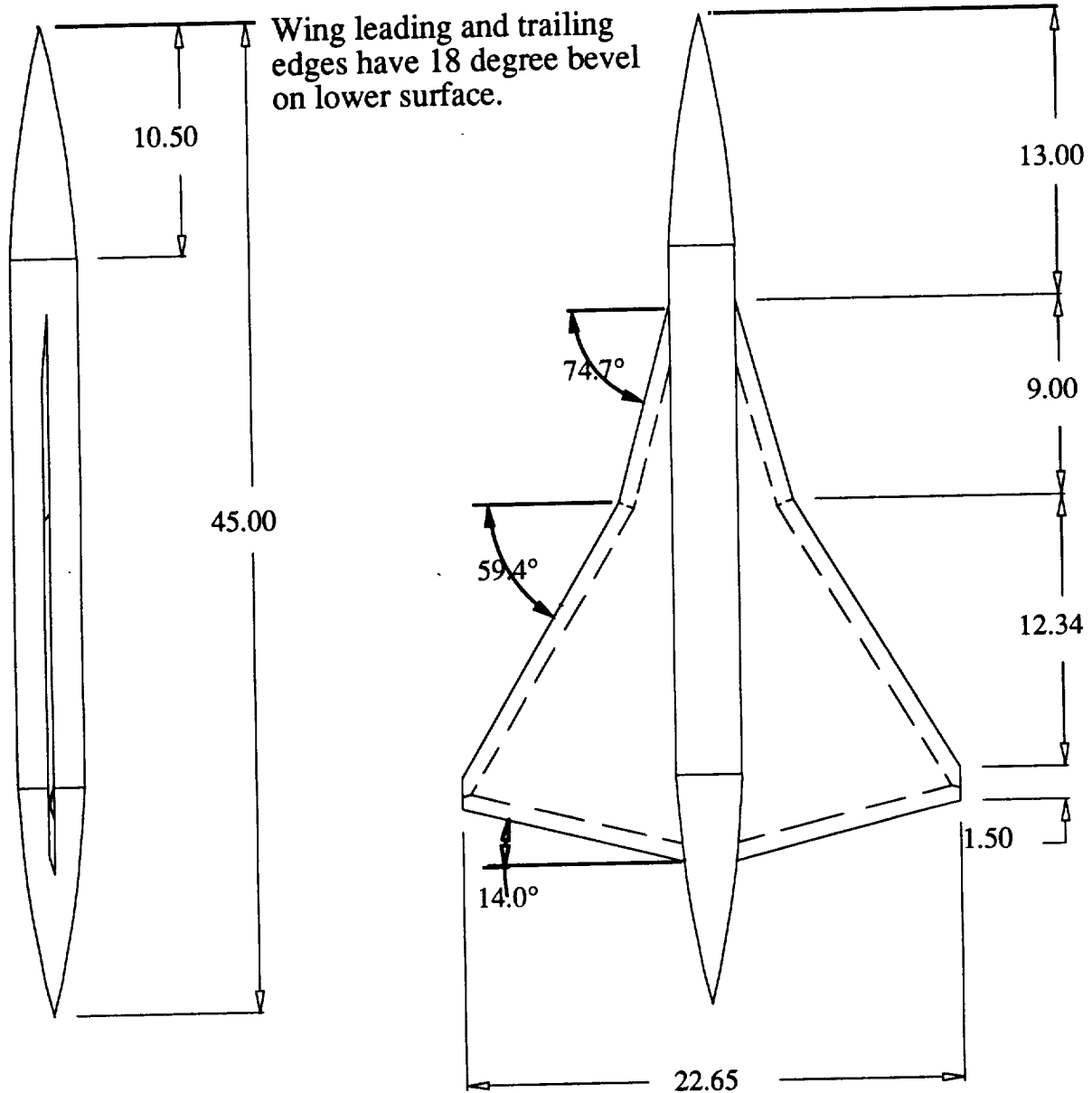
Fig.3.1 Geometry and dimensions of the generic wing/body model
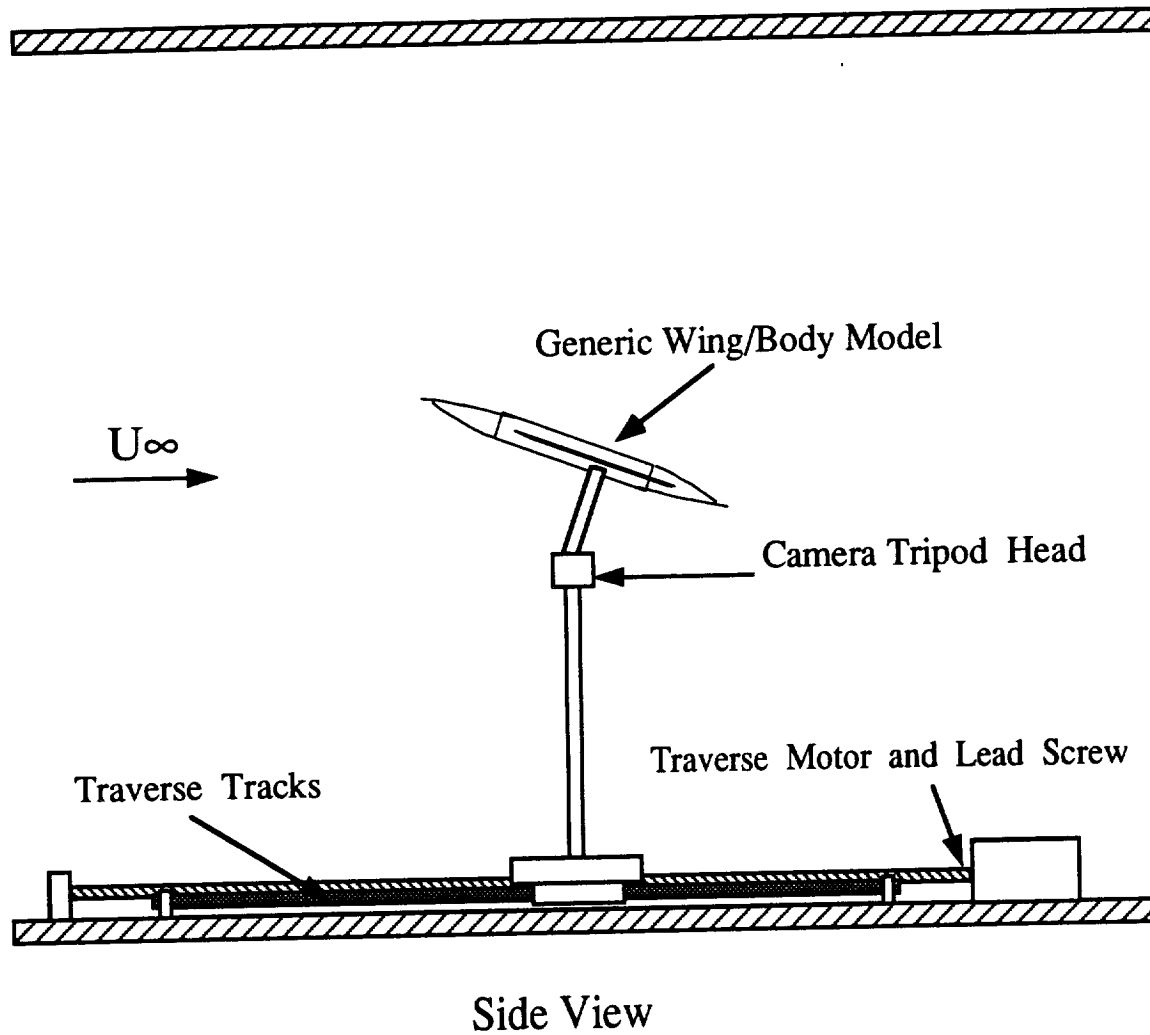
Fig.3.2 Model set-up inside the test section

Optics Box   Fiber Optic Cable from Laser

Smoke
Wires

Laser Sheet

U_∞

Video Camera

Camera
Tripod Head

Traverse Motor and Lead Screw

Traverse Tracks

Side View

Fiber Optic Cable from Laser

Optics Box

Smoke Wires

Laser Sheet

Traverse System
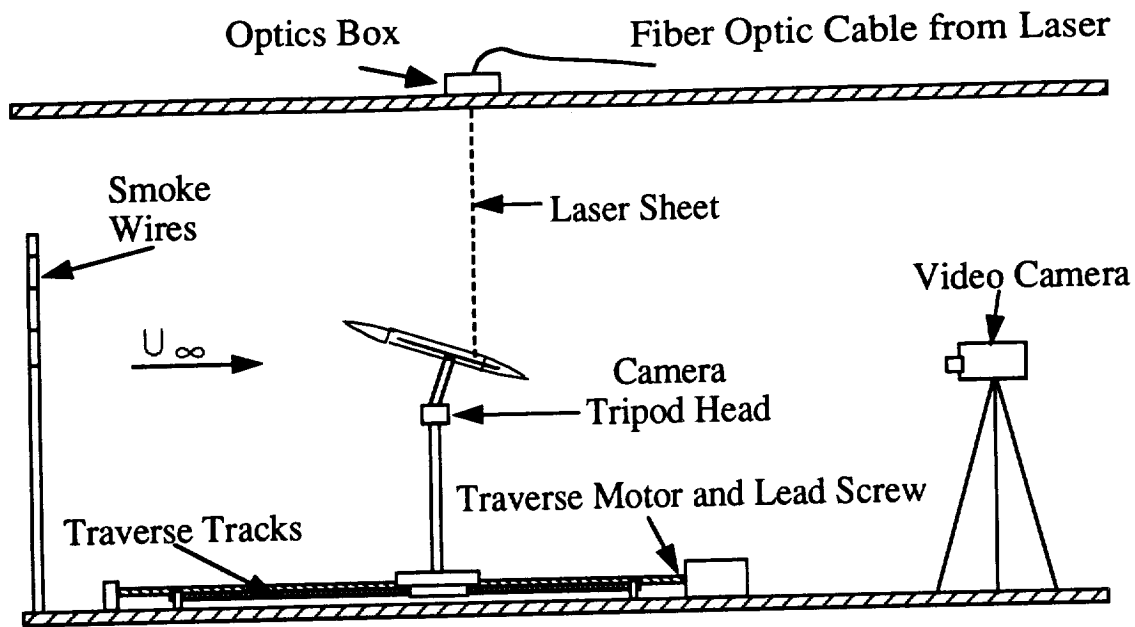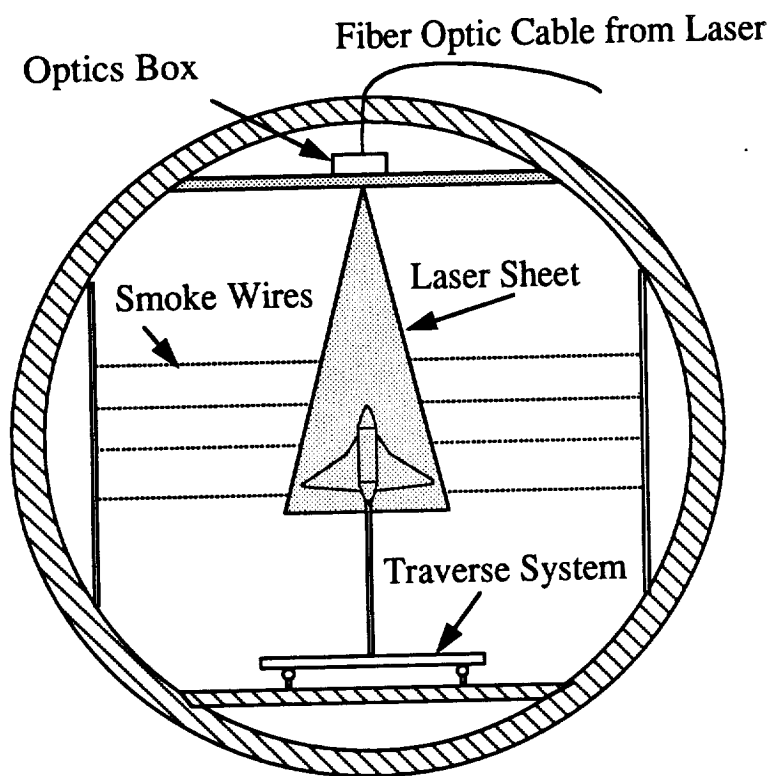
Rear View

Fig.3.3   Flow visualization set-up
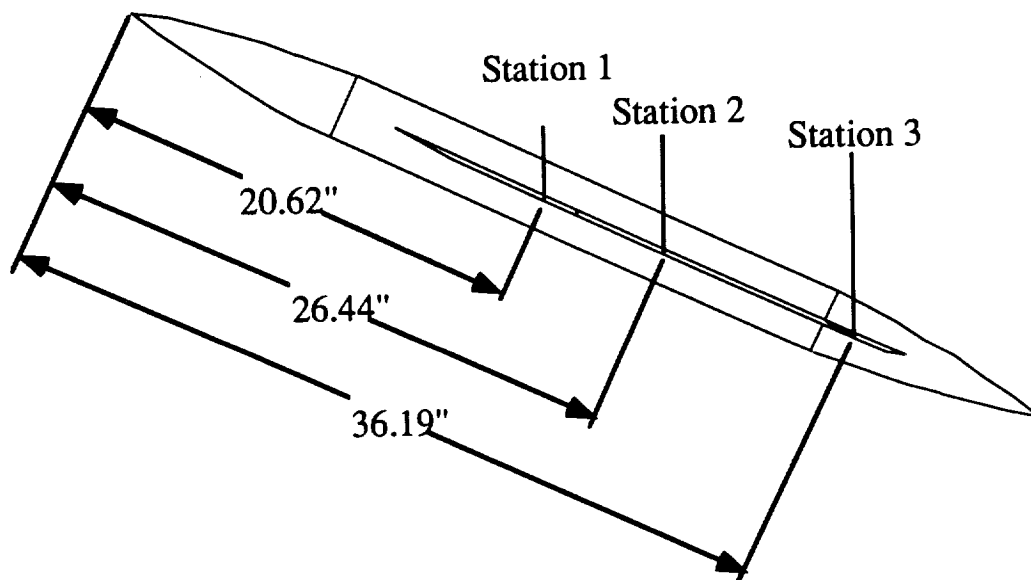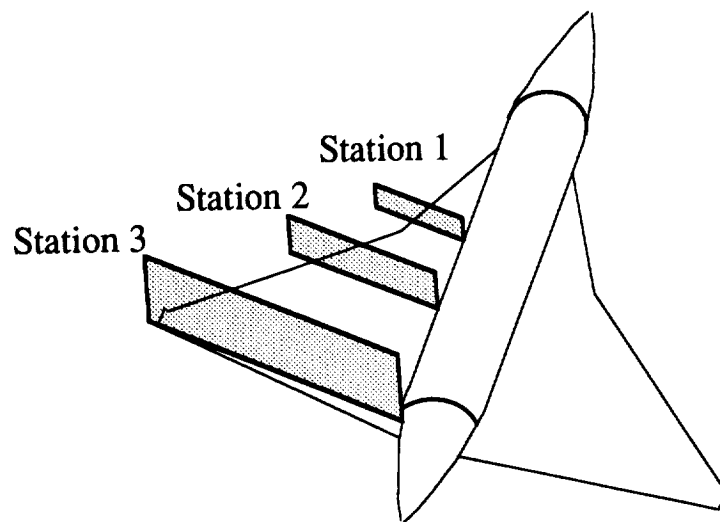
Fig.3.4 Location of measuring planes for velocity field survey
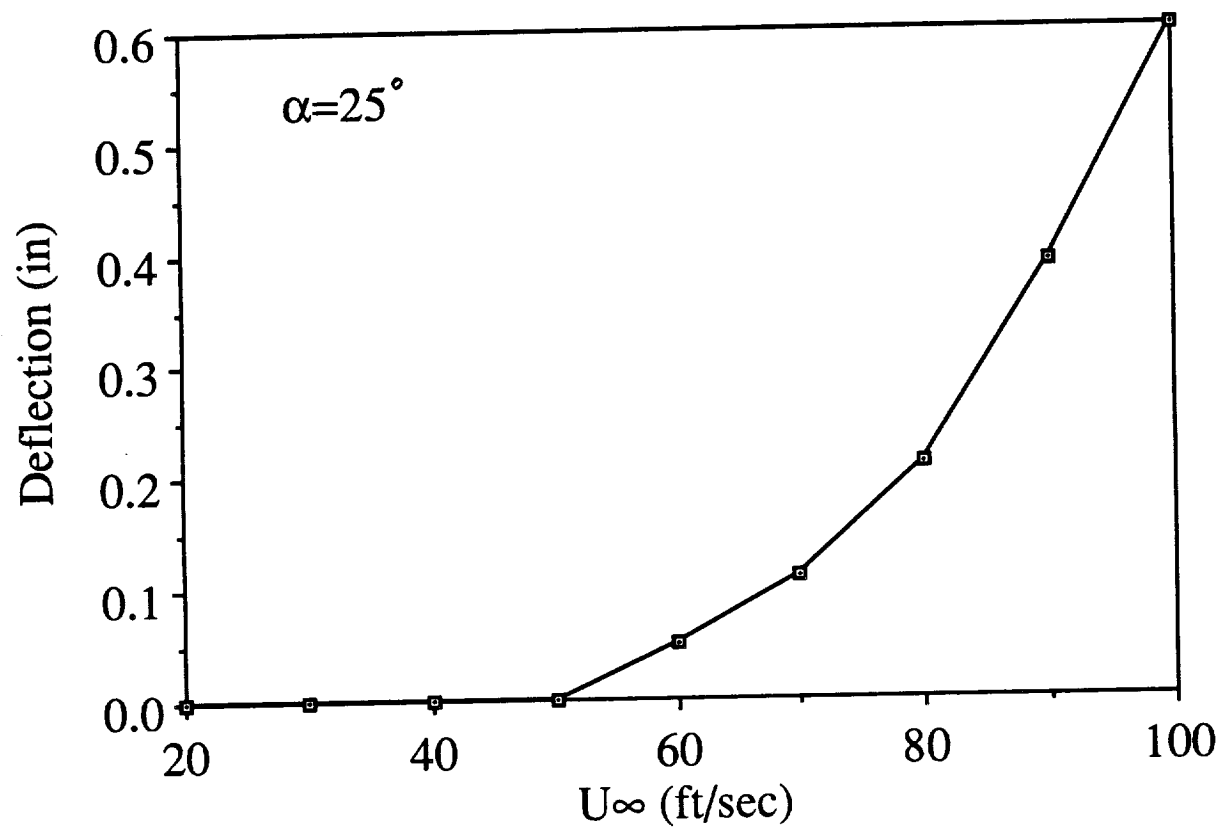
Fig.4.1   Deflection of model nose-tip under different freestream speeds
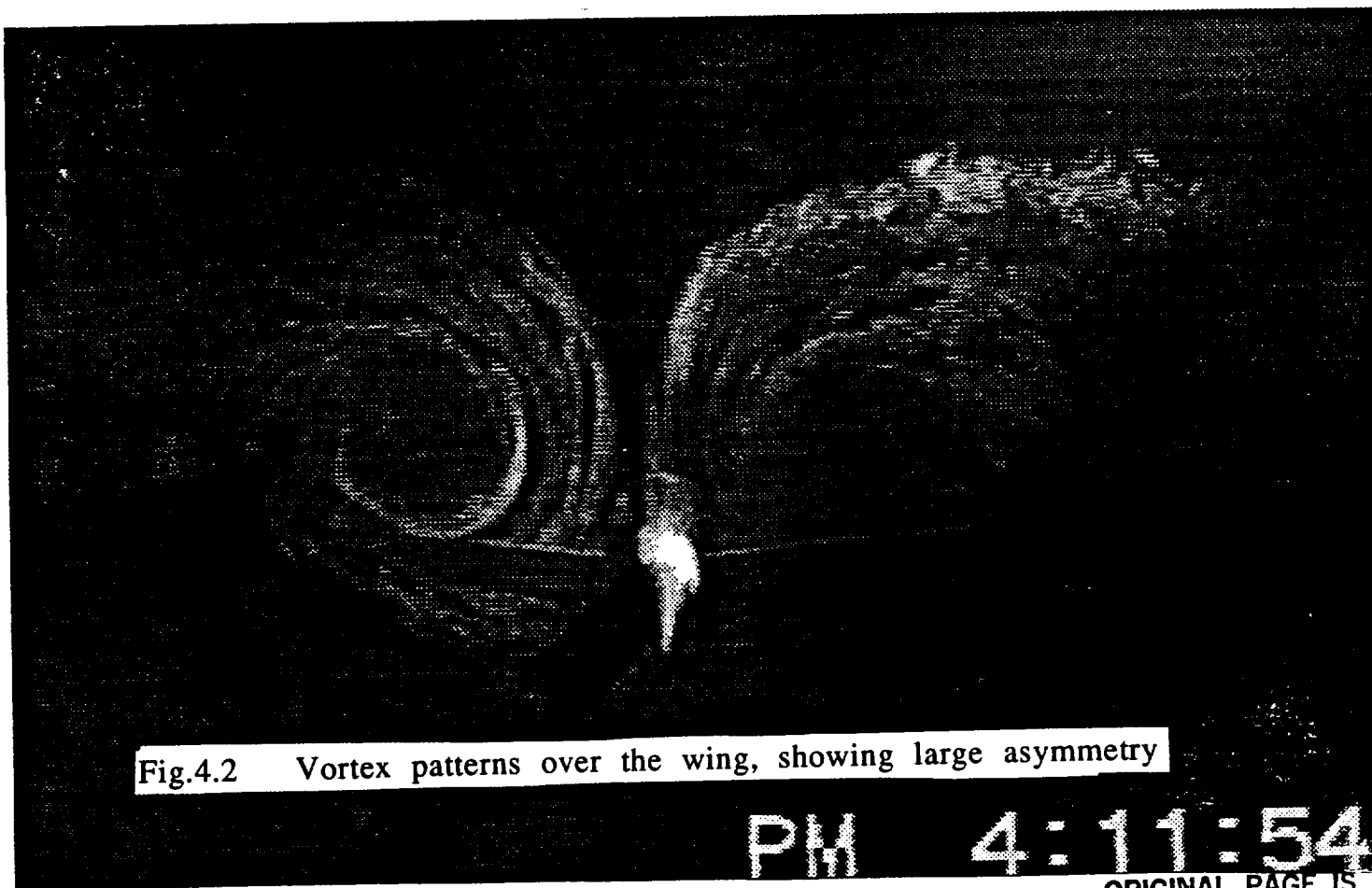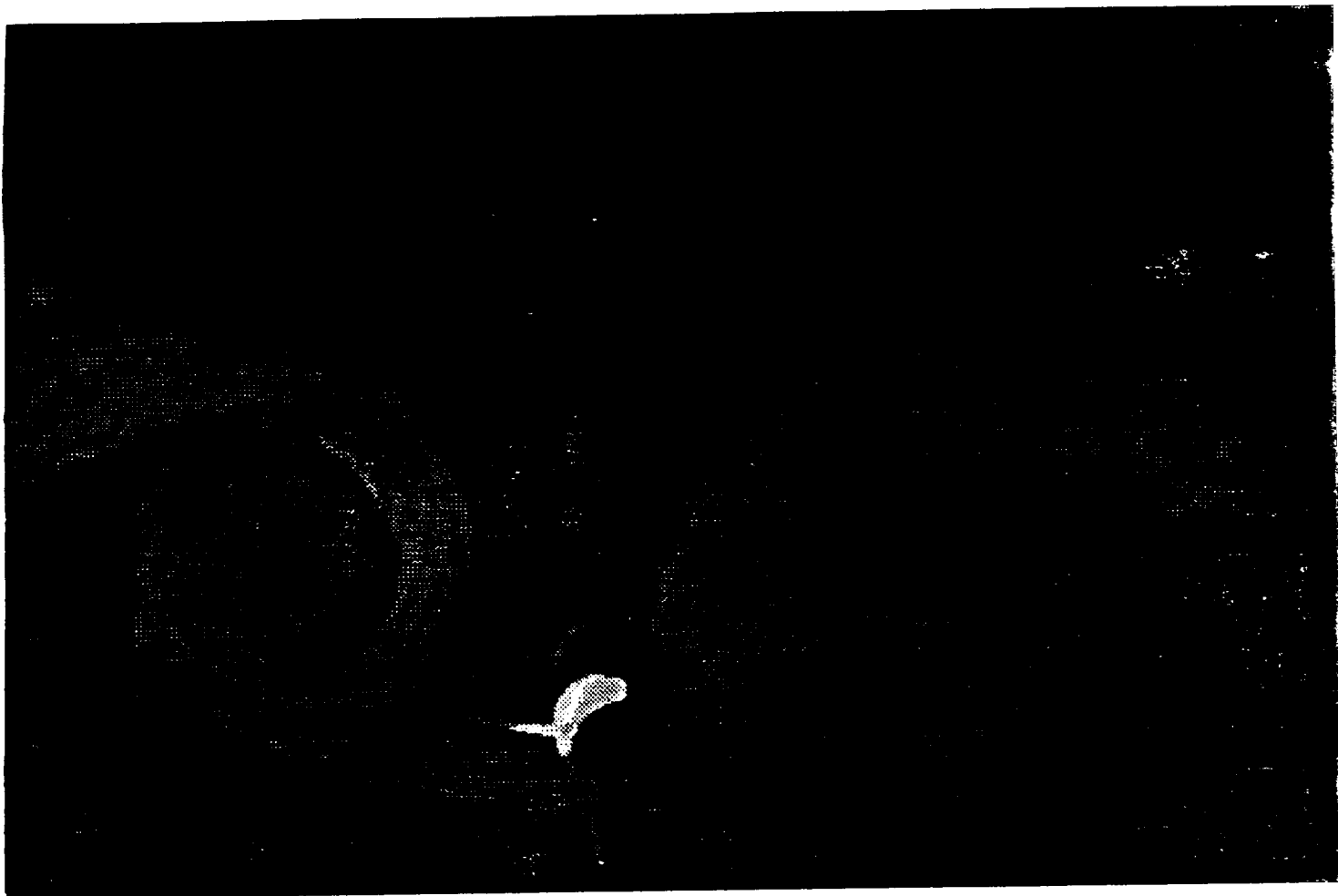
Fig.4.2   Vortex patterns over the wing, showing large asymmetry

PM   4:11:54

PM 2:12:23
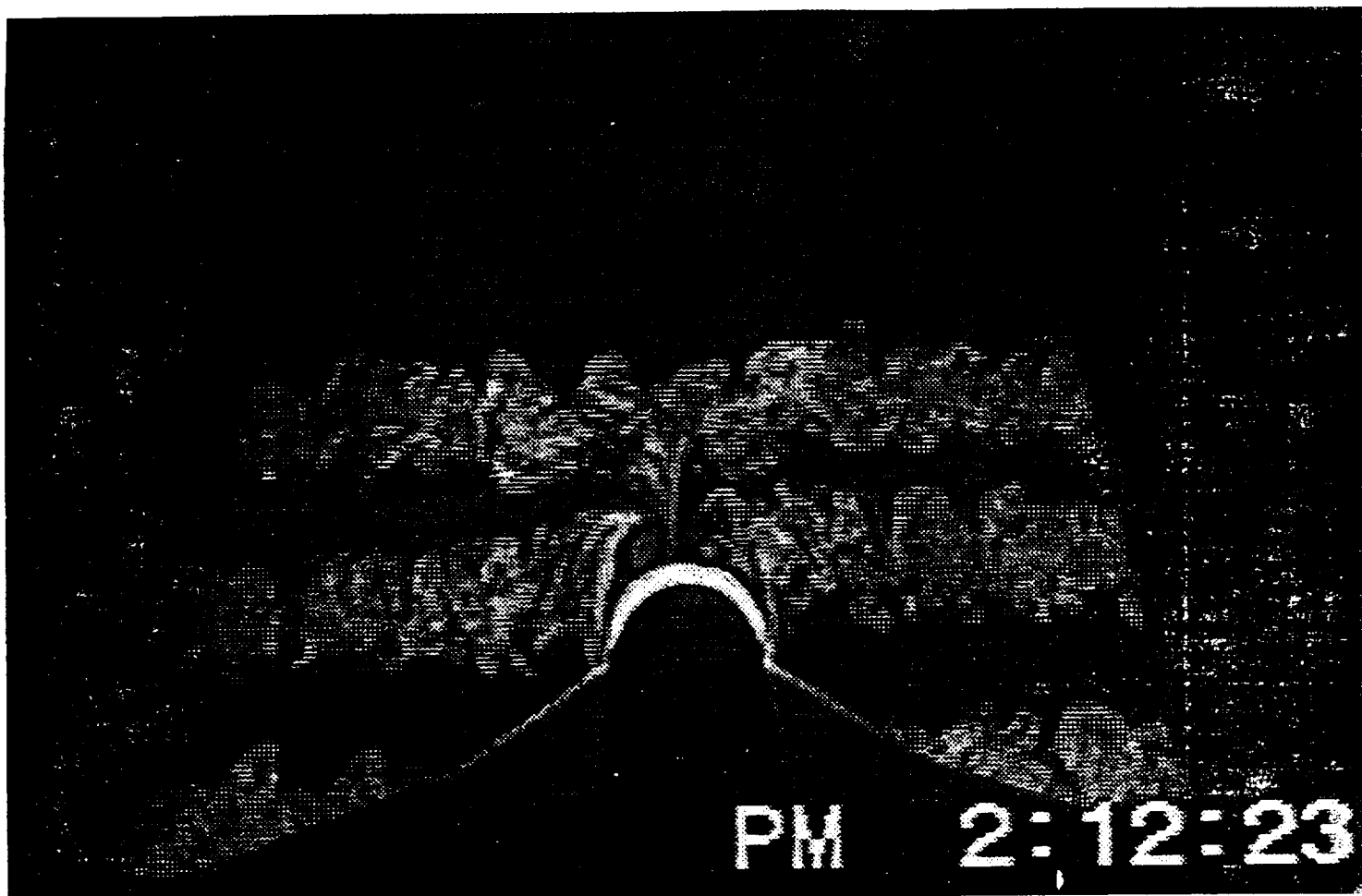
Fig.4.3   Origin of asymmetry: the forebody vortices

PM 1:43:13
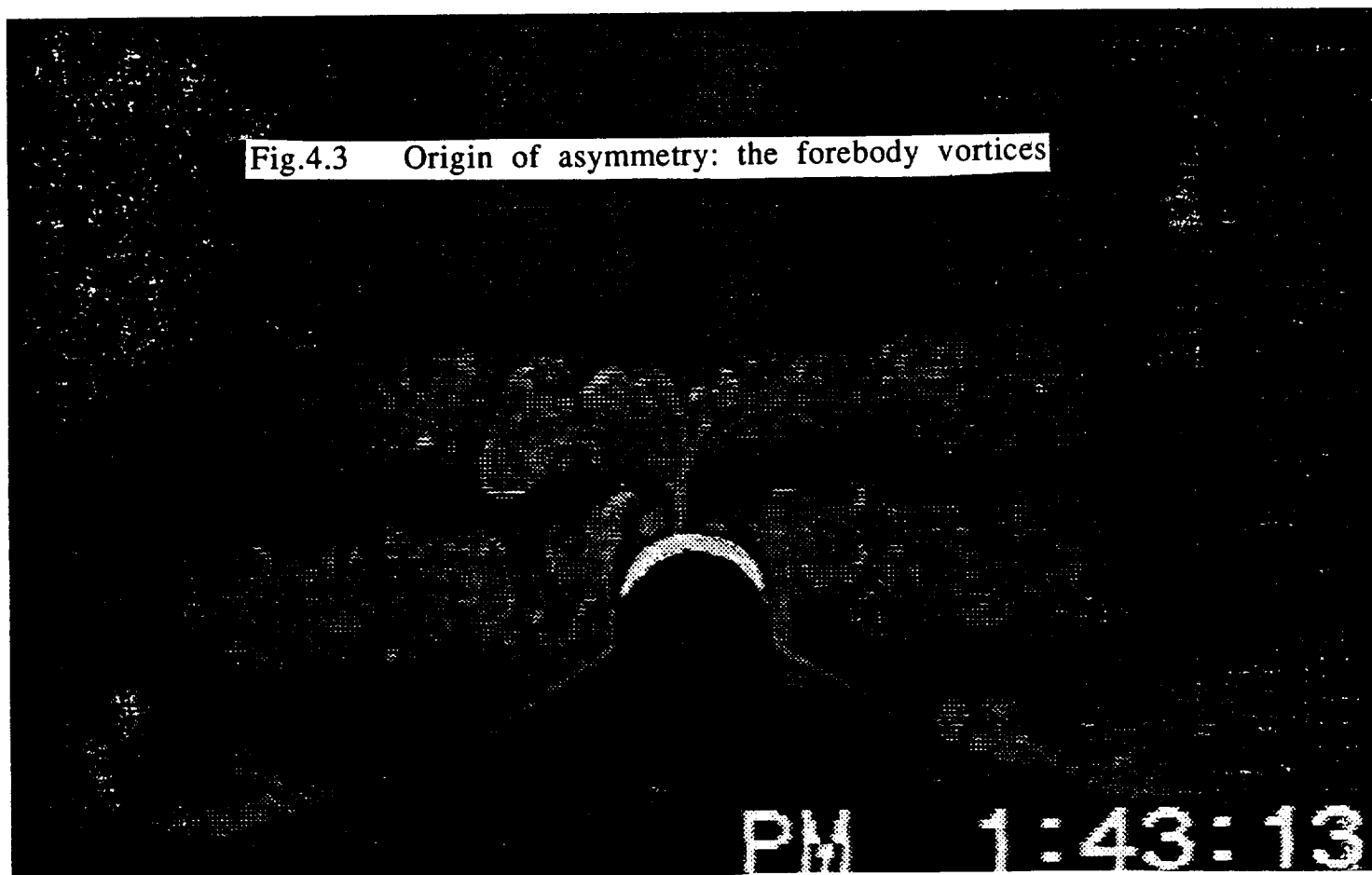
Fig.4.4 Forebody vortex systems after modification to nose
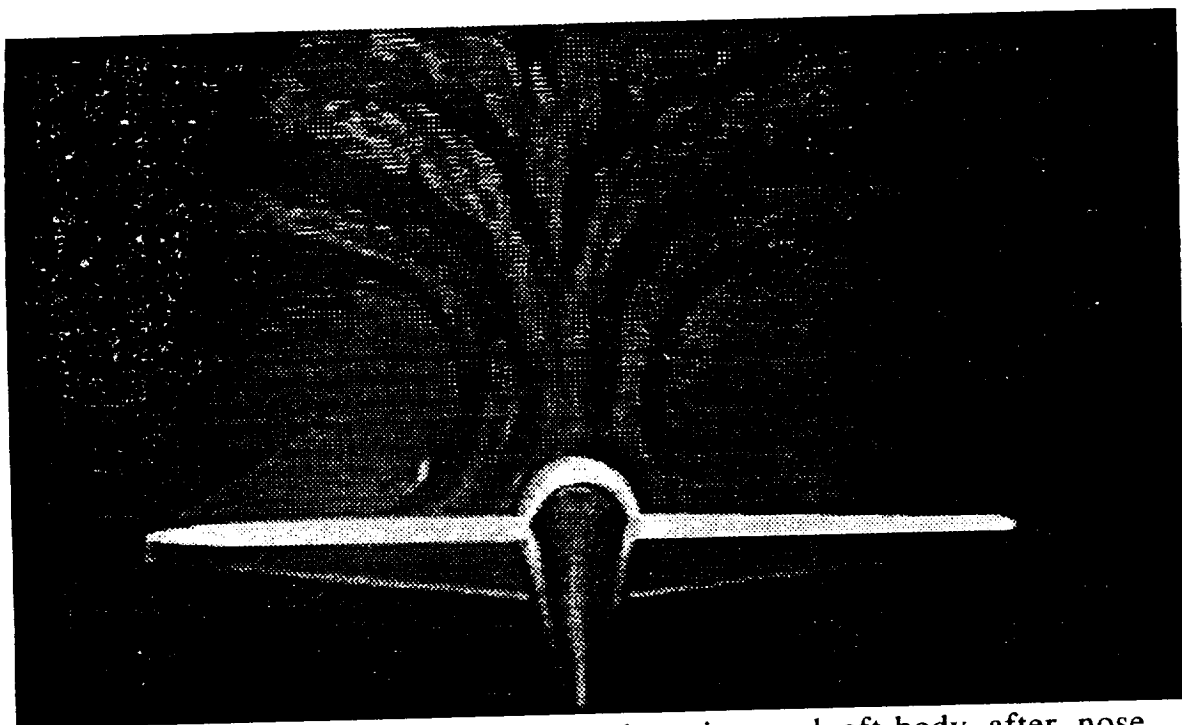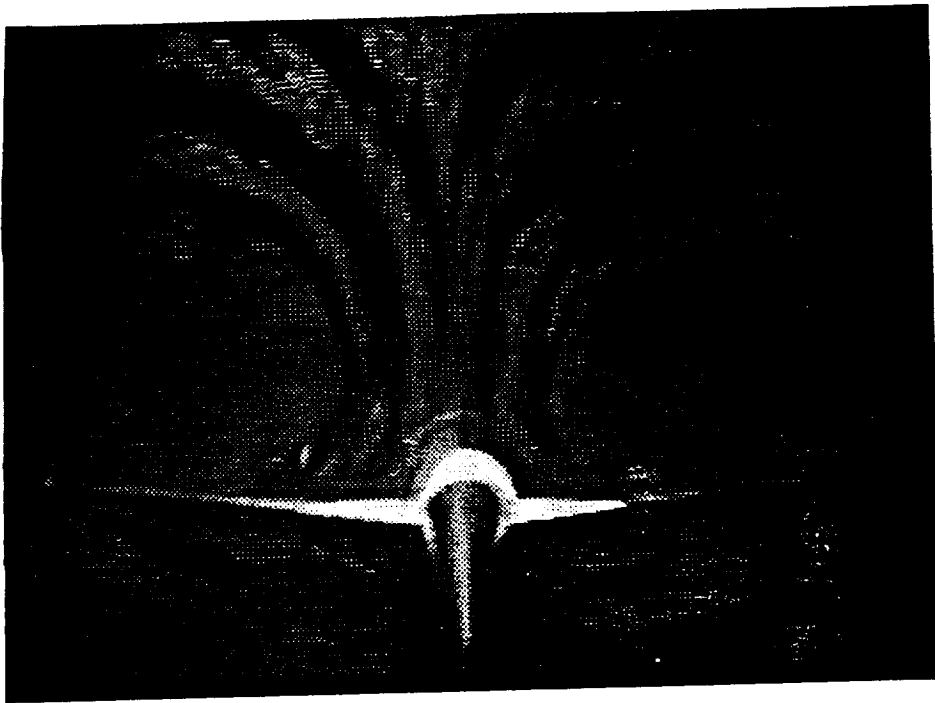
Fig.4.5   Vortex patterns over the wing and aft-body after nose modification

Forebody - Strake - Body Vortices Superposition

Front View

(a)   (b)   (c)
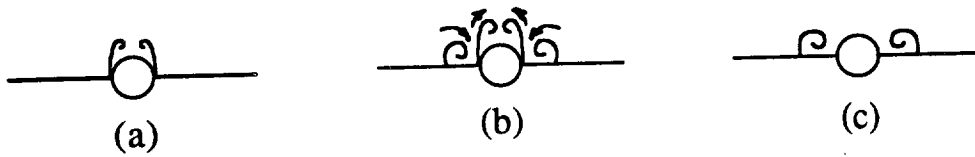
a) Formation of body vortices

b) Formation of forebody - strake vortices with body vortices

Arrows represent circulation strength

c) Superposed strake-body vortices

Wing -Strake Vortices Superposition

Front View

(a)   (b)   (c)

(d)
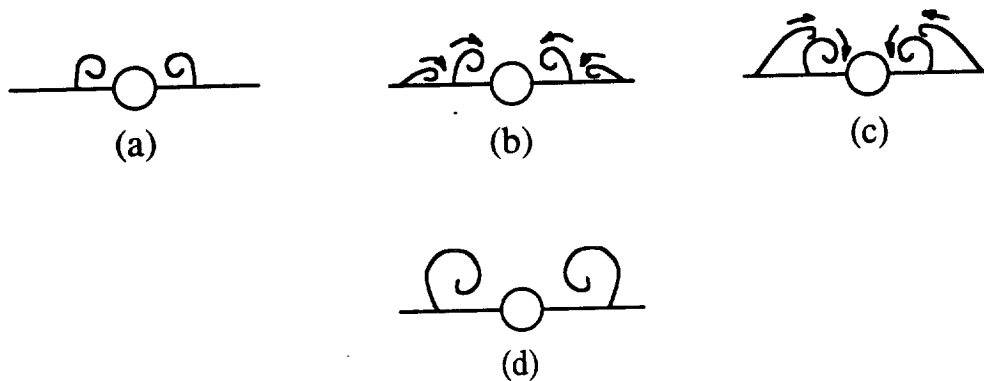
a) Superposed strake - body vortices

b) Strake - body vortices with the formation of wing vortices

c) Instant before superposition

d) Superposed wing - strake vortices

Fig.4.6   Sketch of vortex systems and their superposition
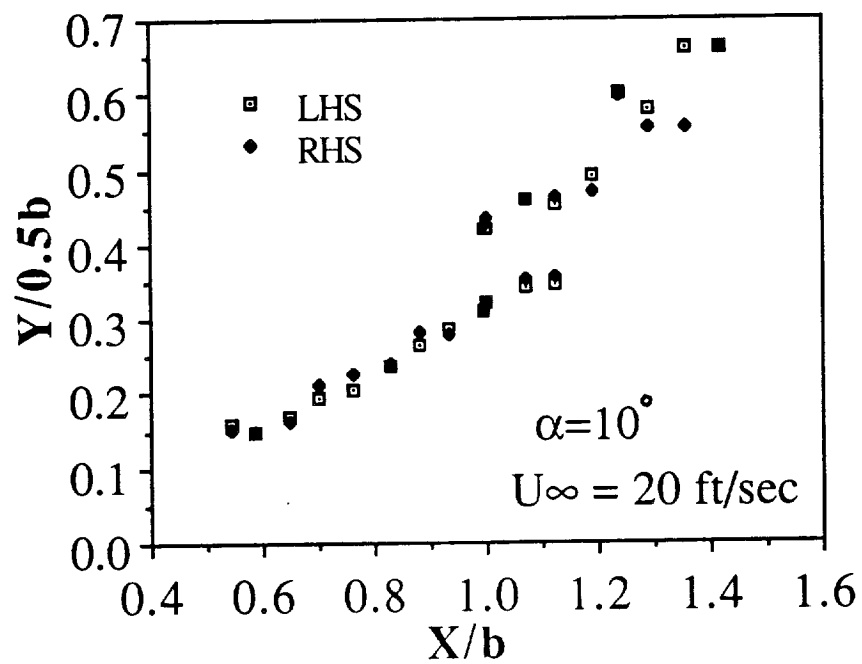
Fig.4.7a   Vortex positions located along one-half span of the model,
U∞=20 ft/sec, α=10°
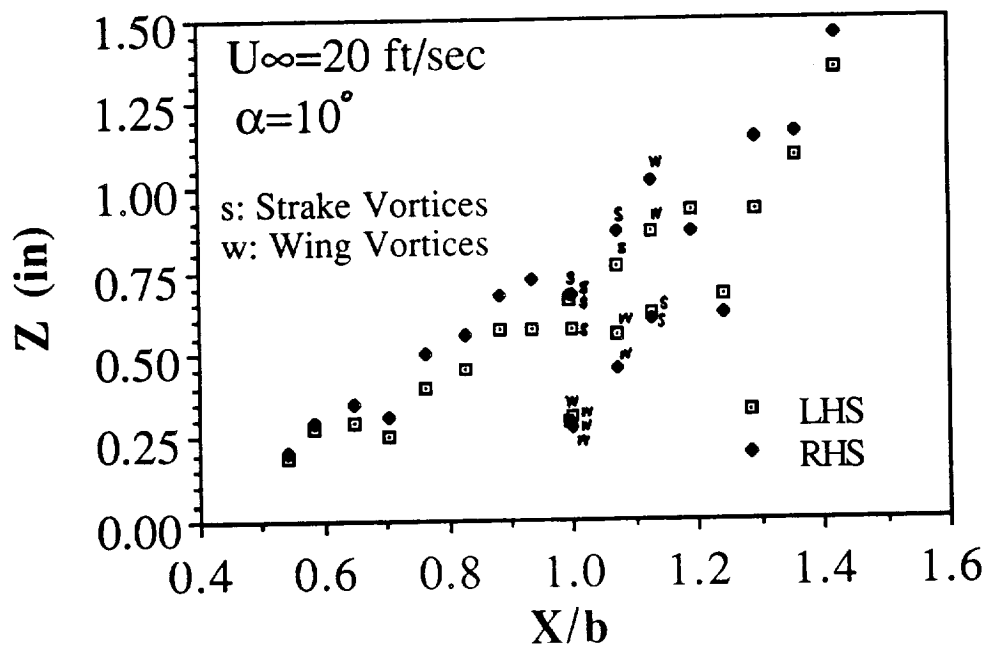
Fig.4.7b Height of vortex cores along the model, U_∞=20 ft/sec, α=10°
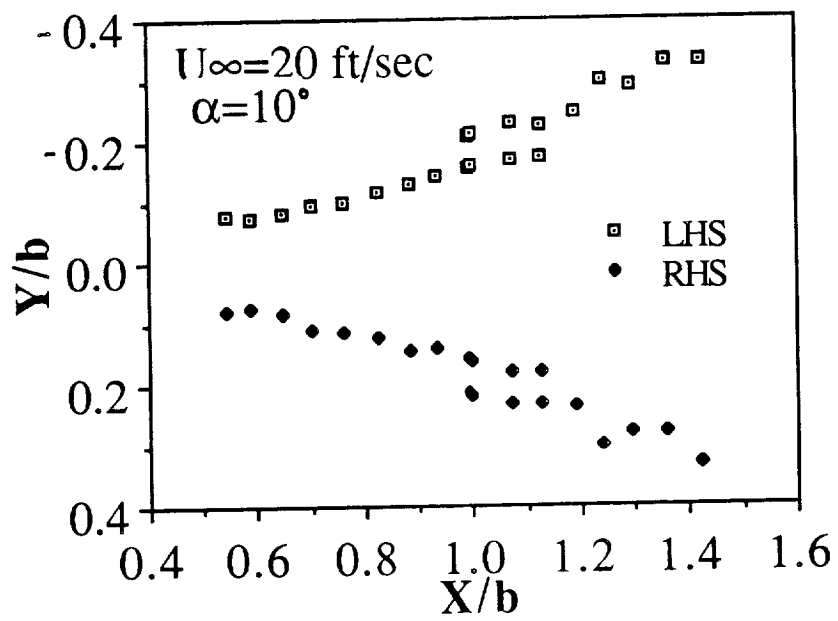
Fig.4.7c   Vortex core trajectory along the model, U_∞=20 ft/sec, α=10°
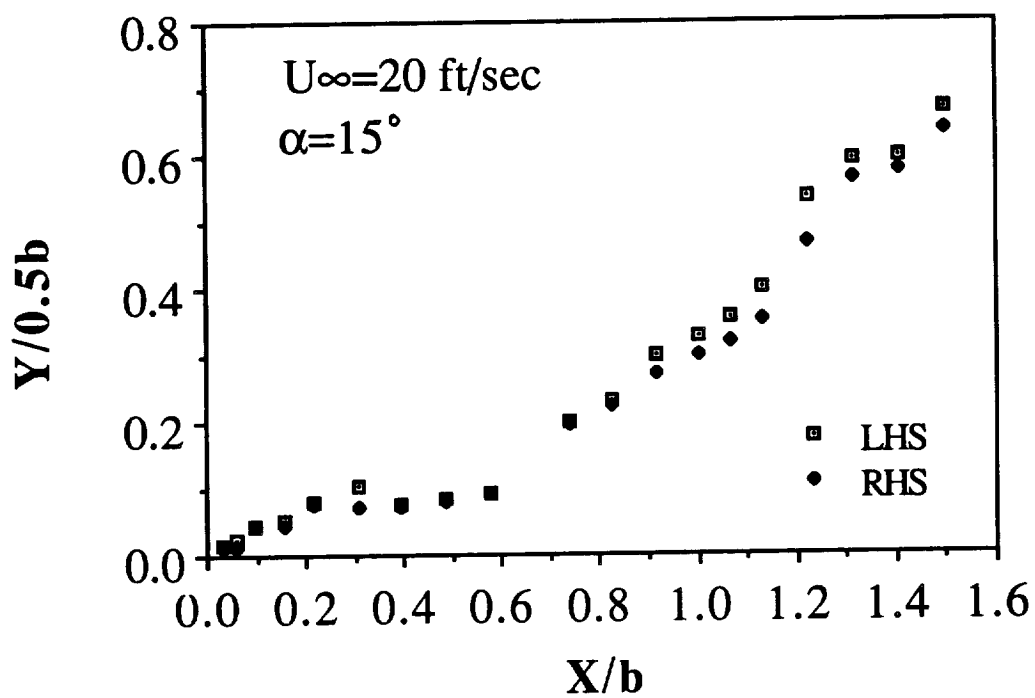
Fig.4.8a   Vortex positions located along one-half span of the model,
U∞=20 ft/sec, α=15°
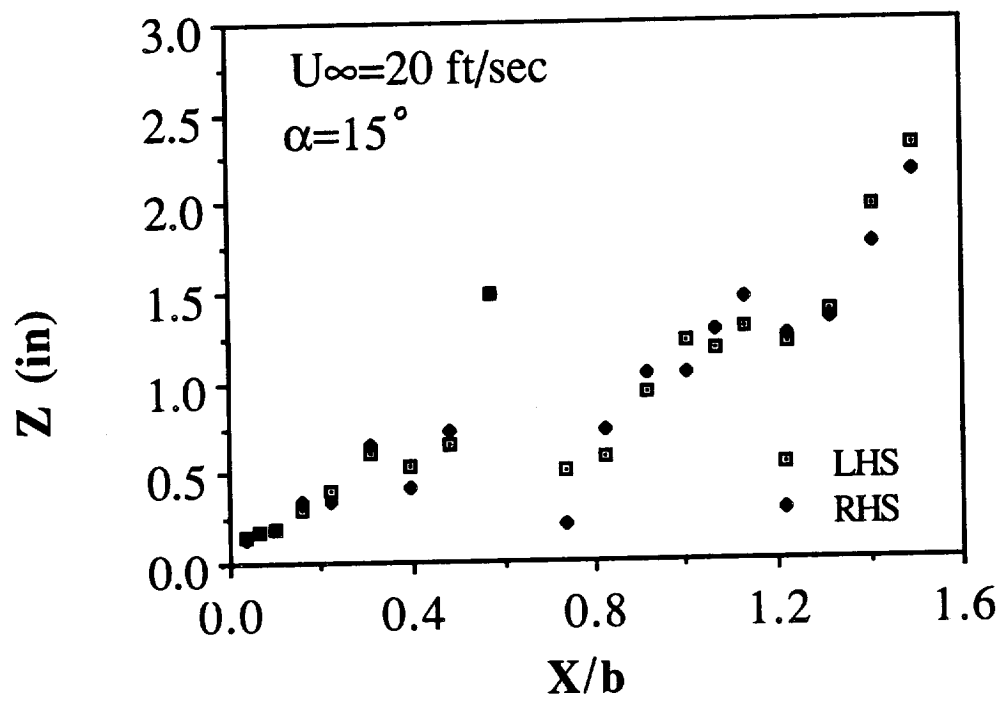
Fig.4.8b   Height of vortex cores along the model, U_∞=20 ft/sec, α=15°
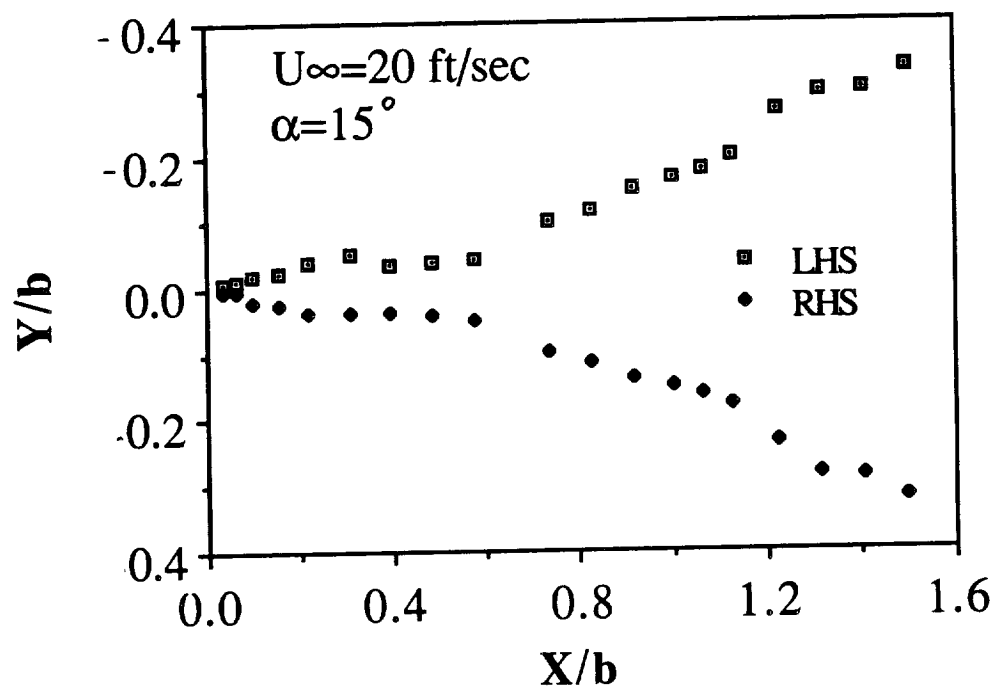
Fig.4.8c Vortex core trajectory along the model, $U_\infty=20$ ft/sec, $\alpha=15^o$
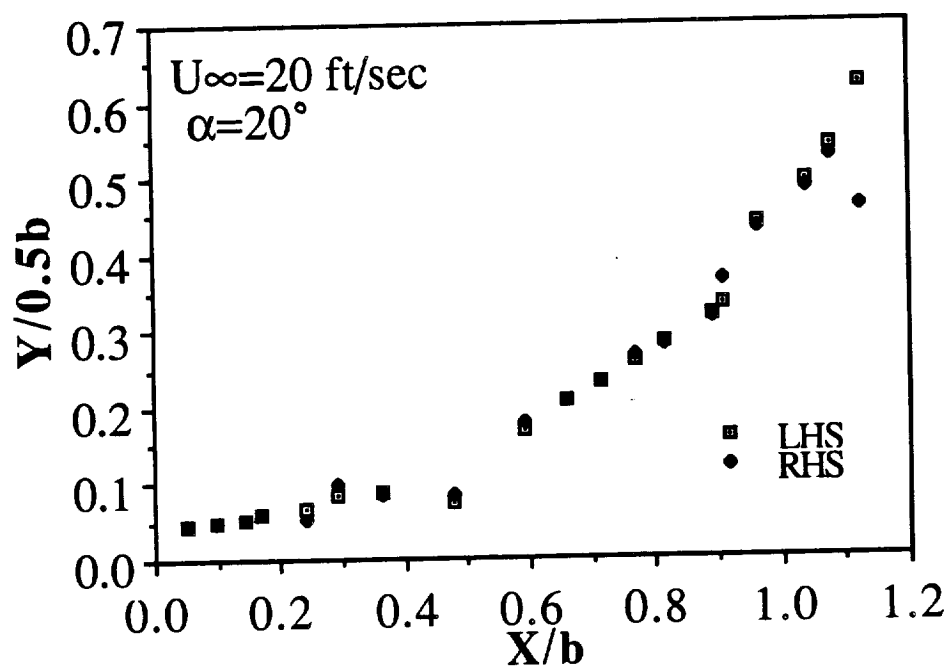
Fig.4.9a   Vortex positions located along one-half span of the model,
U_∞=20 ft/sec, α=20°
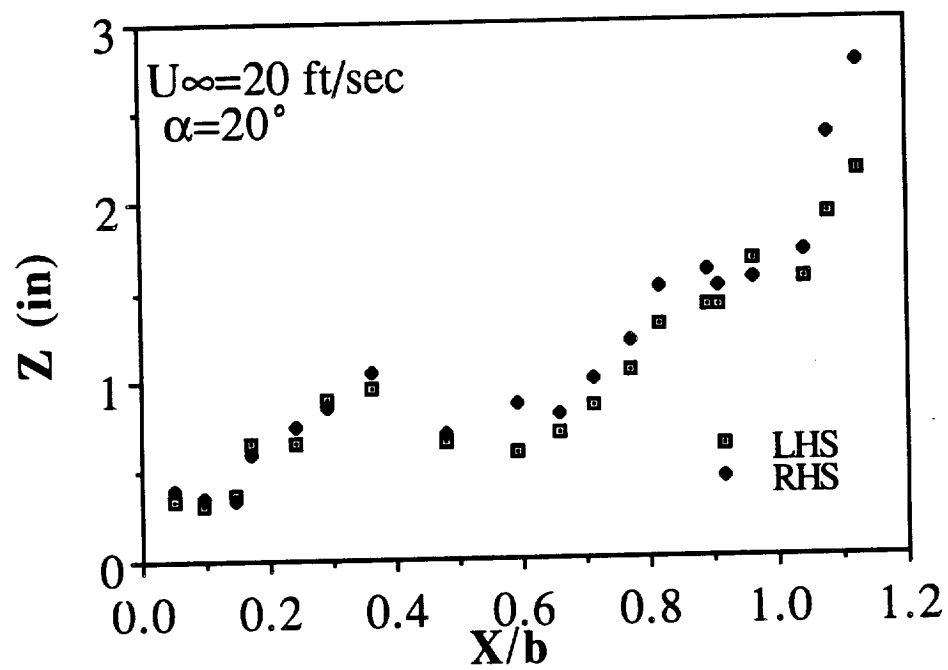
Fig.4.9b   Height of vortex cores along the model, U_∞=20 ft/sec, α=20°
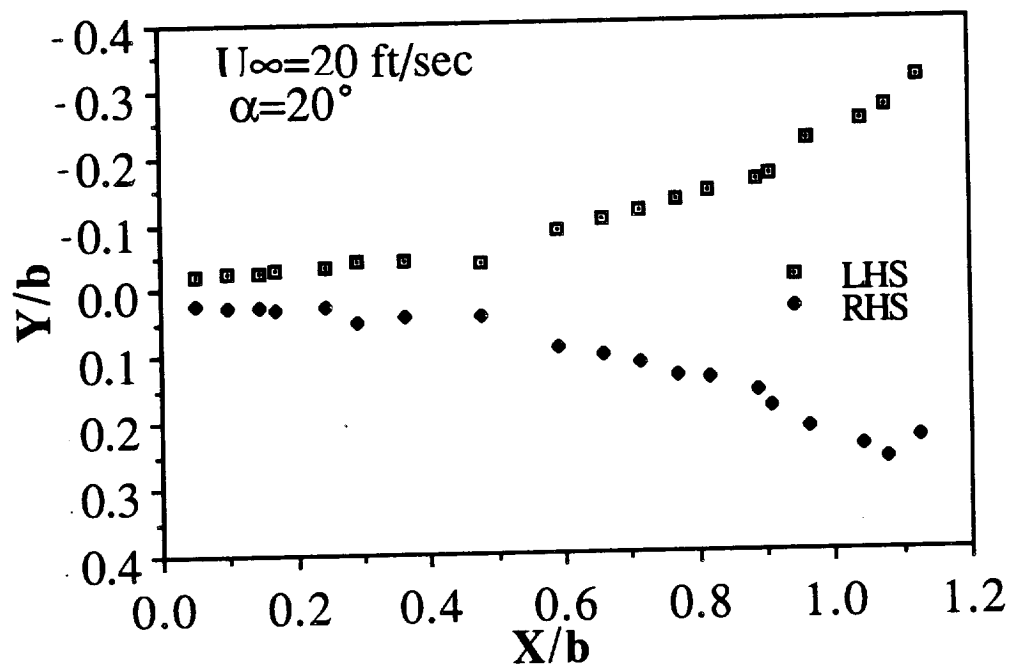
Fig.4.9c   Vortex core trajectory along the model, U_∞=20 ft/sec, α=20°
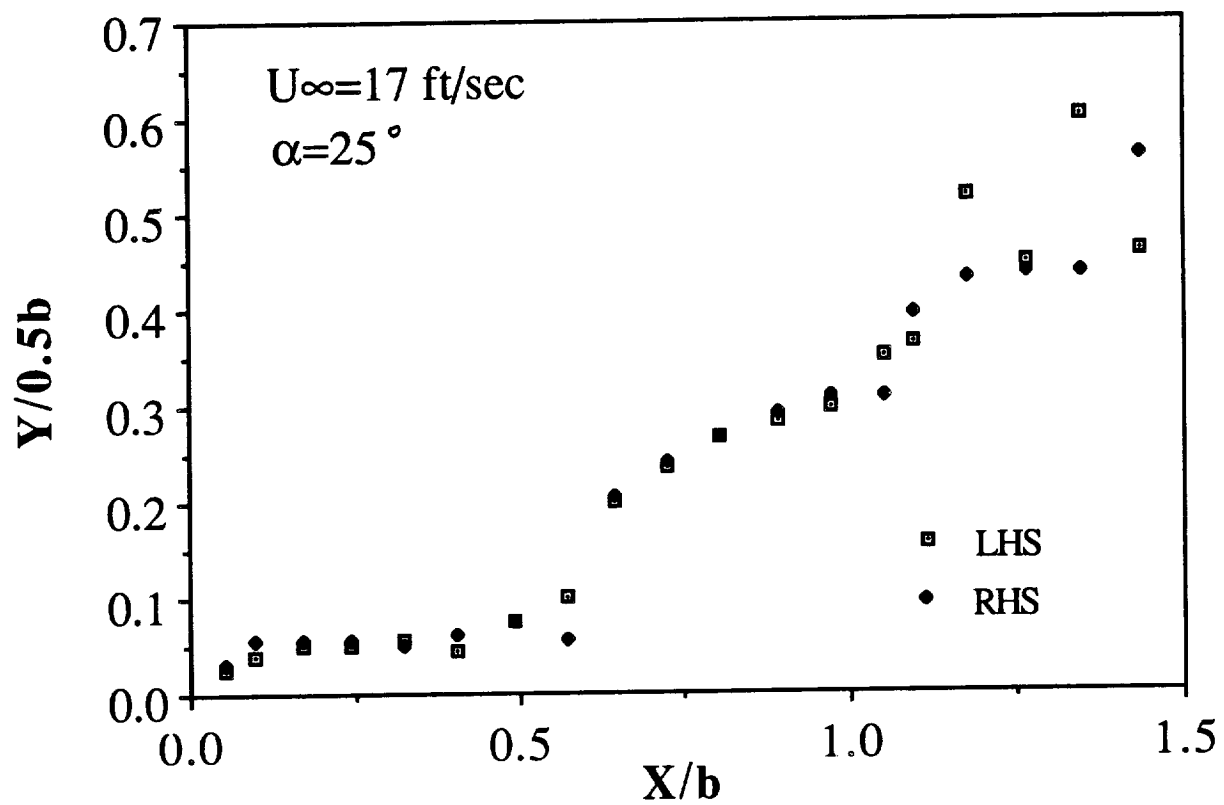
Fig.4.10a Vortex positions located along one-half span of the model,
U_∞=20 ft/sec, α=25°
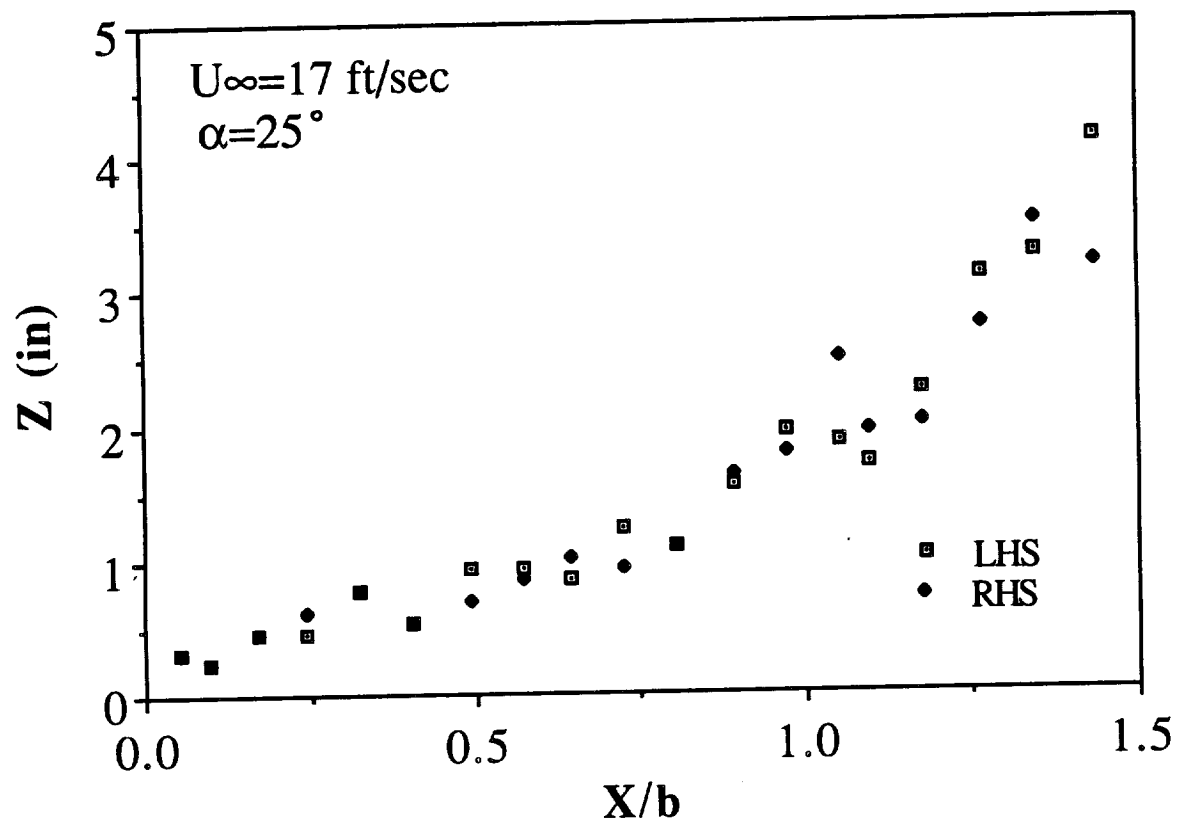
Fig.4.10b   Height of vortex cores along the model, U_∞=20 ft/sec, α=25°
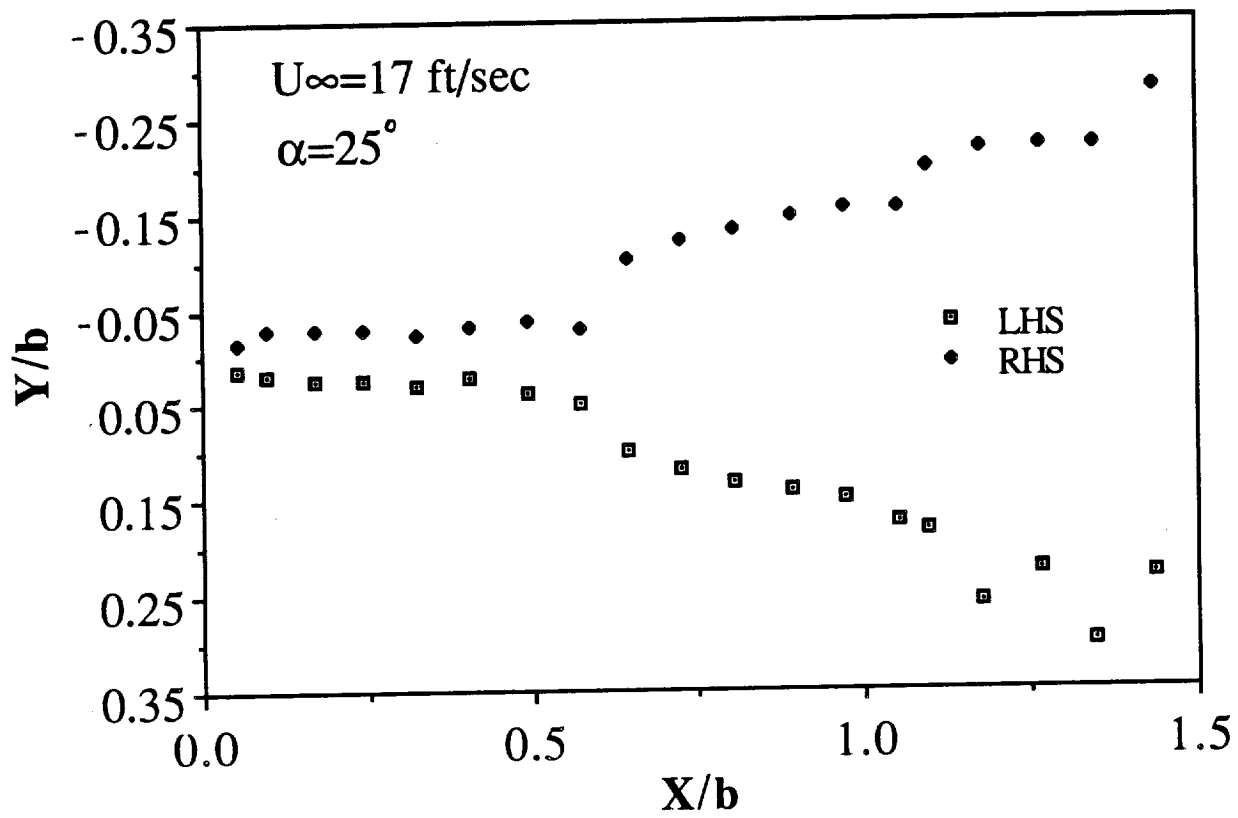
Fig.4.10c   Vortex core trajectory along the model, U∞=20 ft/sec, α=25°
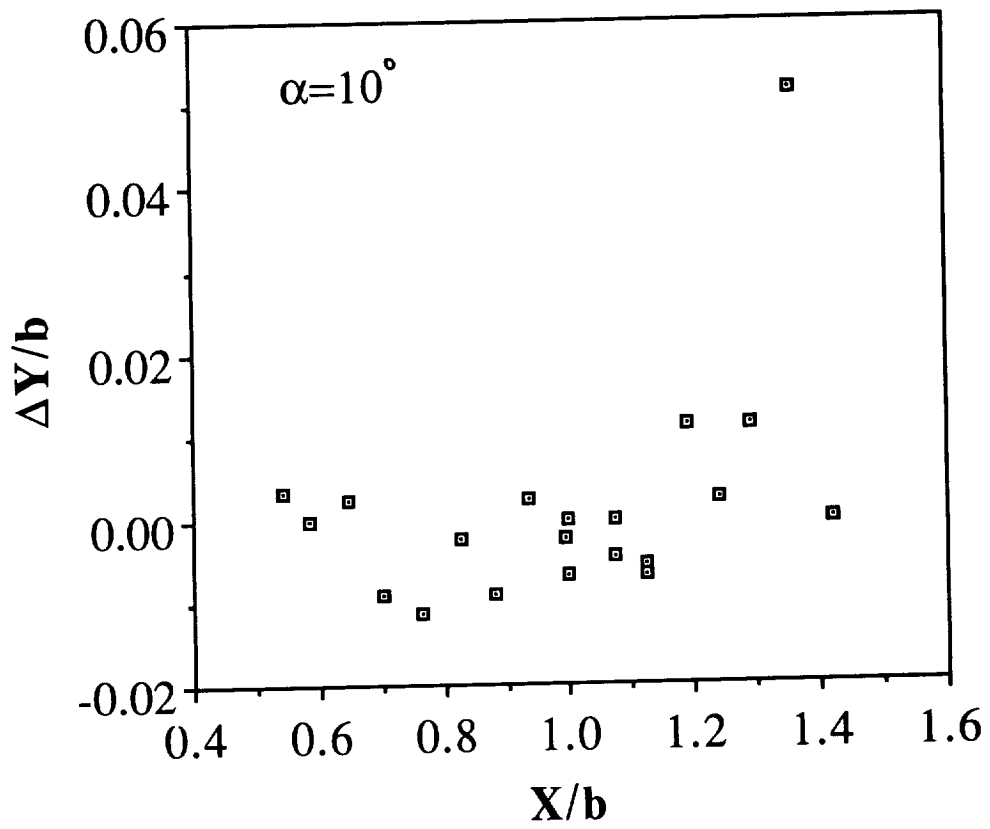
Fig.4.11a Difference in Y positions between LHS and RHS vortex for α=10°
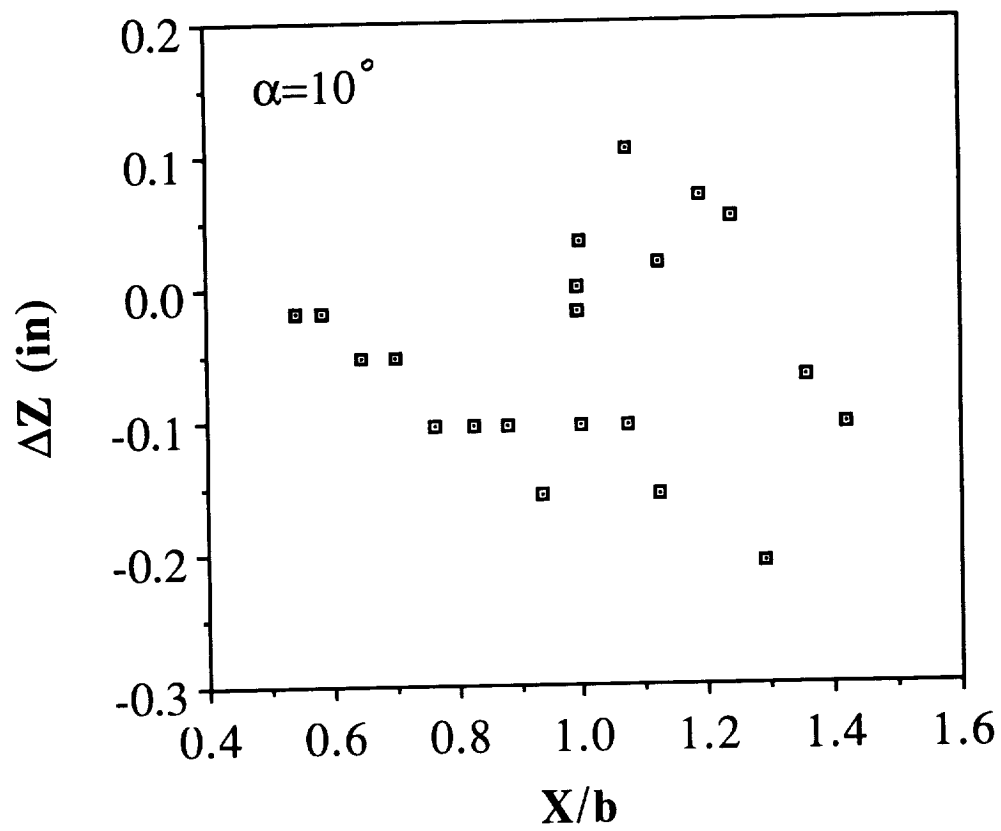
Fig.4.11b   Difference in Z positions between LHS and RHS vortex for $\alpha = 10^{\circ}$
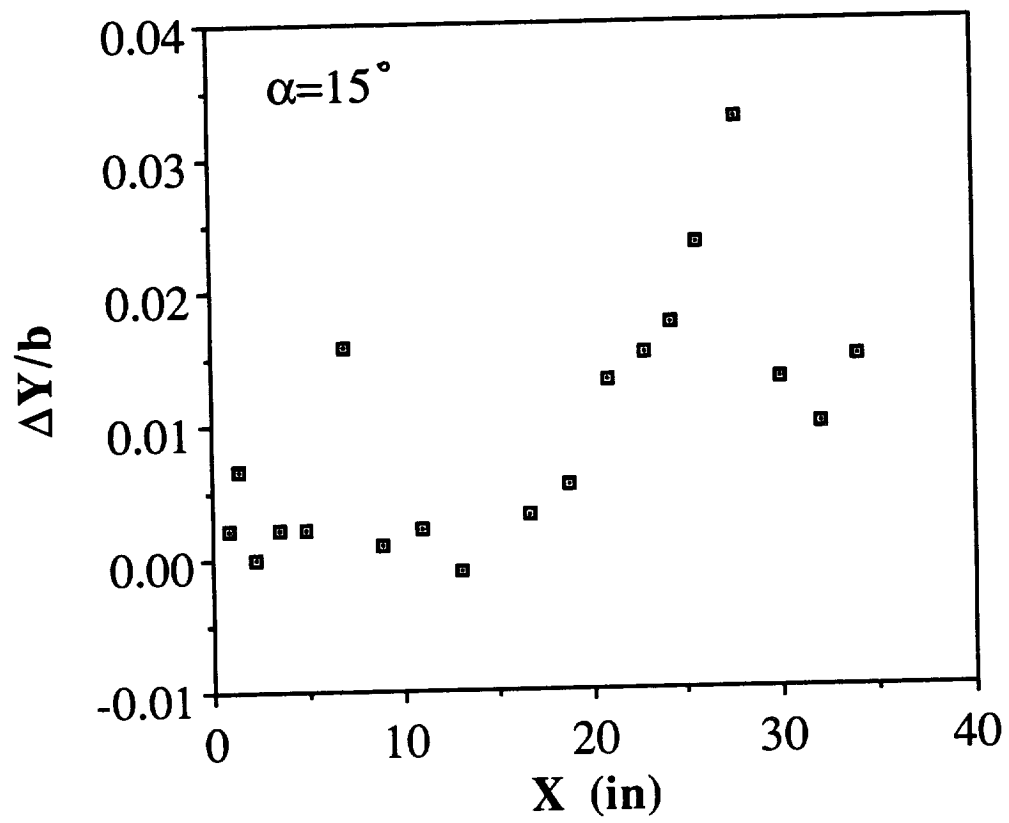
Fig.4.12a   Difference in Y positions between LHS and RHS vortex for $\alpha=15^\circ$
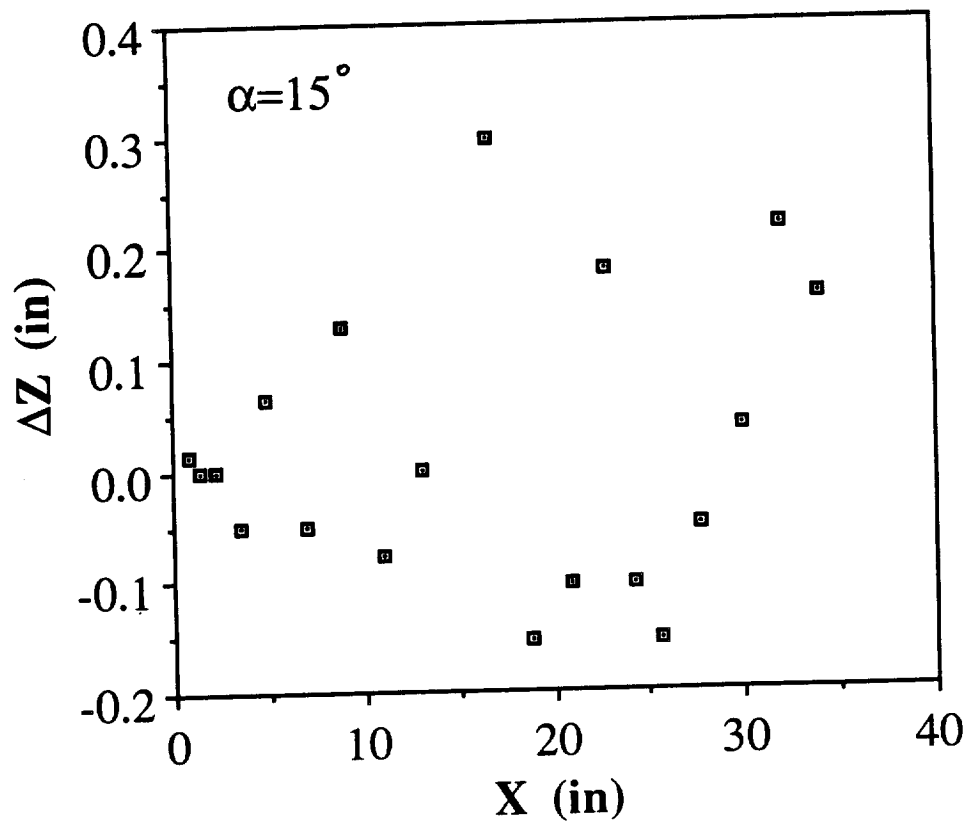
Fig.4.12b   Difference in Z positions between LHS and RHS vortex for $\alpha=15^o$
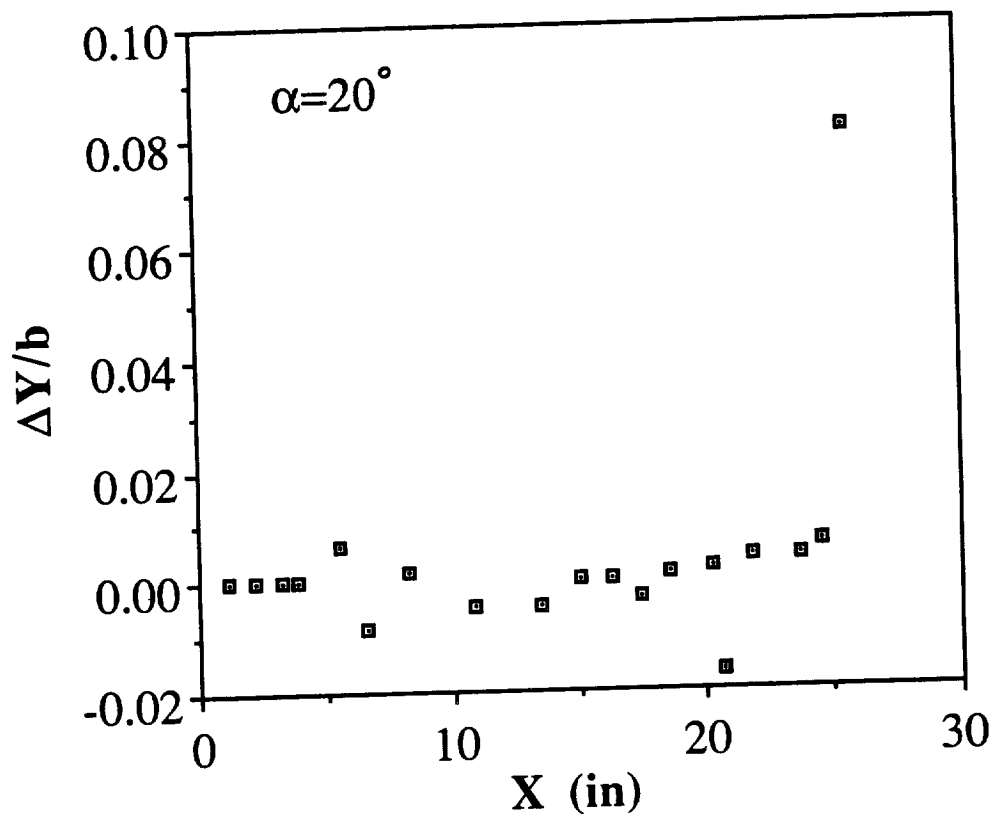
Fig.4.13a   Difference in Y positions between LHS and RHS vortex for α=20⁰

Fig.4.13b   Difference in Z positions between LHS and RHS vortex for $\alpha=20^{\circ}$
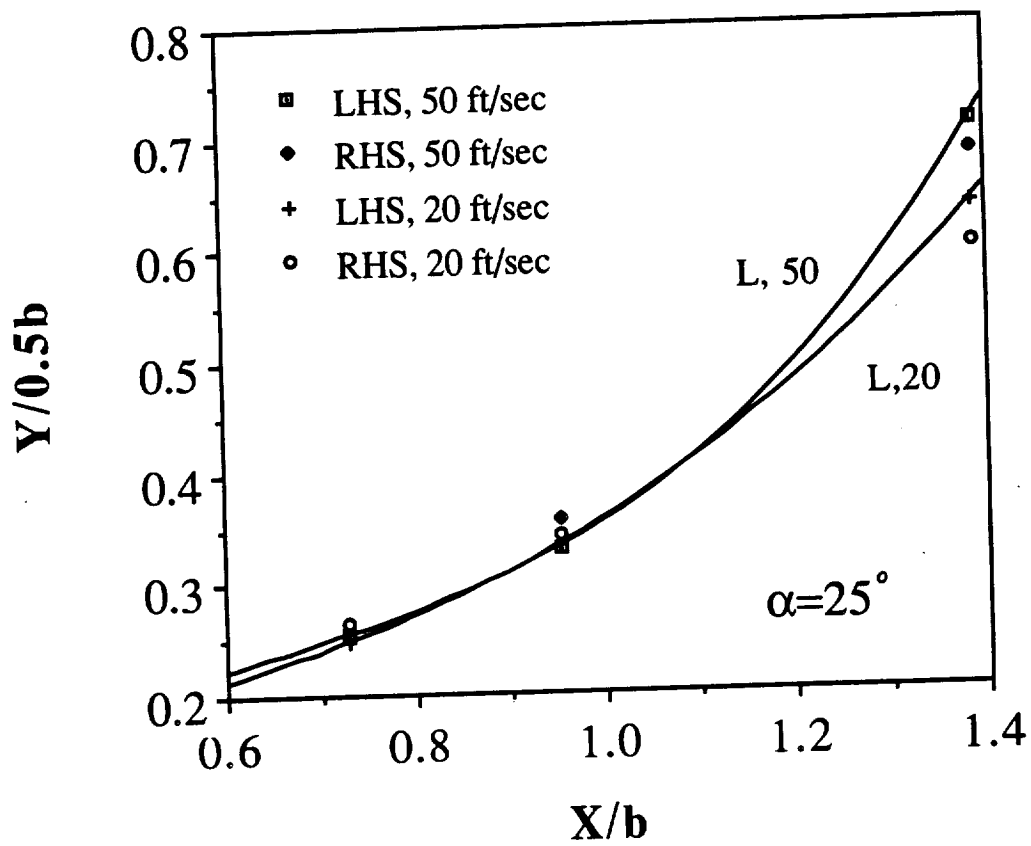
Fig.4.14a   Comparison on Y position for LHS vortex under different freestream speeds
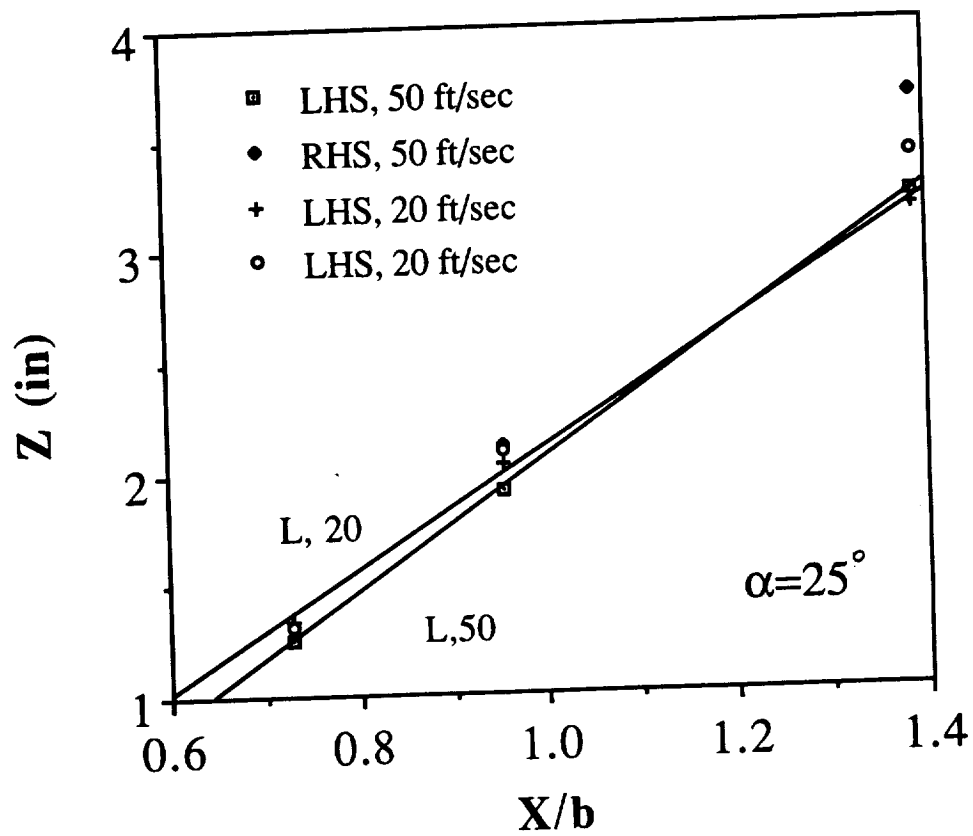
Fig.4.14b   Comparison on Z position for LHS vortex under different freestream speeds
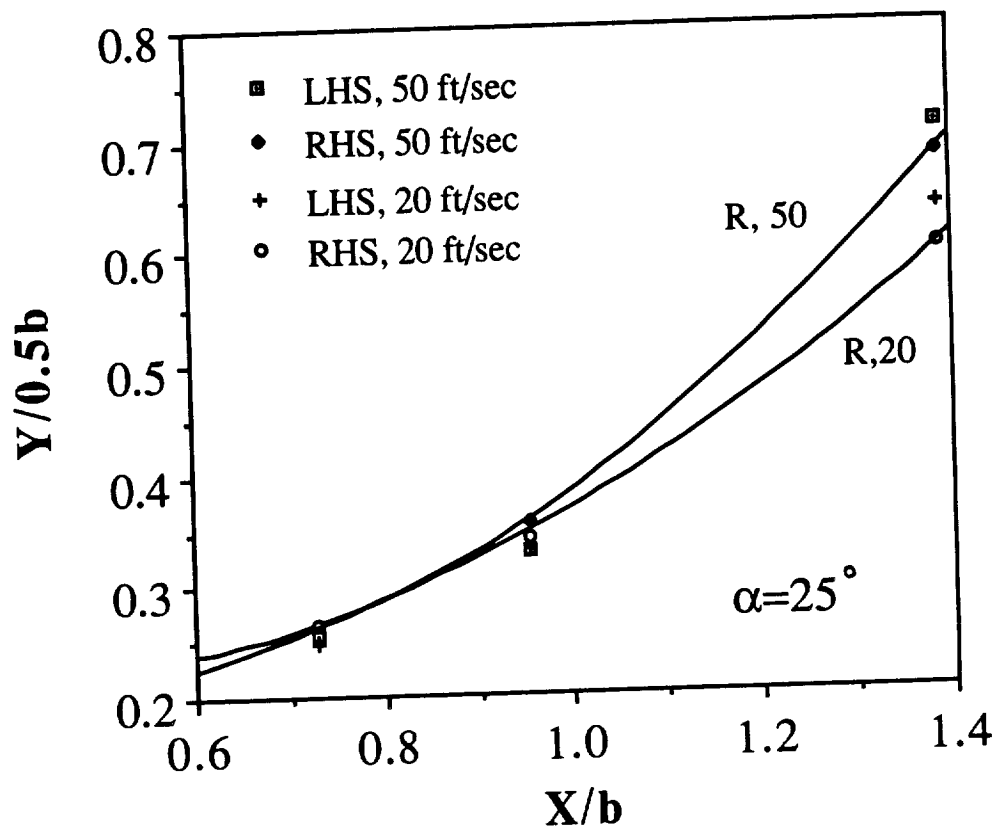
Fig.4.14c   Comparison on Y position for RHS vortex under different freestream
speeds
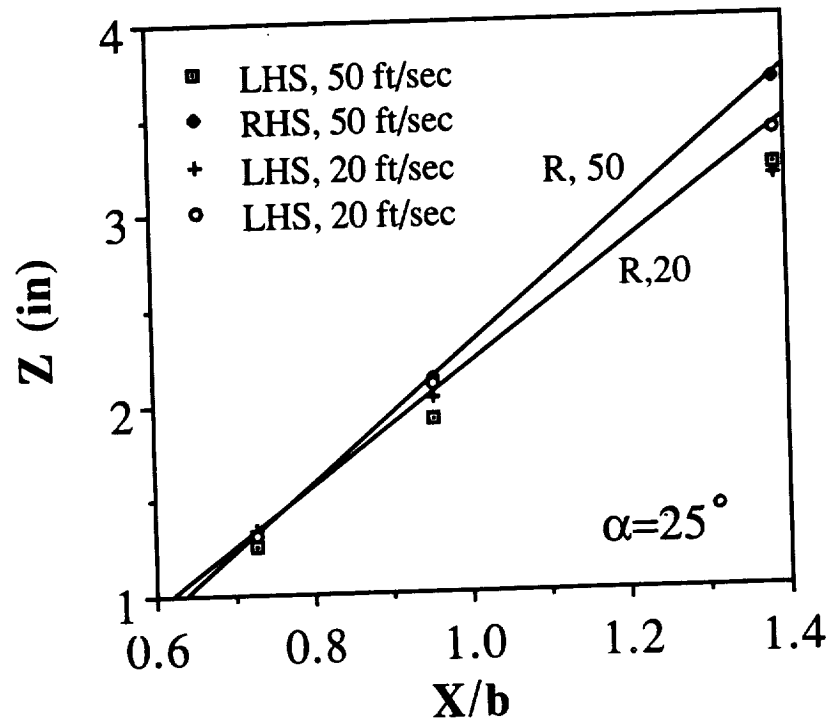
Fig.4.14d   Comparison on Z position for RHS vortex under different freestream speeds
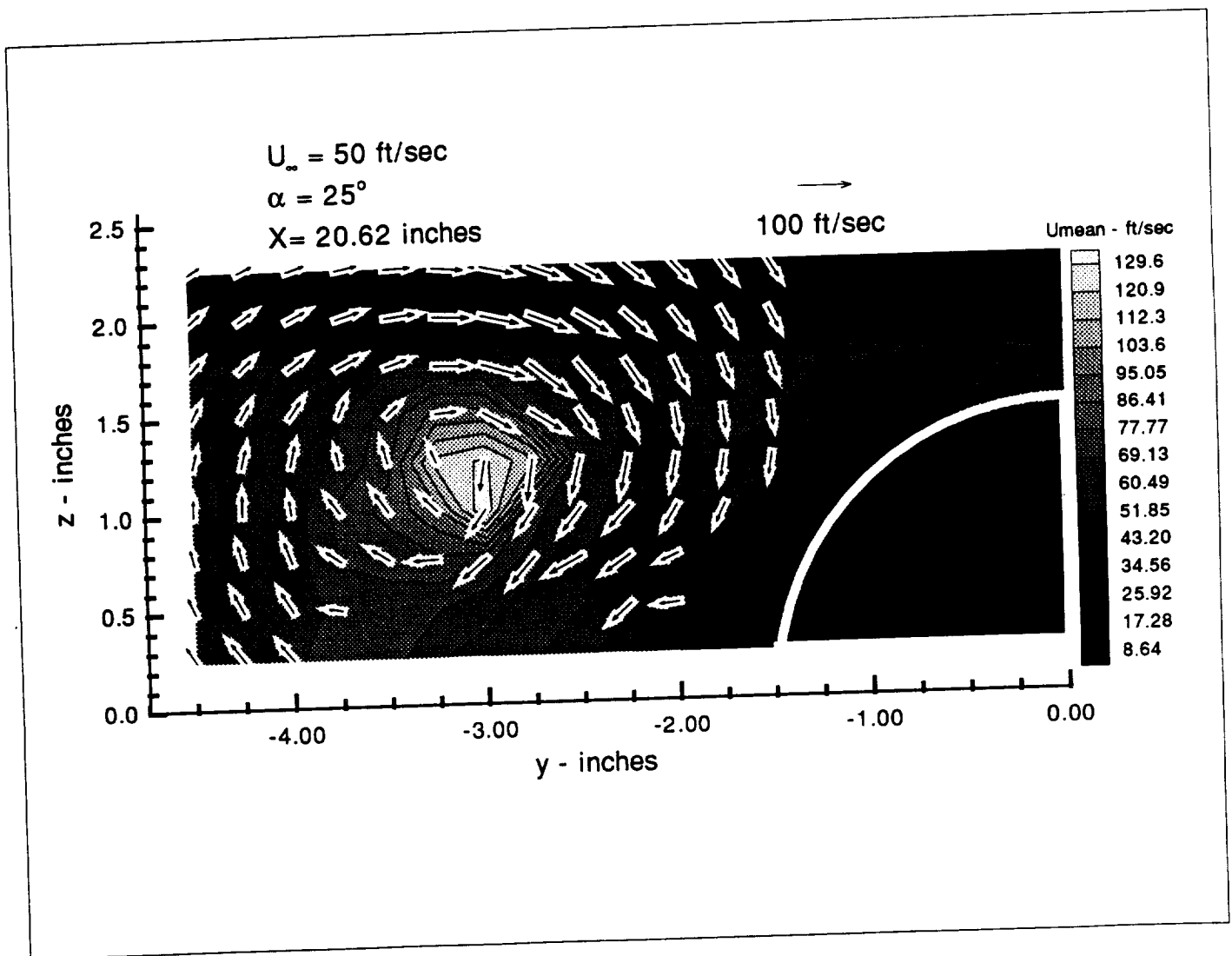
Fig.4.15a   Velocity field from LDV measurements at station 1, U_∞=50 ft/sec, α=25°
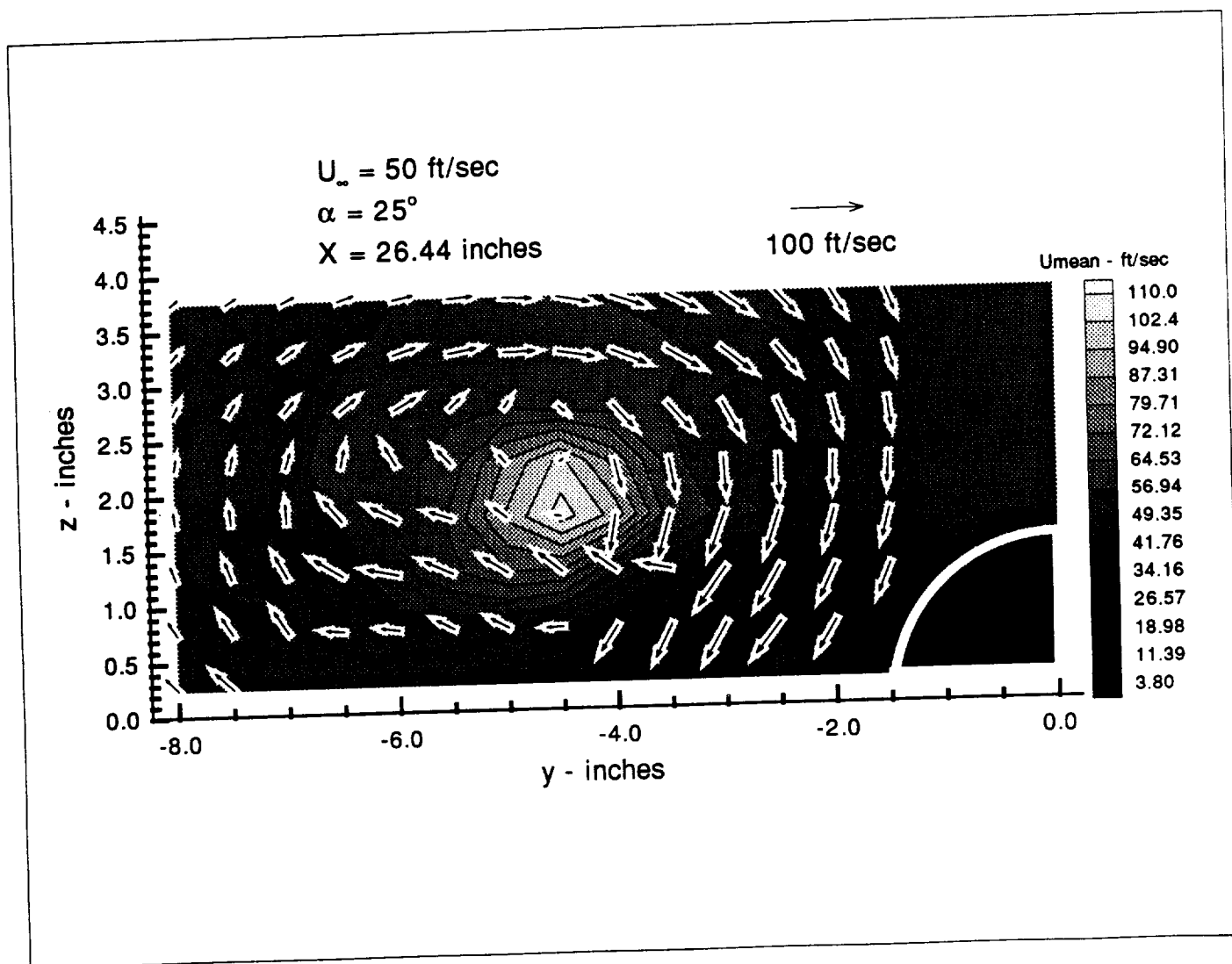
Fig.4.15b Velocity field from LDV measurements at station 2, U_∞=50 ft/sec, α=25°
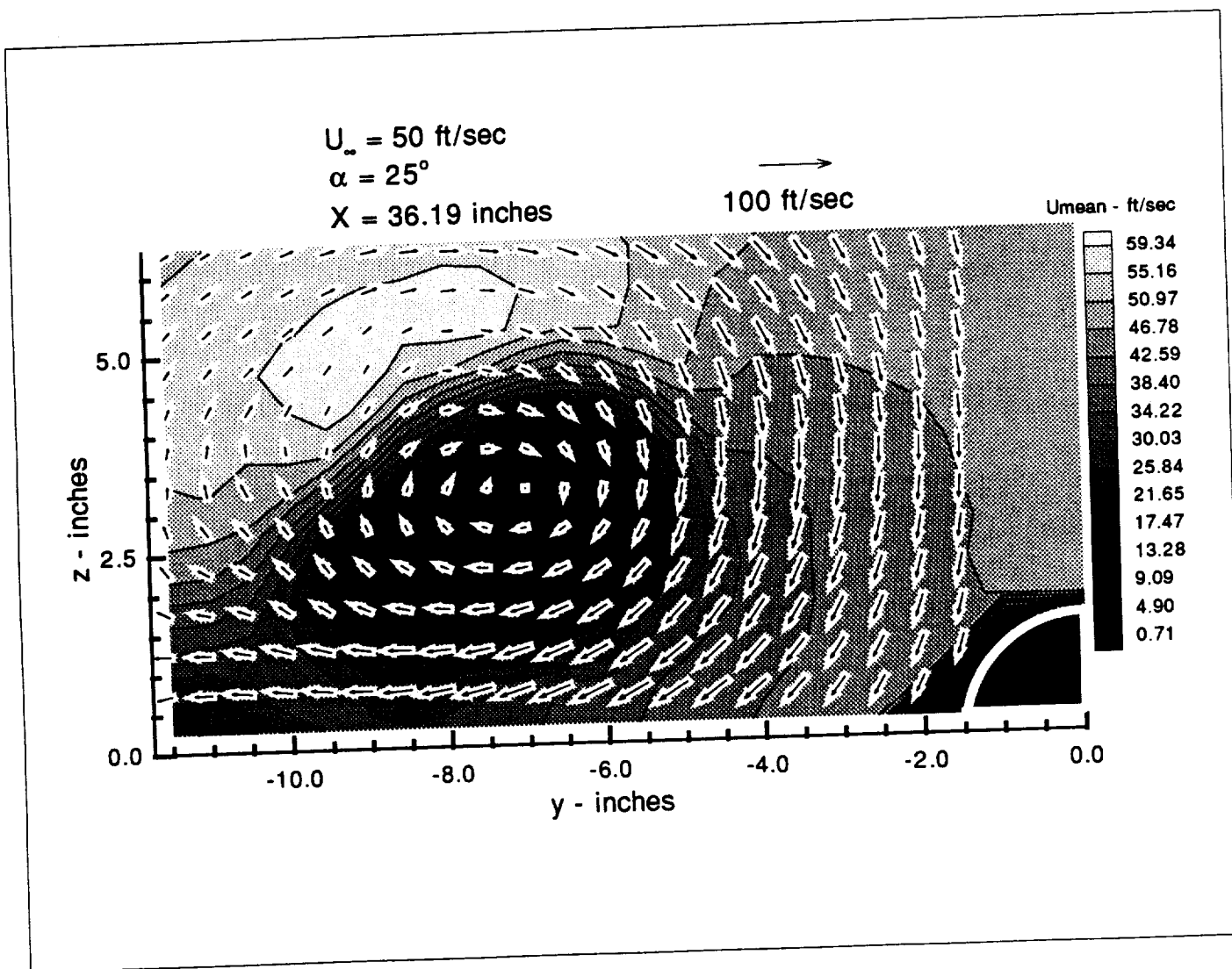
Fig.4.15c Velocity field from LDV measurements at station 3, U_∞=50 ft/sec, α=25°
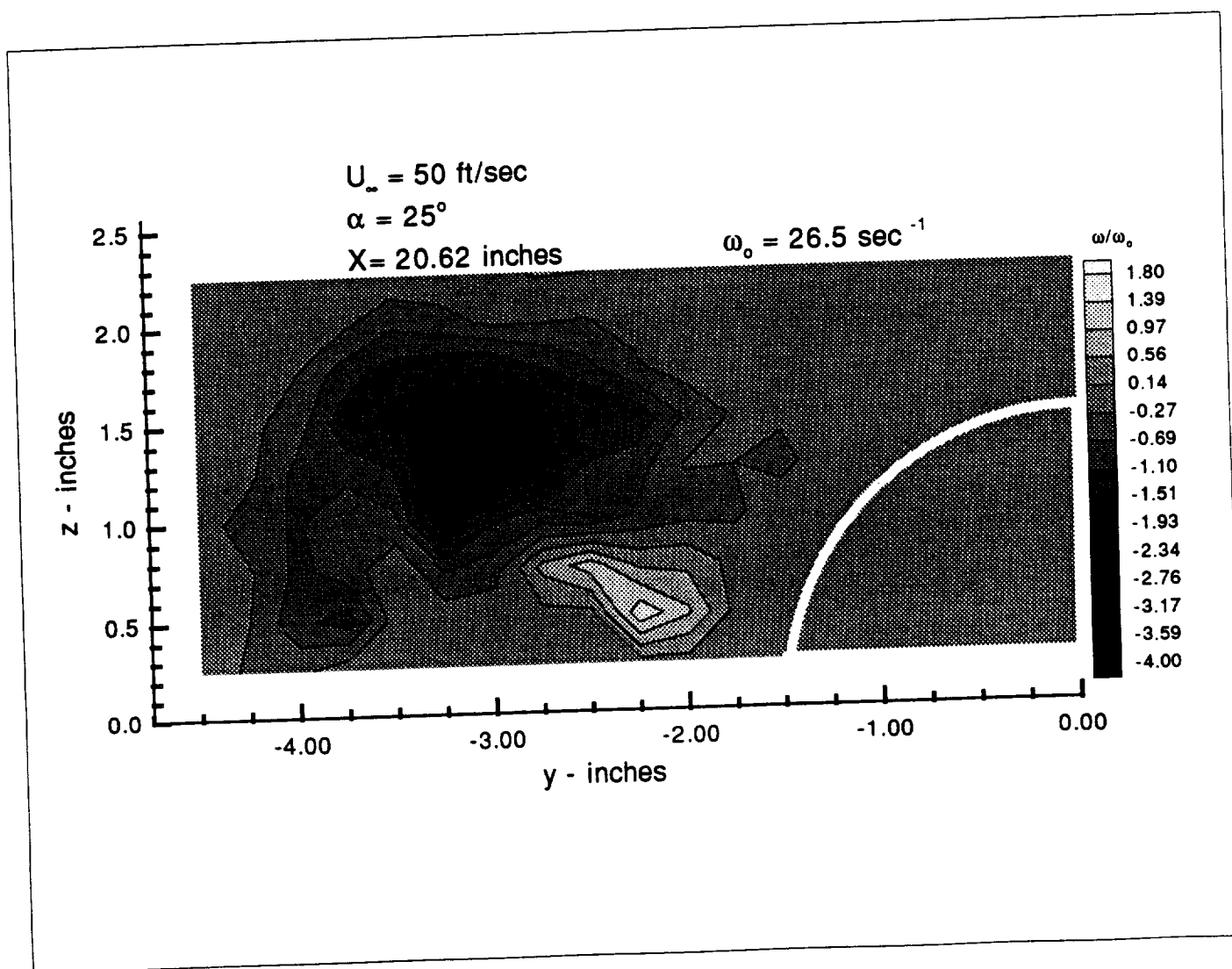
Fig.4.16a Vorticity contours at LDV station 1
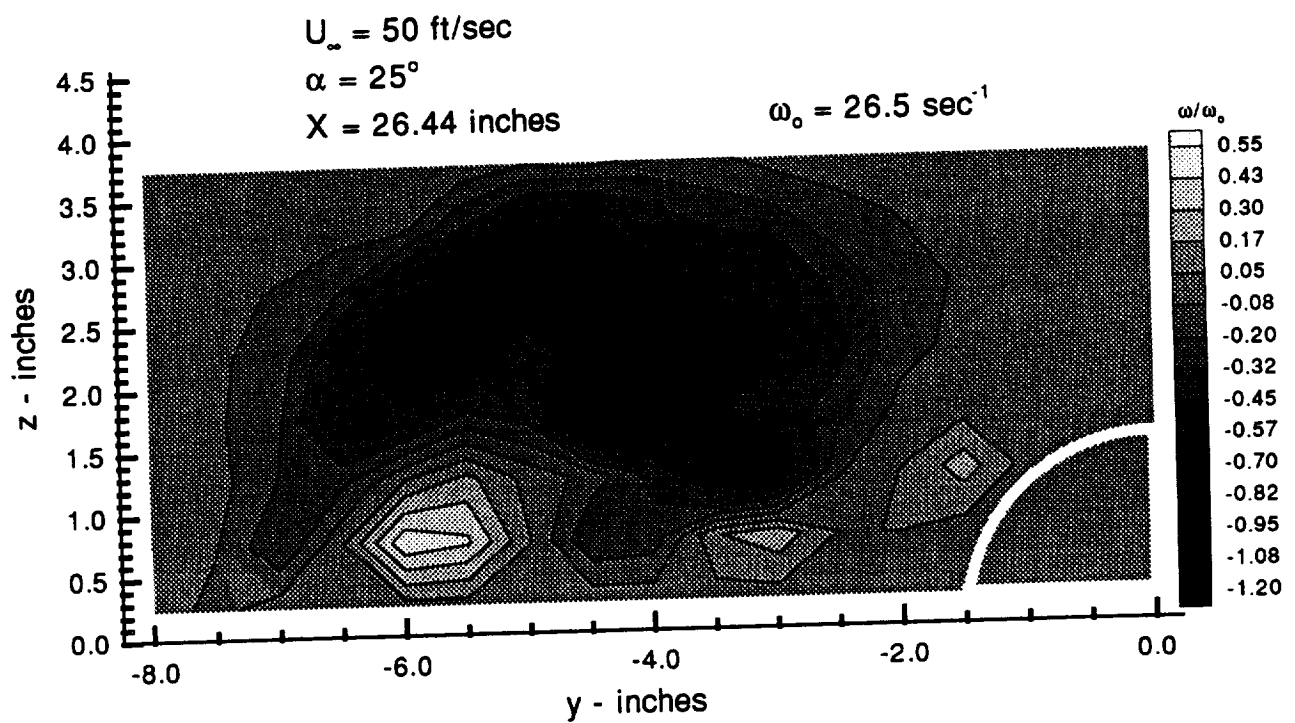
Fig.4.16b   Vorticity contours at LDV station 2

$U_\infty = 50$ ft/sec
$\alpha = 25°$
$X = 36.19$ inches
$\omega_o = 26.5$ sec^{-1}

ω/ω_o

| 0.15 |
| 0.11 |
| 0.08 |
| 0.04 |
| 0.00 |
| -0.04 |
| -0.07 |
| -0.11 |
| -0.15 |
| -0.18 |
| -0.22 |
| -0.26 |
| -0.30 |
| -0.33 |
| -0.37 |

z - inches
y - inches
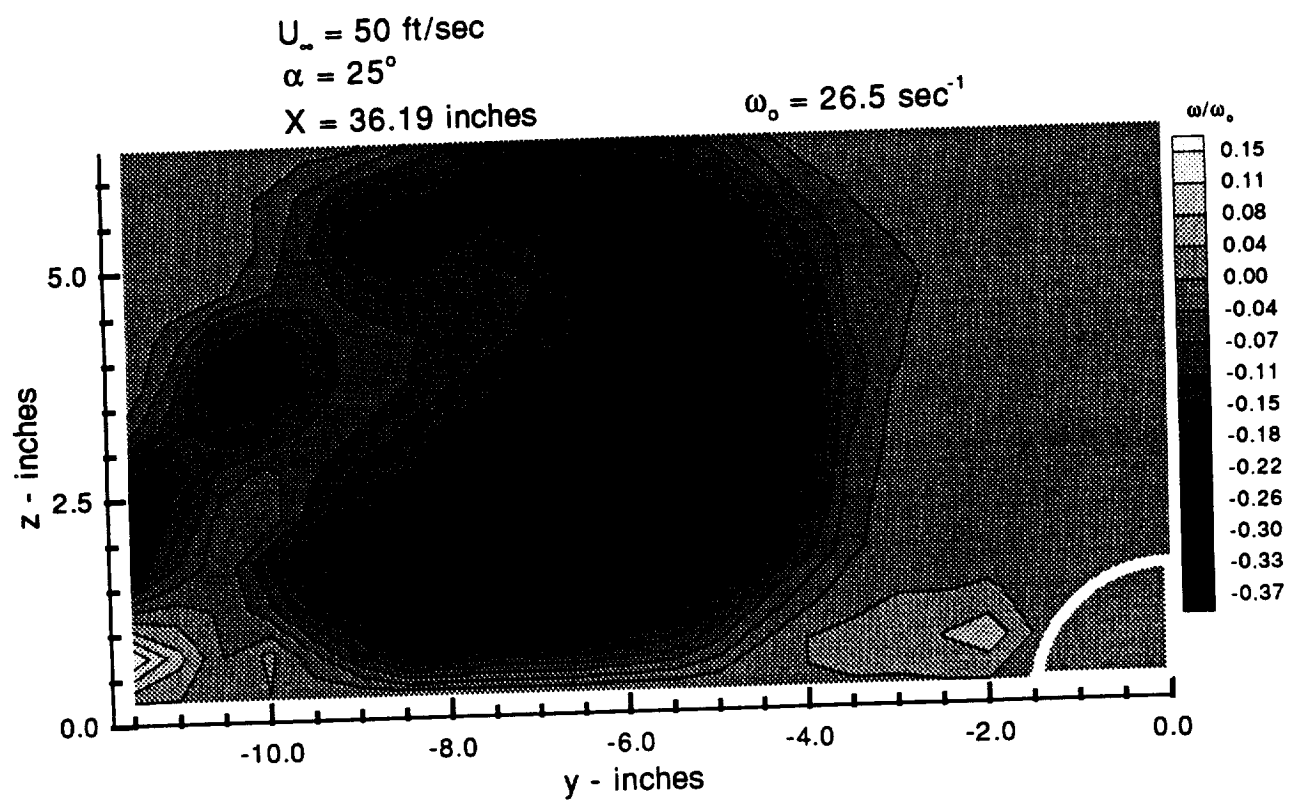
Fig.4.16c   Vorticity contours at LDV station 3
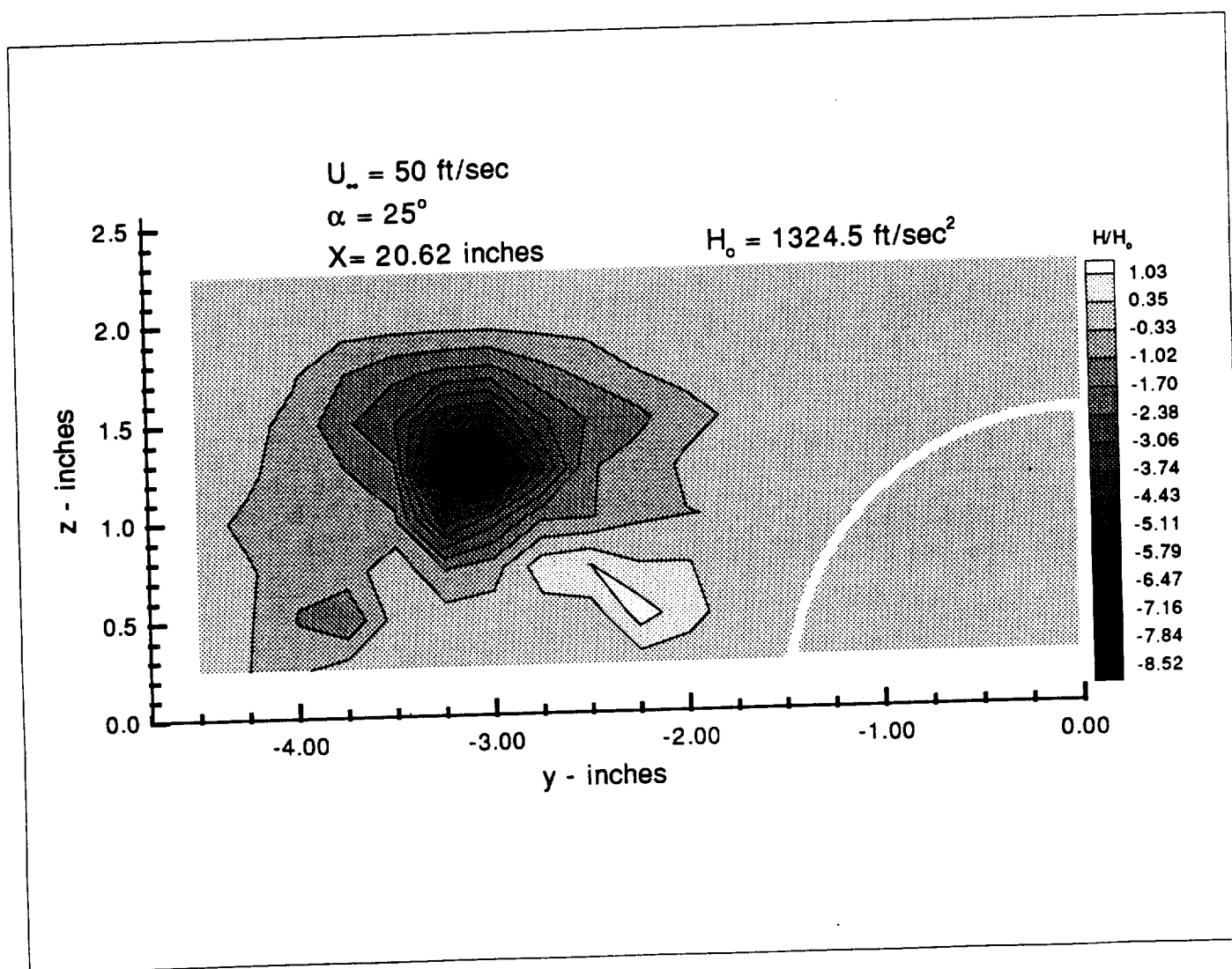
Fig.4.17a Helicity contours at LDV station 1
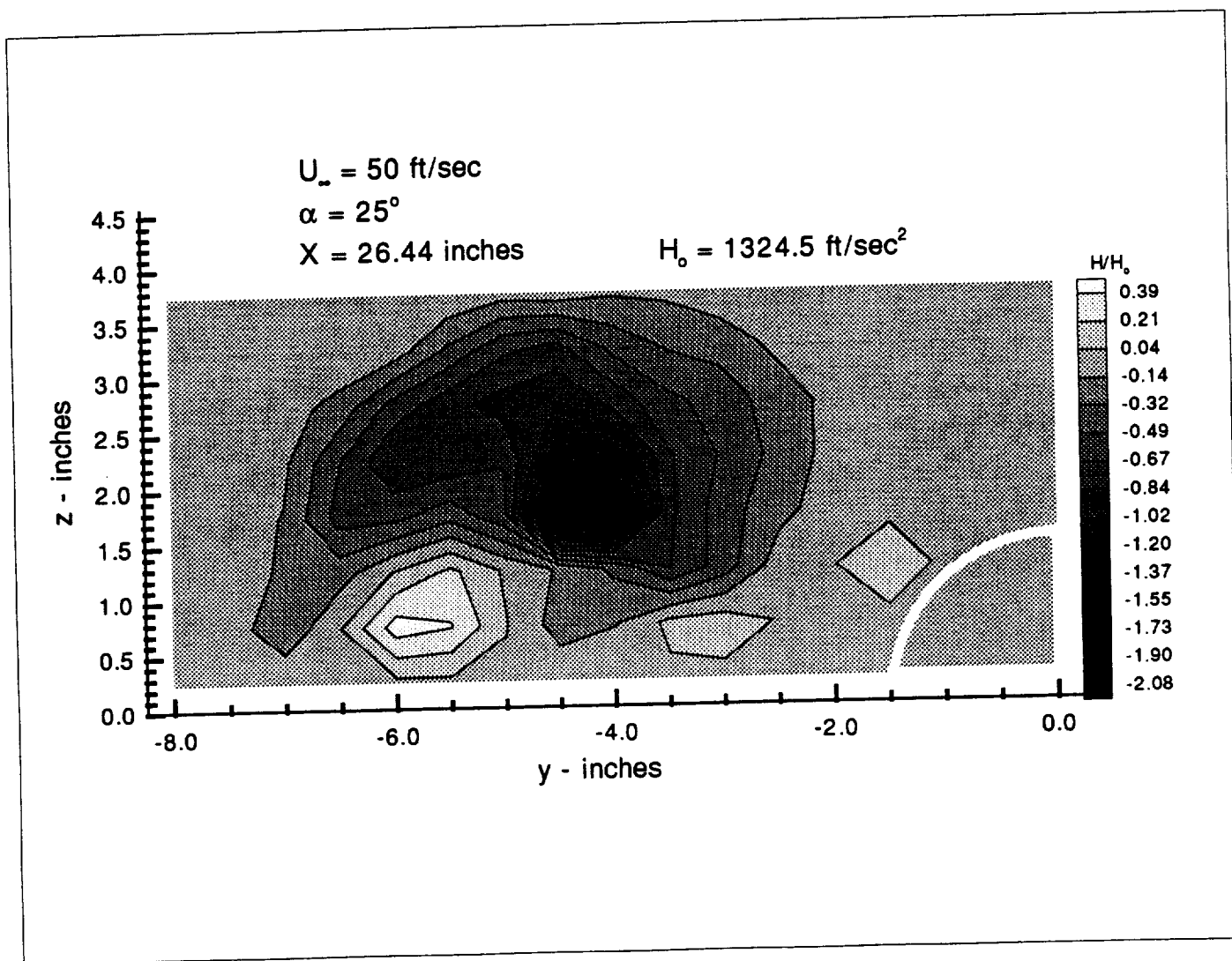
Fig.4.17b   Helicity contours at LDV station 2

U_∞ = 50 ft/sec

α = 25°

X = 36.19 inches

H_o = 1324.5 ft/sec^2

H/H$_o$

| 0.70 |
| 0.43 |
| 0.17 |
| -0.10 |
| -0.37 |
| -0.63 |
| -0.90 |
| -1.17 |
| -1.43 |
| -1.70 |
| -1.97 |
| -2.23 |
| -2.50 |
| -2.77 |
| -3.03 |

z - inches

y - inches
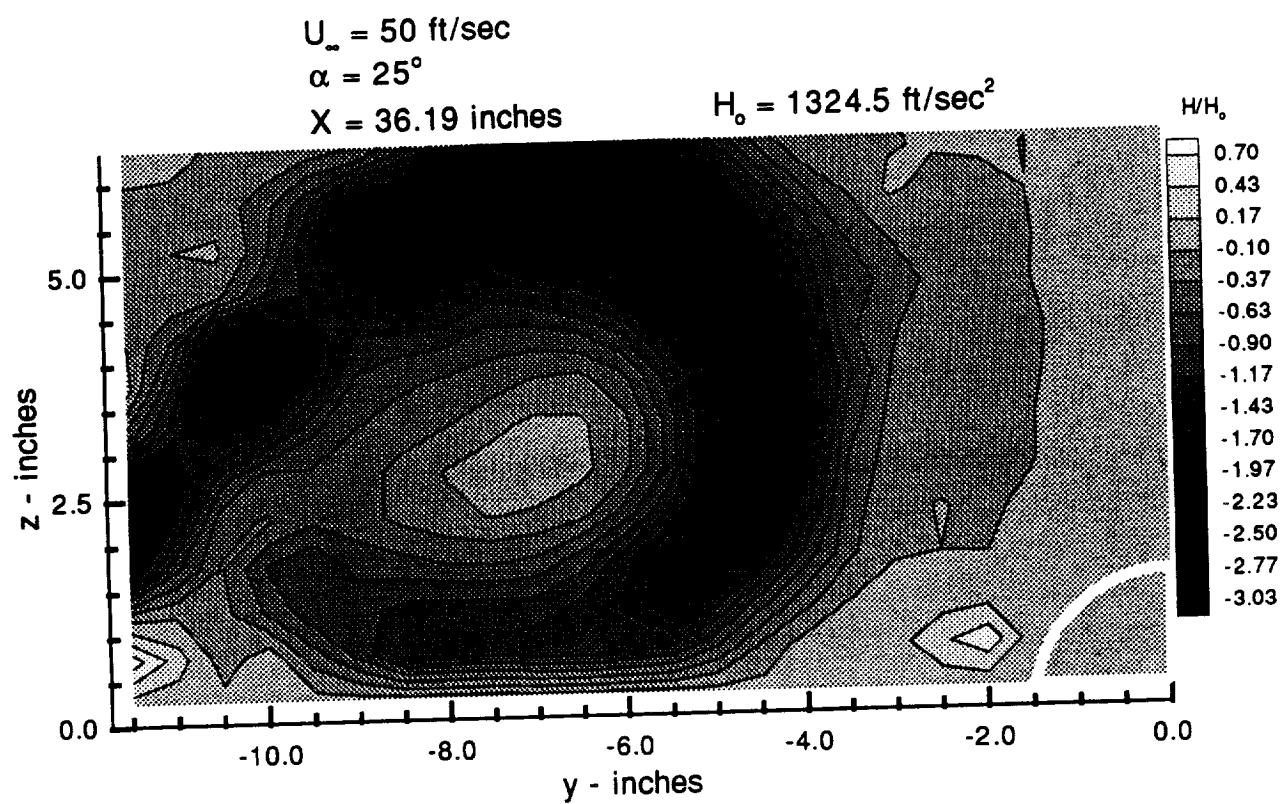
Fig.4.17c   Helicity contours at LDV station 3
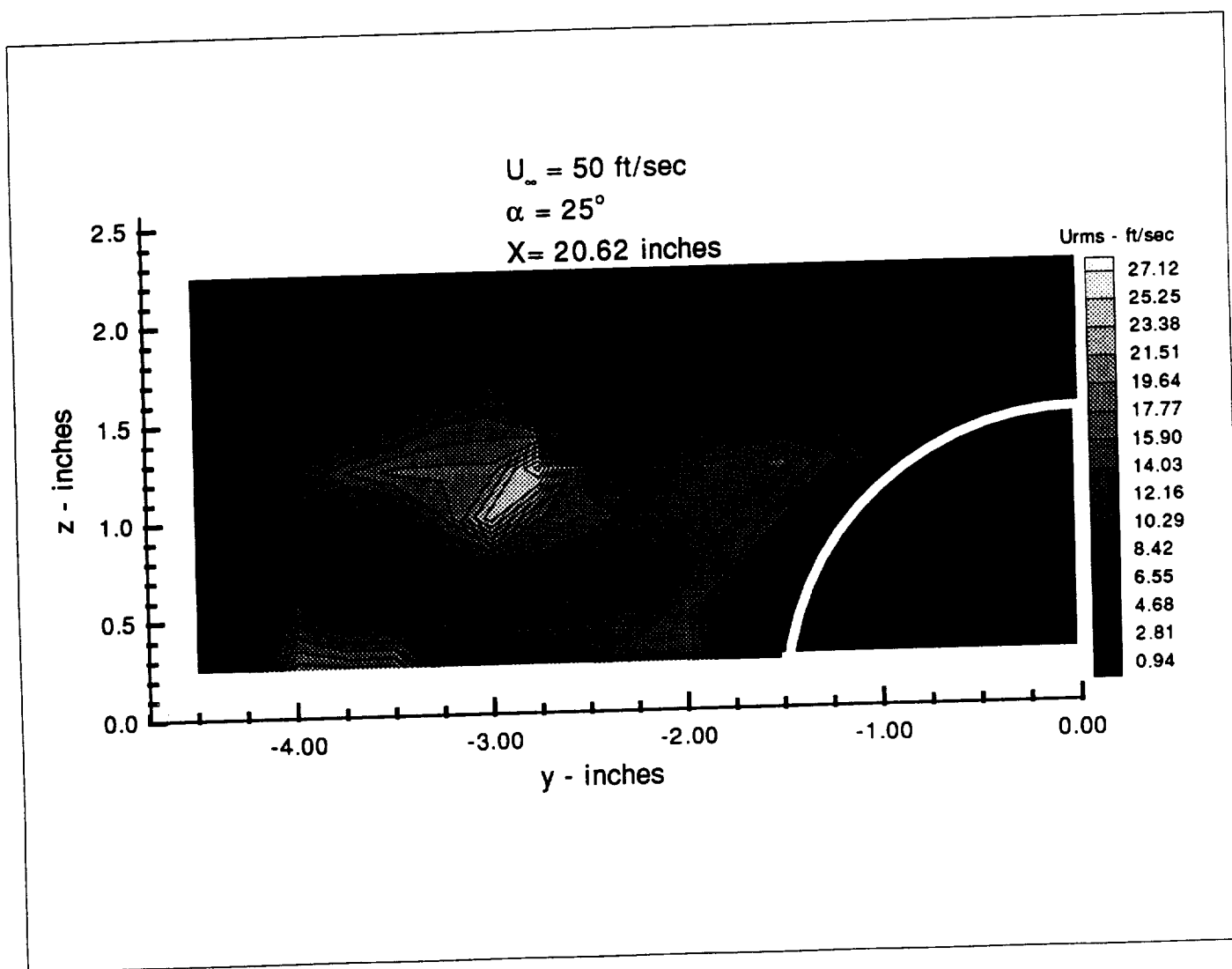
Fig.4.18a   RMS velocity contours (U-component) at LDV station 1

$U_\infty = 50$ ft/sec

$\alpha = 25°$

$X = 20.62$ inches

Vrms - ft/sec

| 30.37 |
| 28.28 |
| 26.18 |
| 24.09 |
| 21.99 |
| 19.90 |
| 17.80 |
| 15.71 |
| 13.61 |
| 11.52 |
| 9.43 |
| 7.33 |
| 5.24 |
| 3.14 |
| 1.05 |

z - inches

2.5

2.0

1.5

1.0

0.5

0.0

-4.00   -3.00   -2.00   -1.00   0.00

y - inches
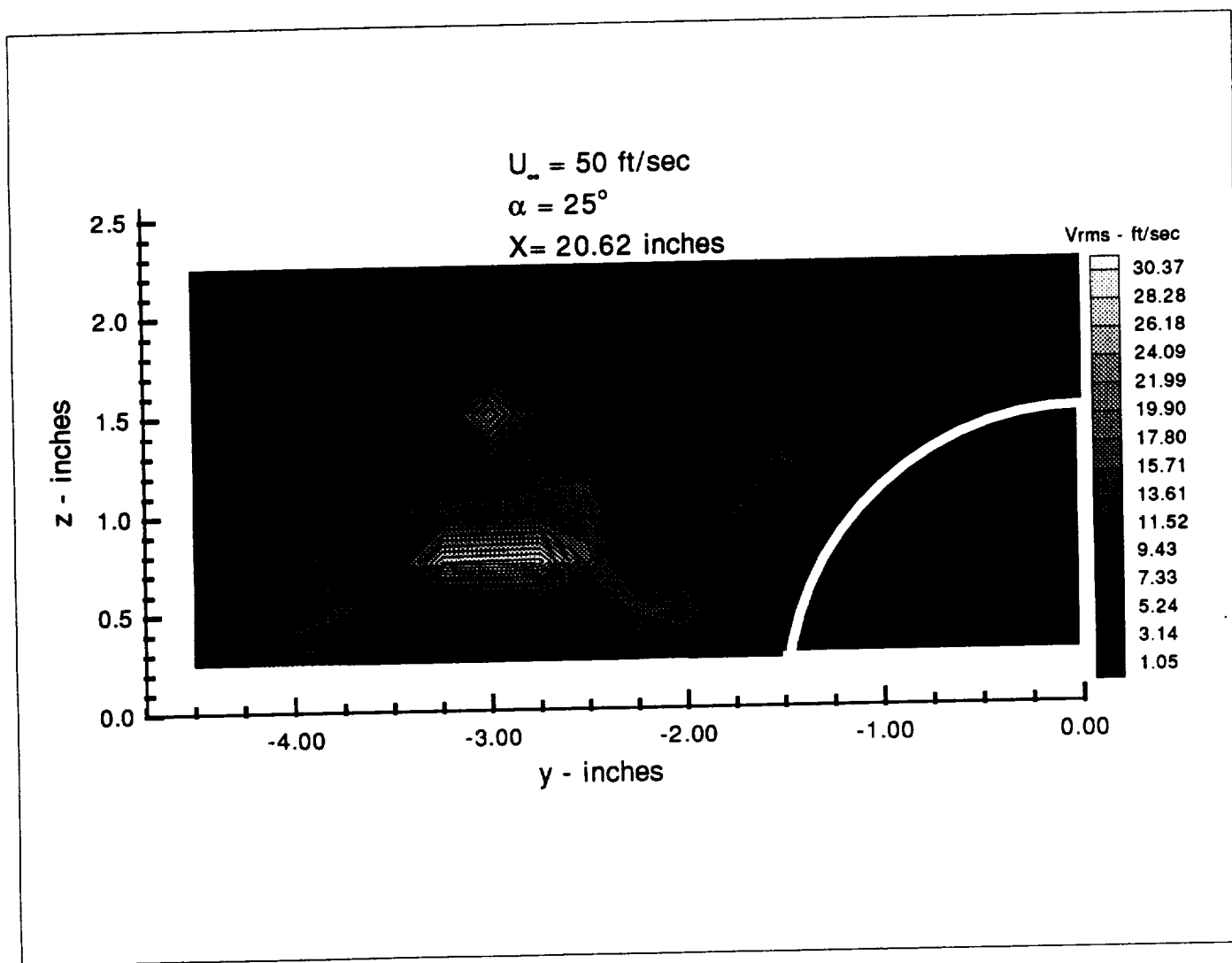
Fig.4.18b   RMS velocity contours (V-component) at LDV station 1
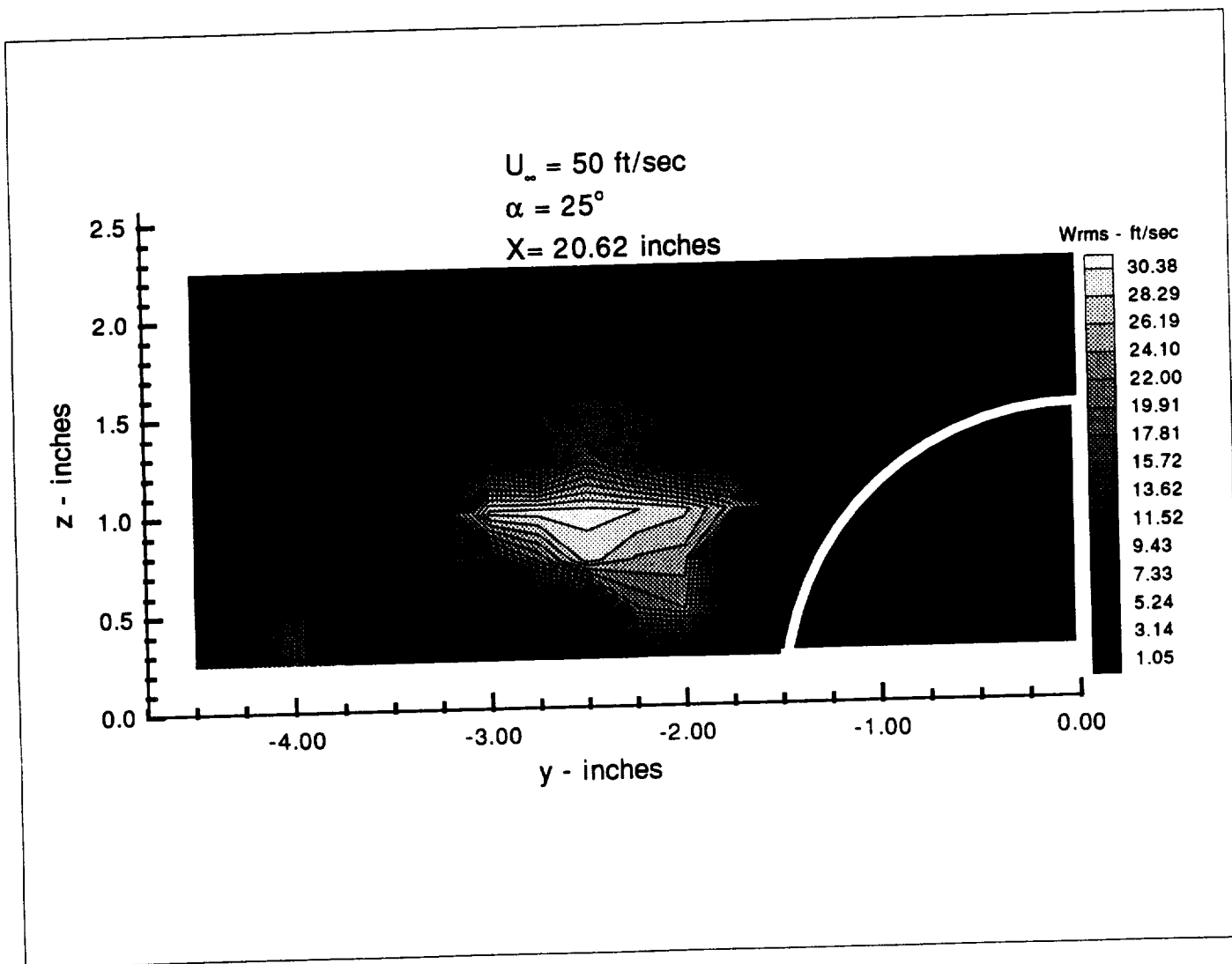
Fig.4.18c RMS velocity contours (W-component) at LDV station 1

$U_\infty = 50$ ft/sec

$\alpha = 25°$

$X = 26.44$ inches
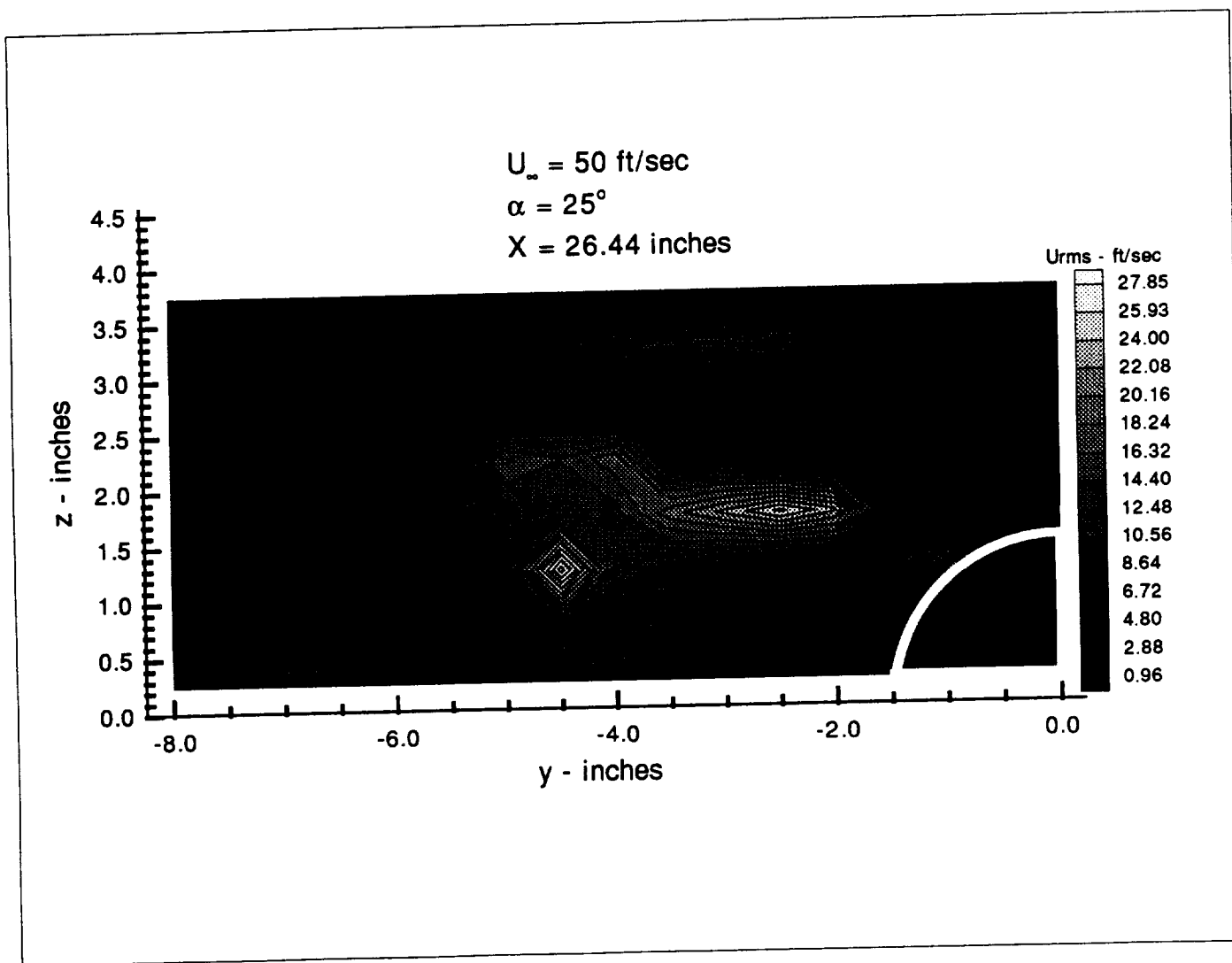
Fig.4.19a   RMS velocity contours (U-component) at LDV station 2
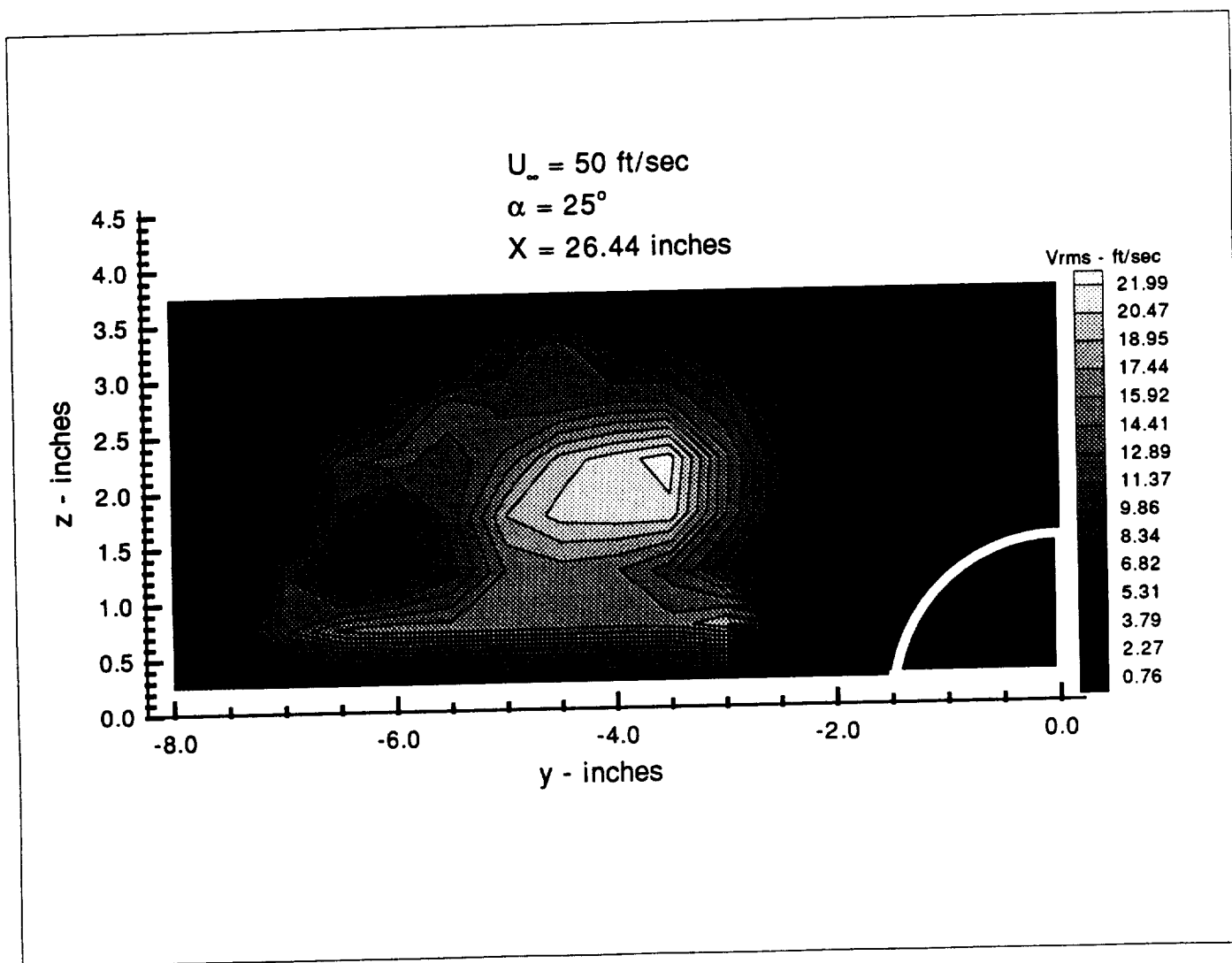
Fig.4.19b   RMS velocity contours (V-component) at LDV station 2
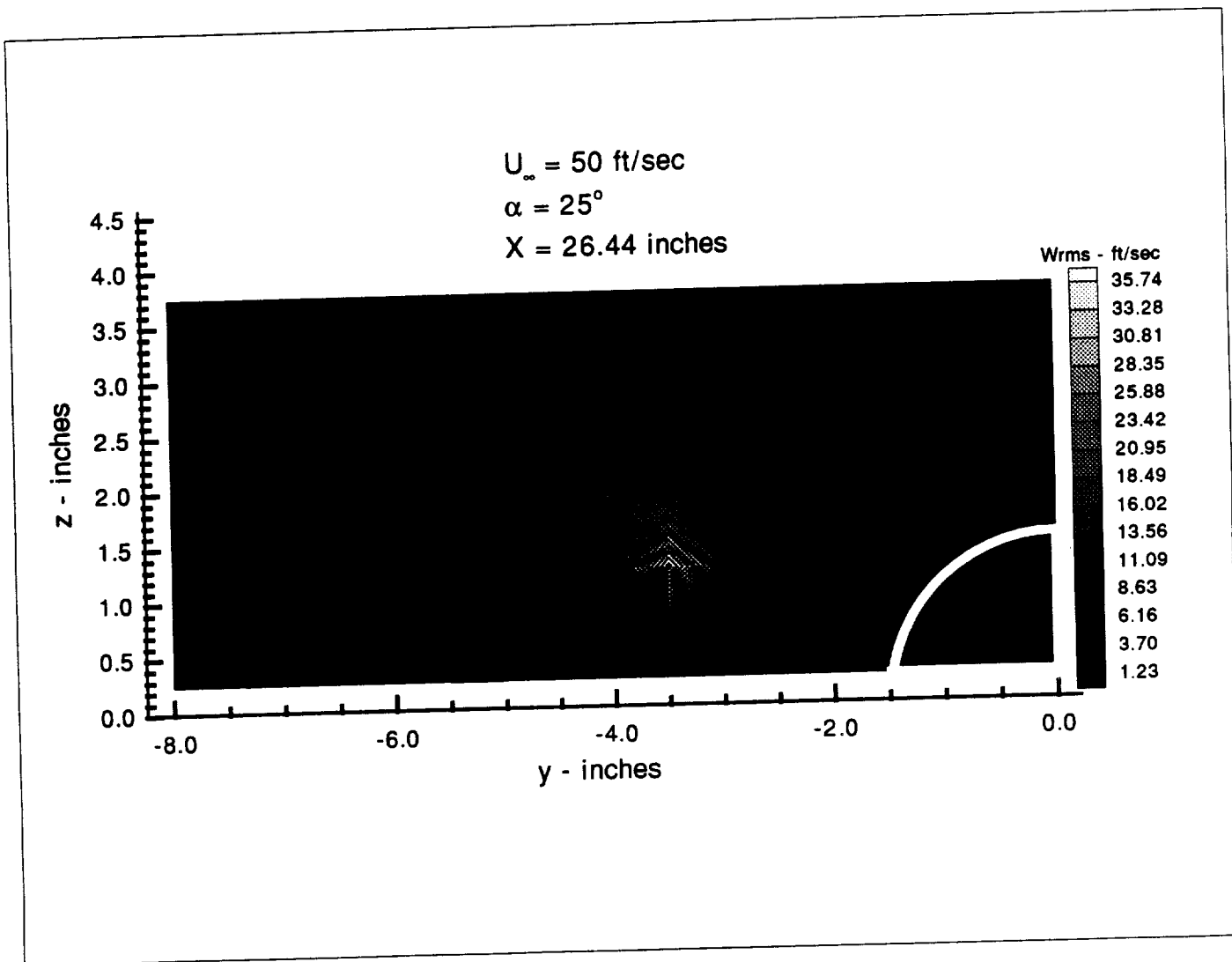
Fig.4.19c   RMS velocity contours (W-component) at LDV station 2
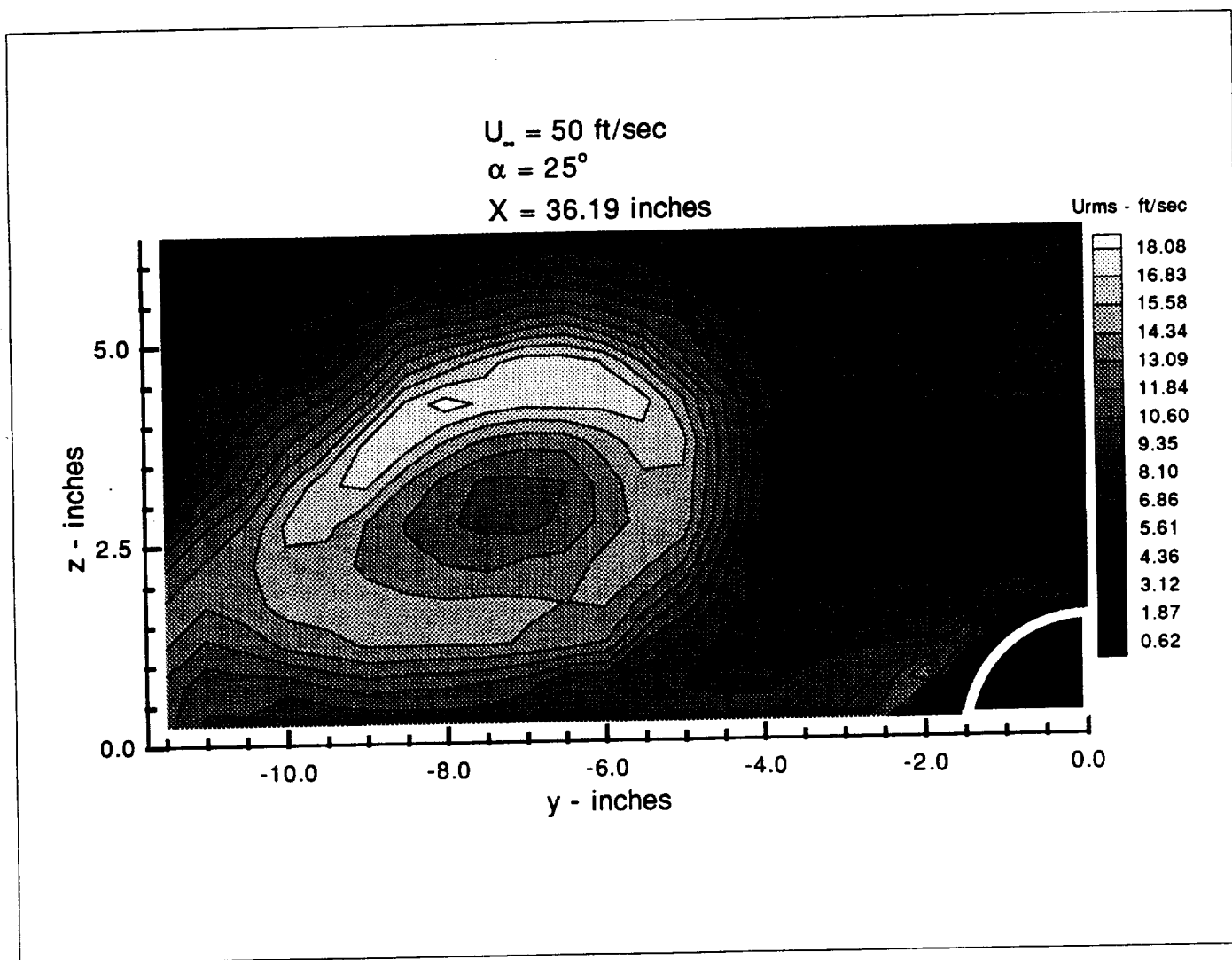
Fig.4.20a   RMS velocity contours (U-component) at LDV station 3
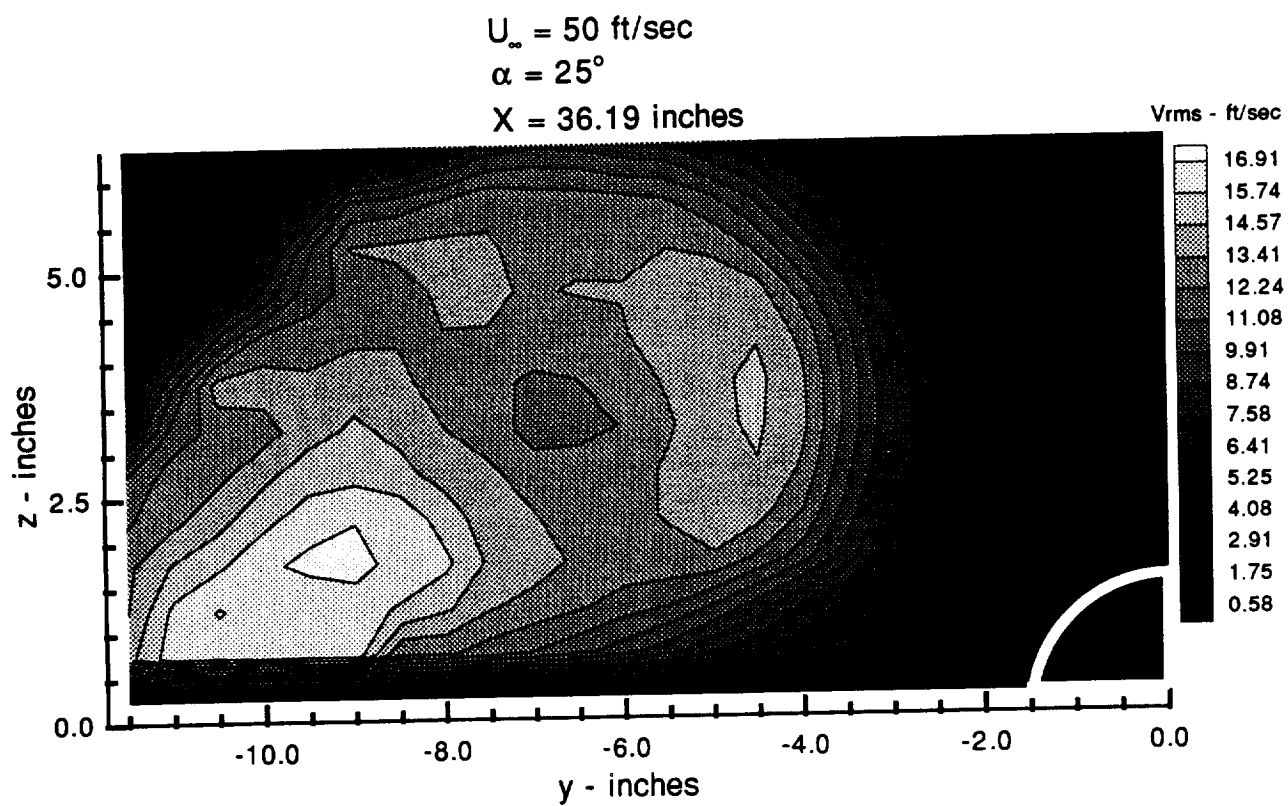
Fig.4.20b   RMS velocity contours (V-component) at LDV station 3
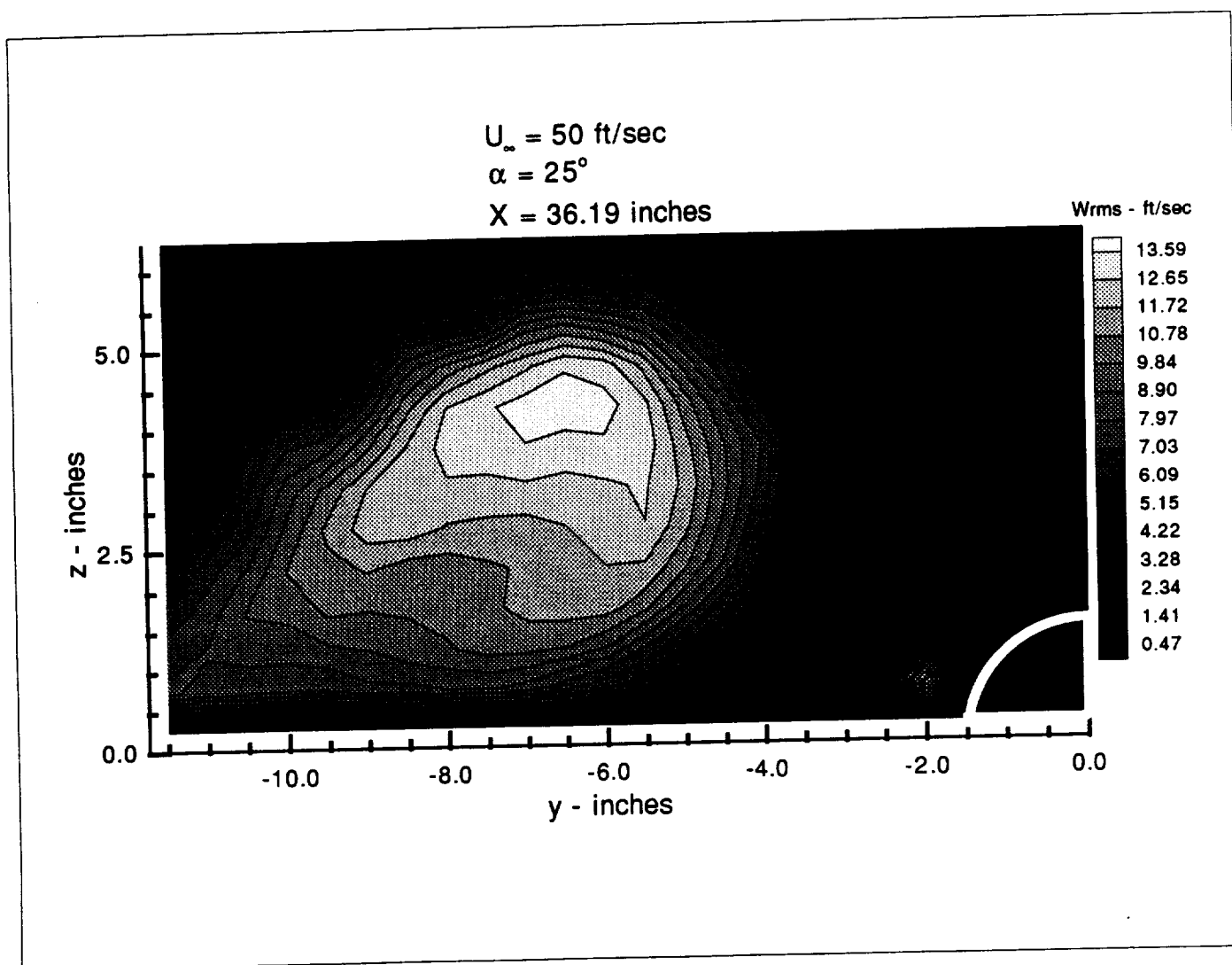
Fig.4.20c   RMS velocity contours (W-component) at LDV station 3
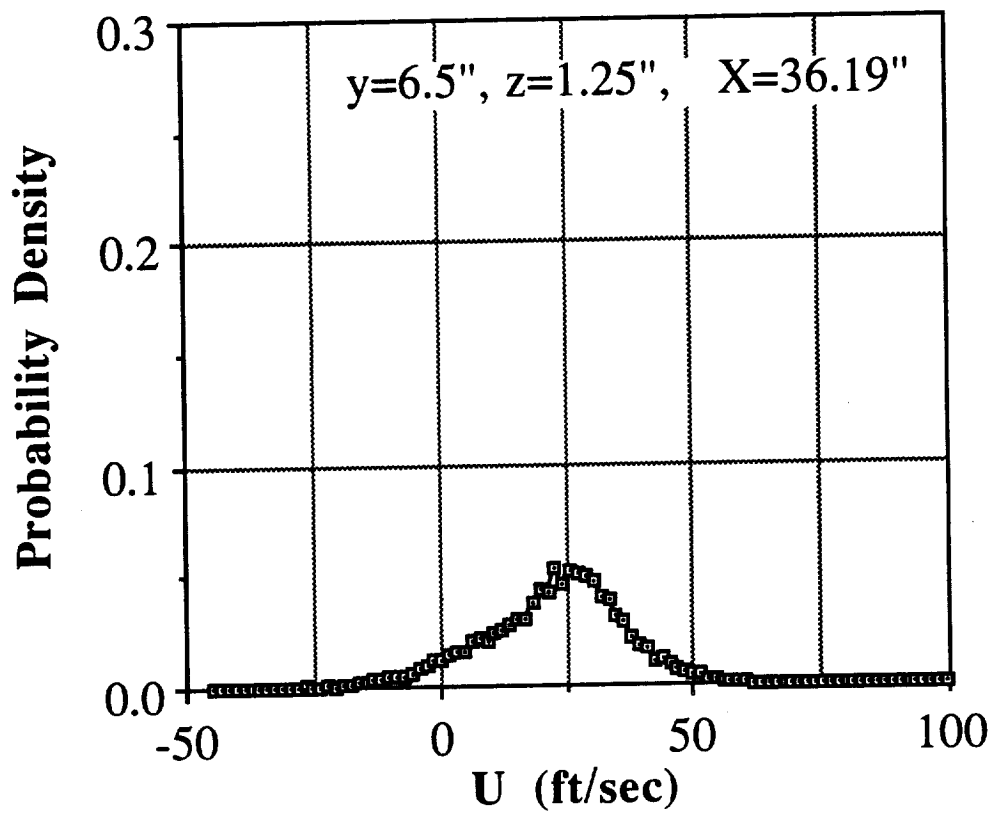
Fig.4.21a Histogram of U-component at y=6.5", z=1.25" at LDV station 3
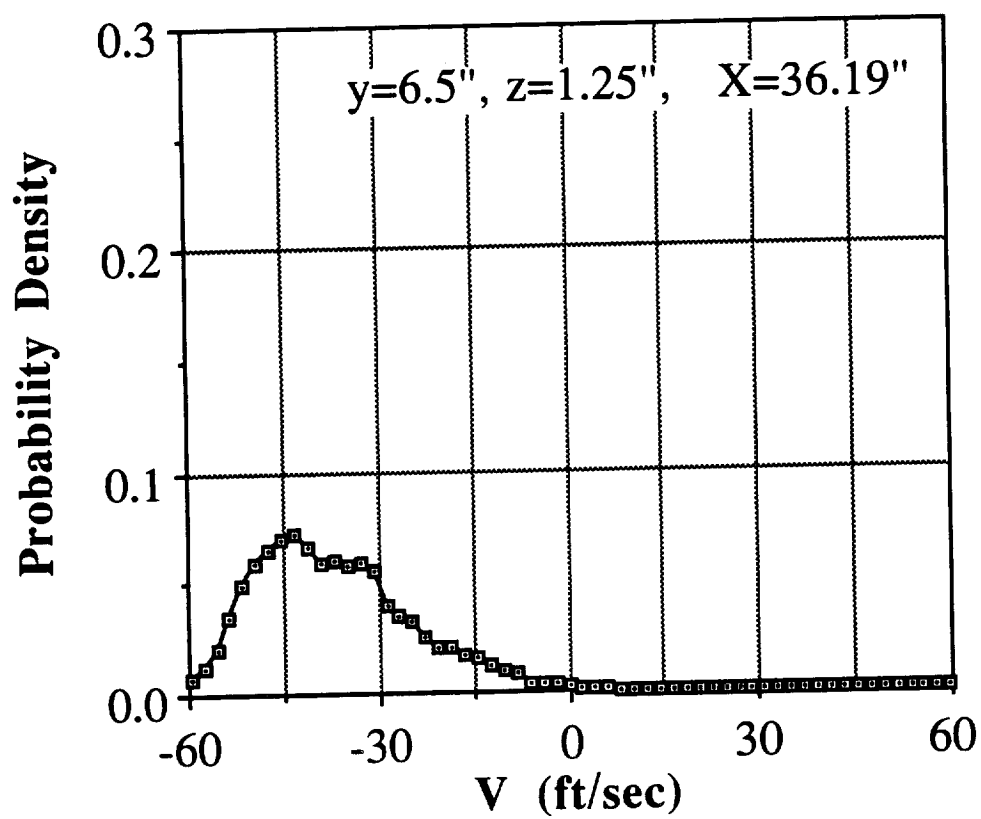
Fig.4.21b   Histogram of V-component at y=6.5", z=1.25" at LDV station 3
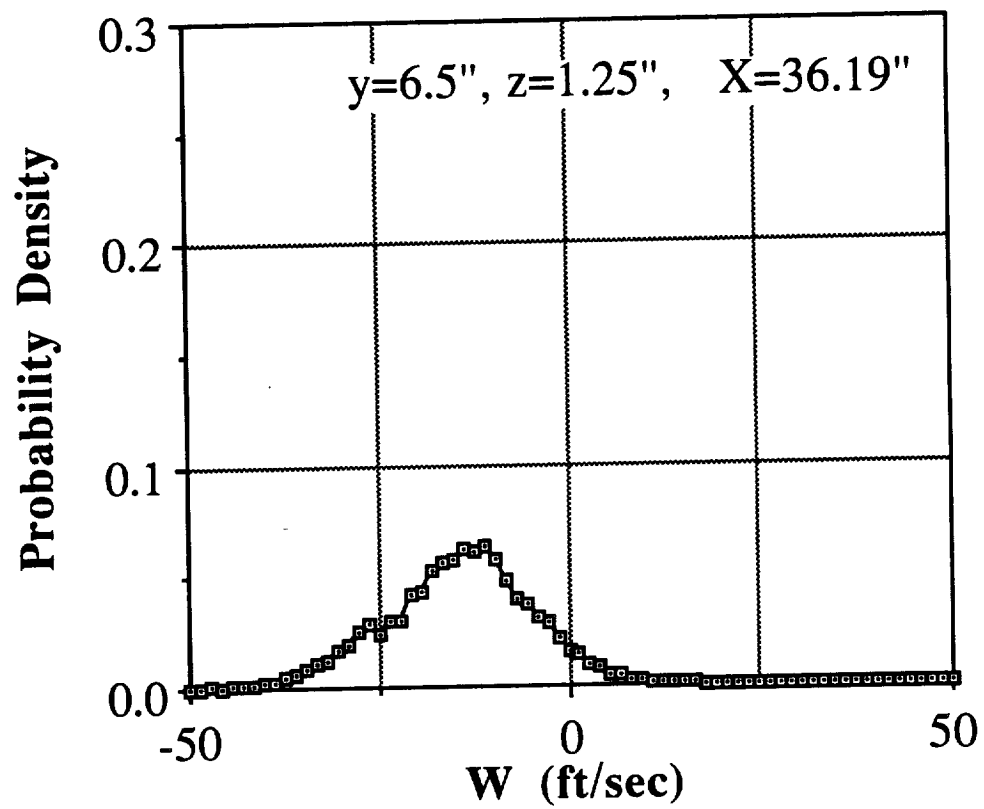
Fig.4.21c   Histogram of W-component at y=6.5", z=1.25" at LDV station 3
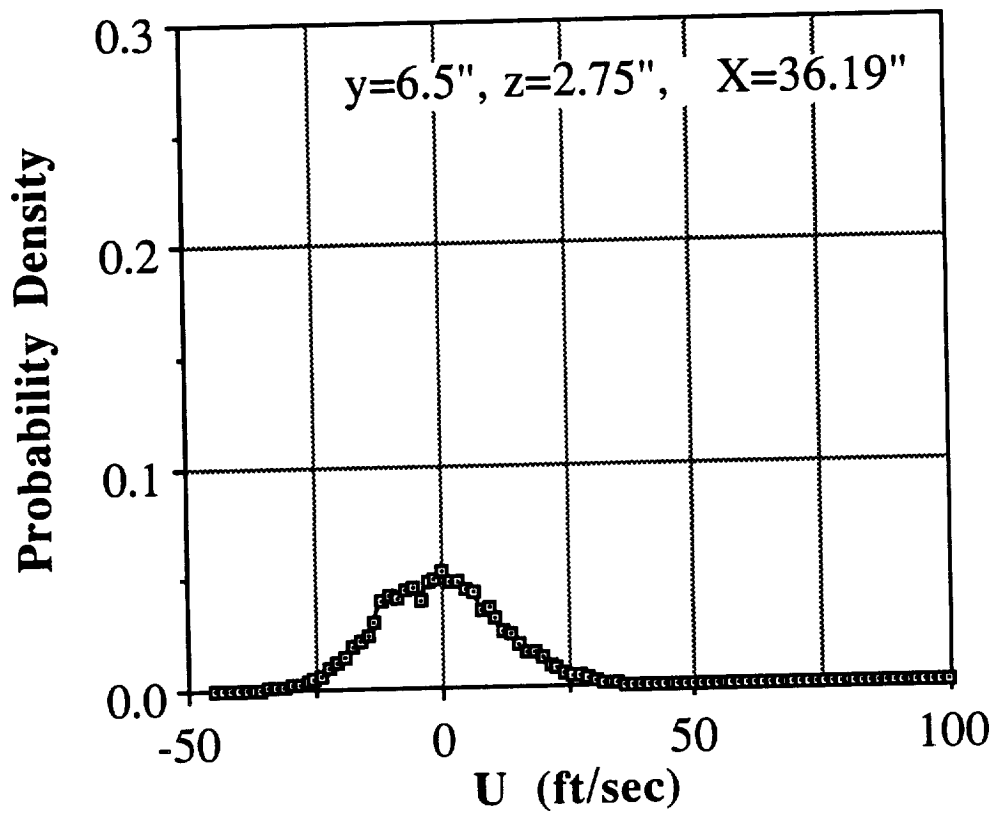
Fig.4.22a   Histogram of U-component at y=6.5", z=2.75" at LDV station 3
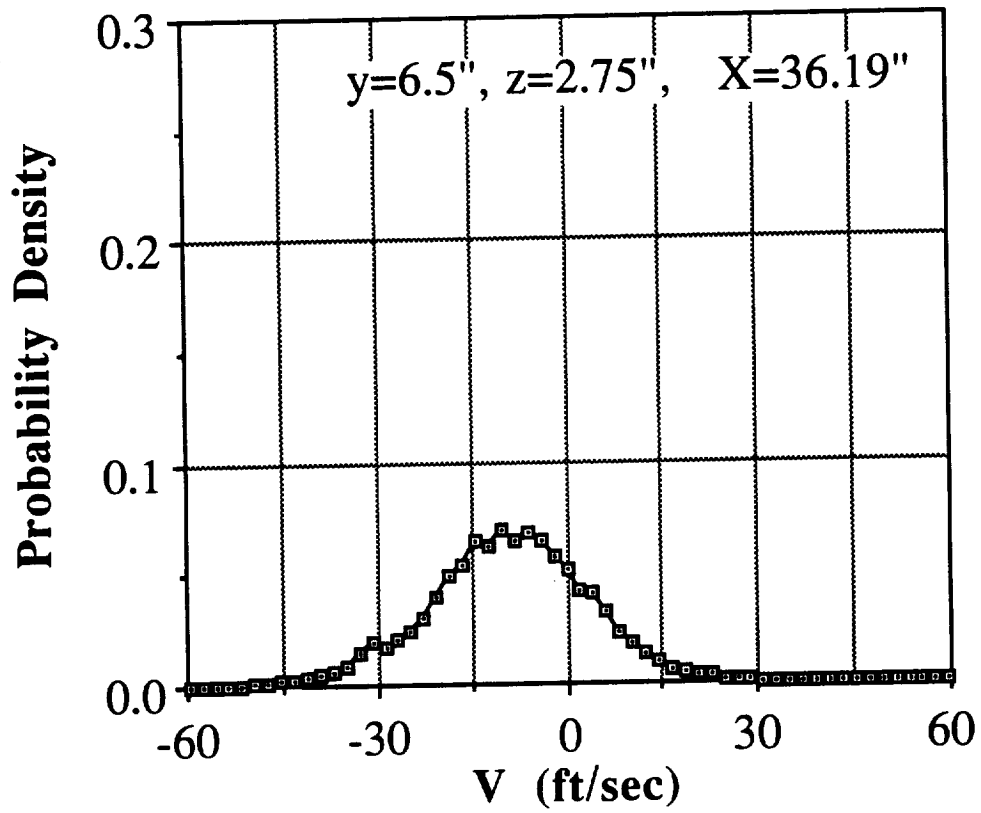
Fig.4.22b   Histogram of V-component at y=6.5", z=2.75" at LDV station 3
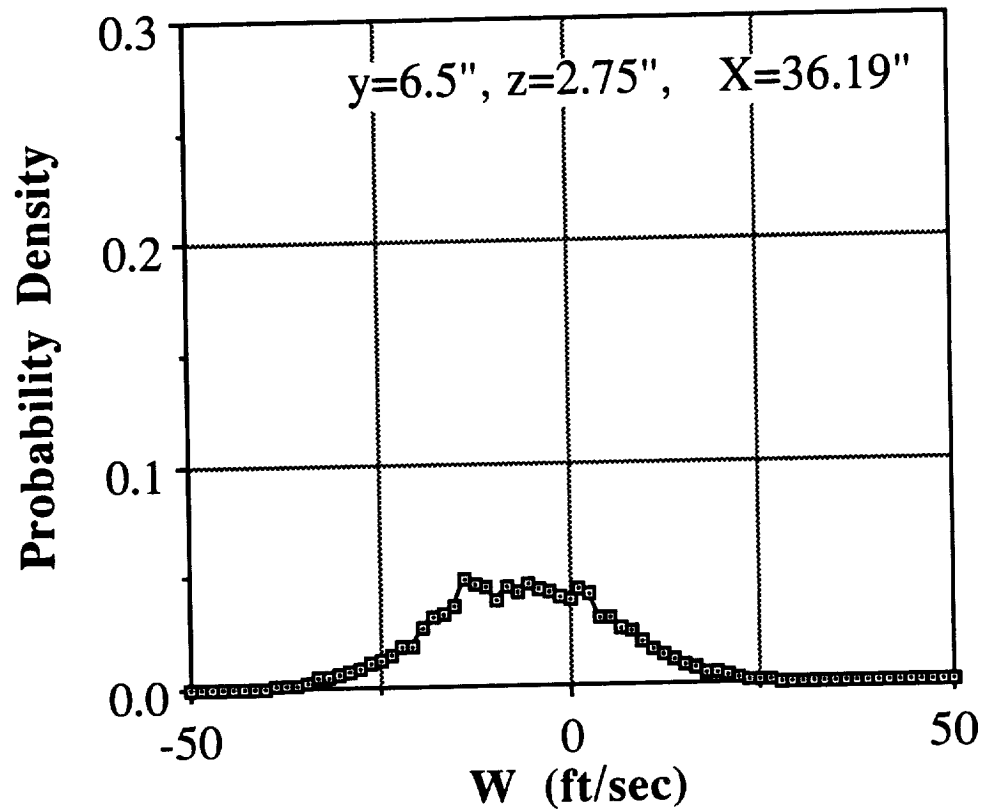
Fig.4.22c   Histogram of W-component at y=6.5", z=2.75" at LDV station 3
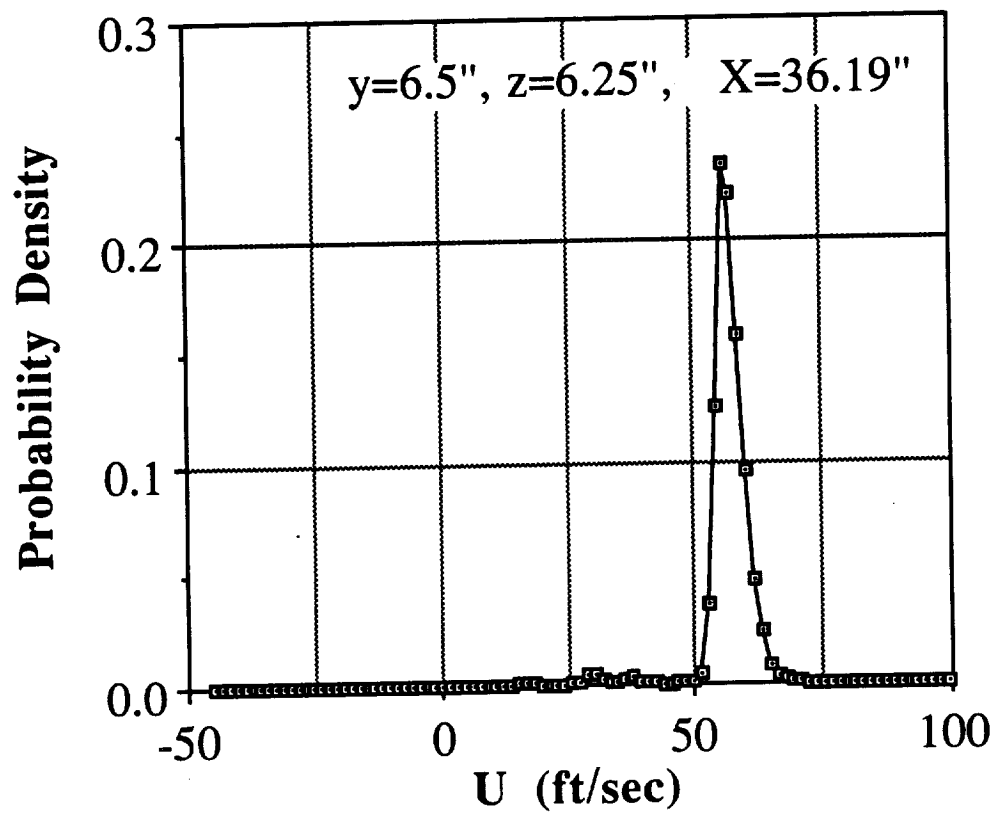
Fig.4.23a   Histogram of U-component at y=6.5", z=6.25" at LDV station 3
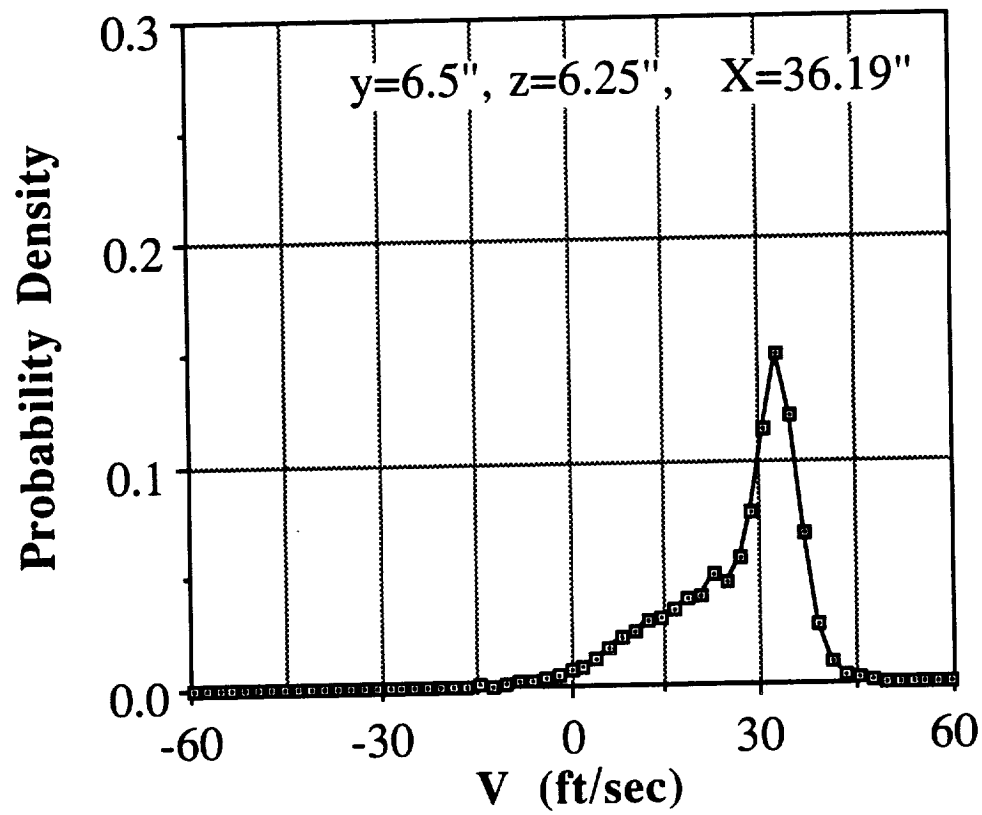
Fig.4.23b   Histogram of V-component at y=6.5", z=6.25" at LDV station 3
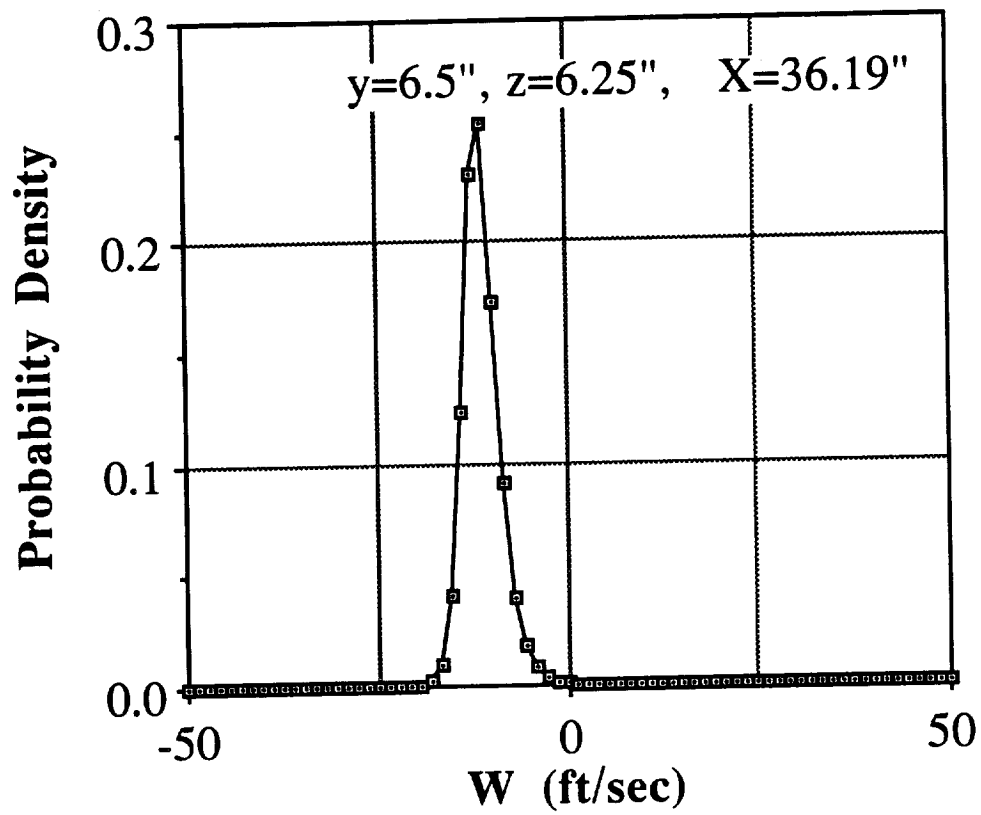
Fig.4.23c   Histogram of W-component at y=6.5", z=6.25" at LDV station 3

Top View
of Left Wing

Station 1 (19.8% of b/2)
Station 2 (28.7% of b/2)
Station 3 (37.5% of b/2)
Station 4 (48.5% of b/2)
Station 5 (61.8% of b/2)
Station 6 (79.5% of b/2)
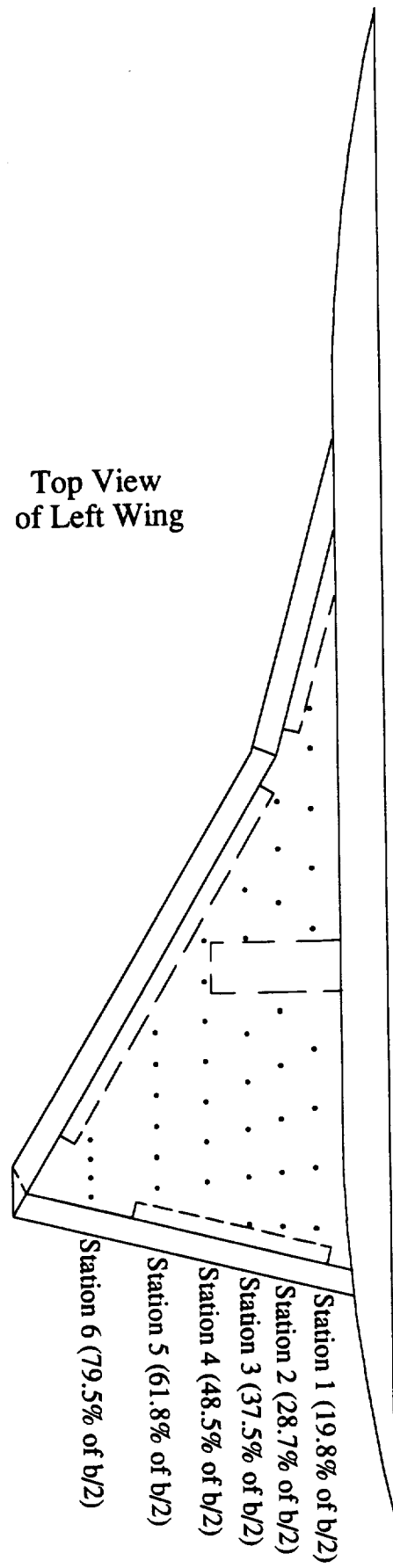
Fig.4.24   Static pressure measuring locations on the generic wing/body model
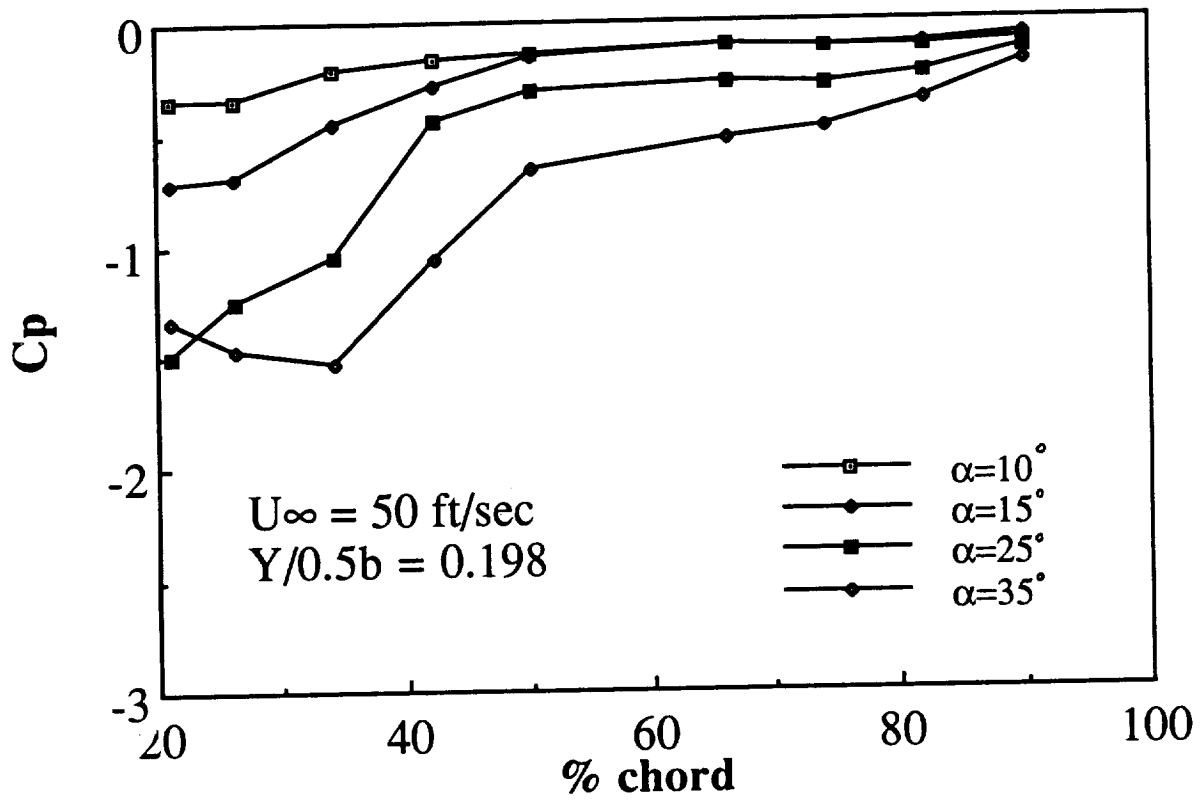
Fig.4.25a   Cp distribution at spanwise station 1 under different model angles
of attack, U∞=50 ft/sec
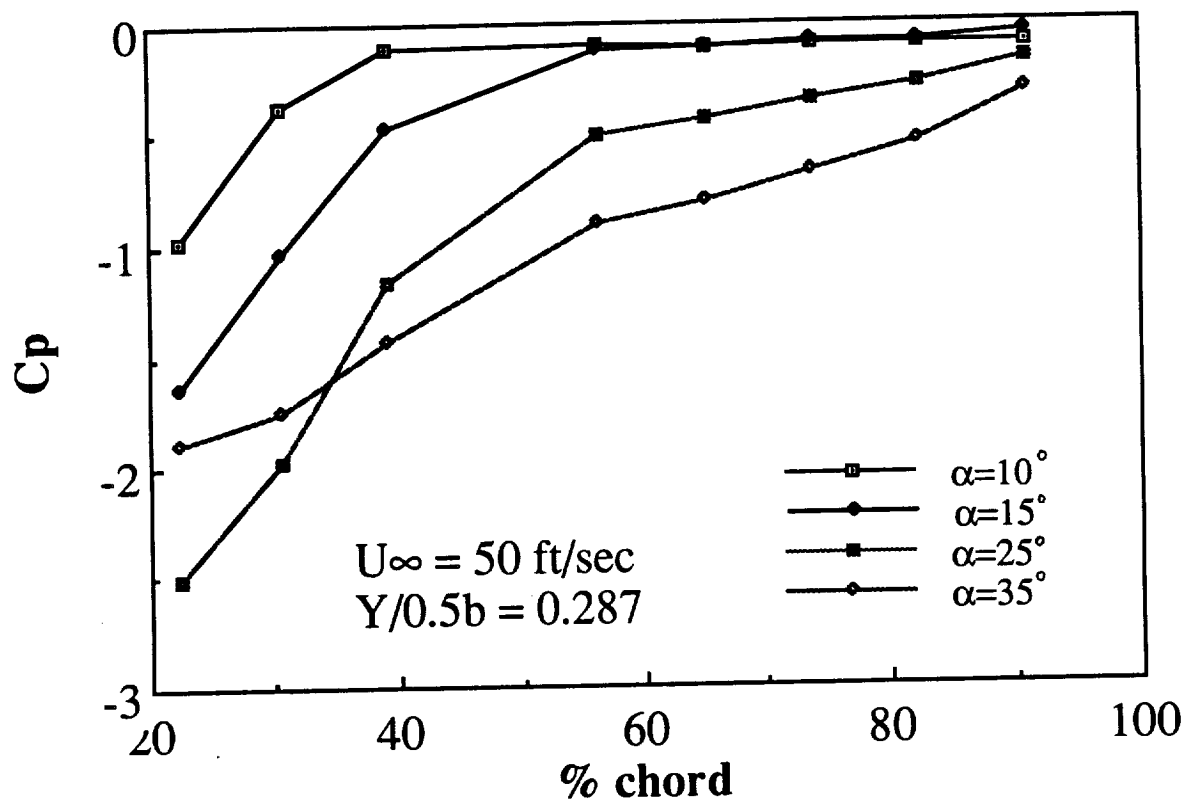
Fig.4.25b   Cp distribution at spanwise station 2 under different model angles
of attack, U∞=50 ft/sec
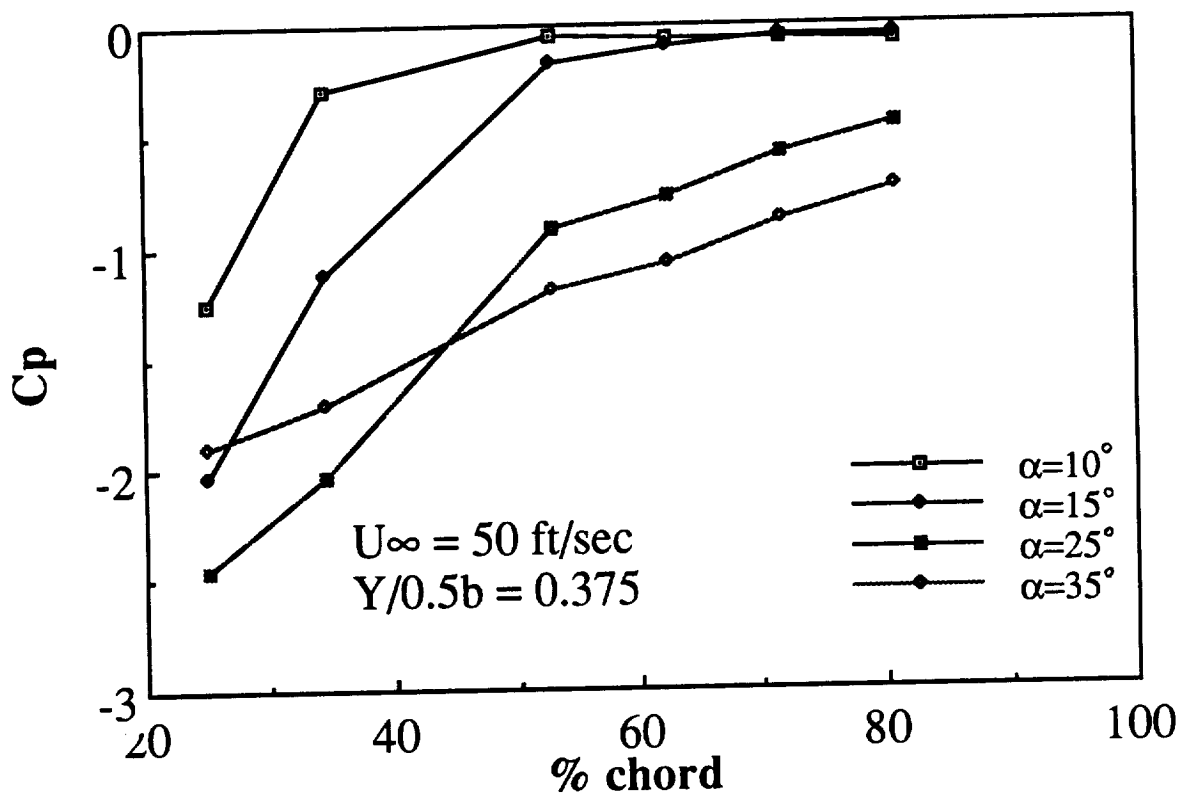
Fig.4.25c   Cp distribution at spanwise station 3 under different model angles of attack, U∞=50 ft/sec
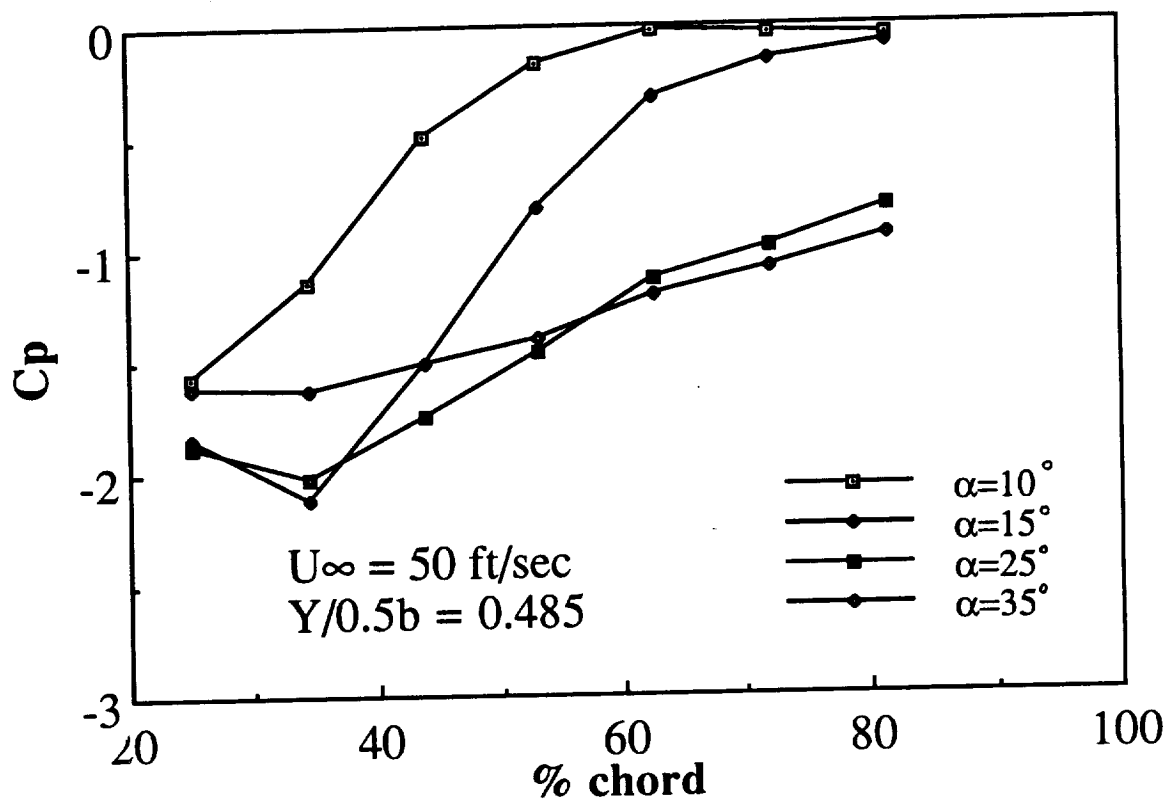
Fig.4.25d   Cp distribution at spanwise station 4 under different model angles
of attack, U∞=50 ft/sec
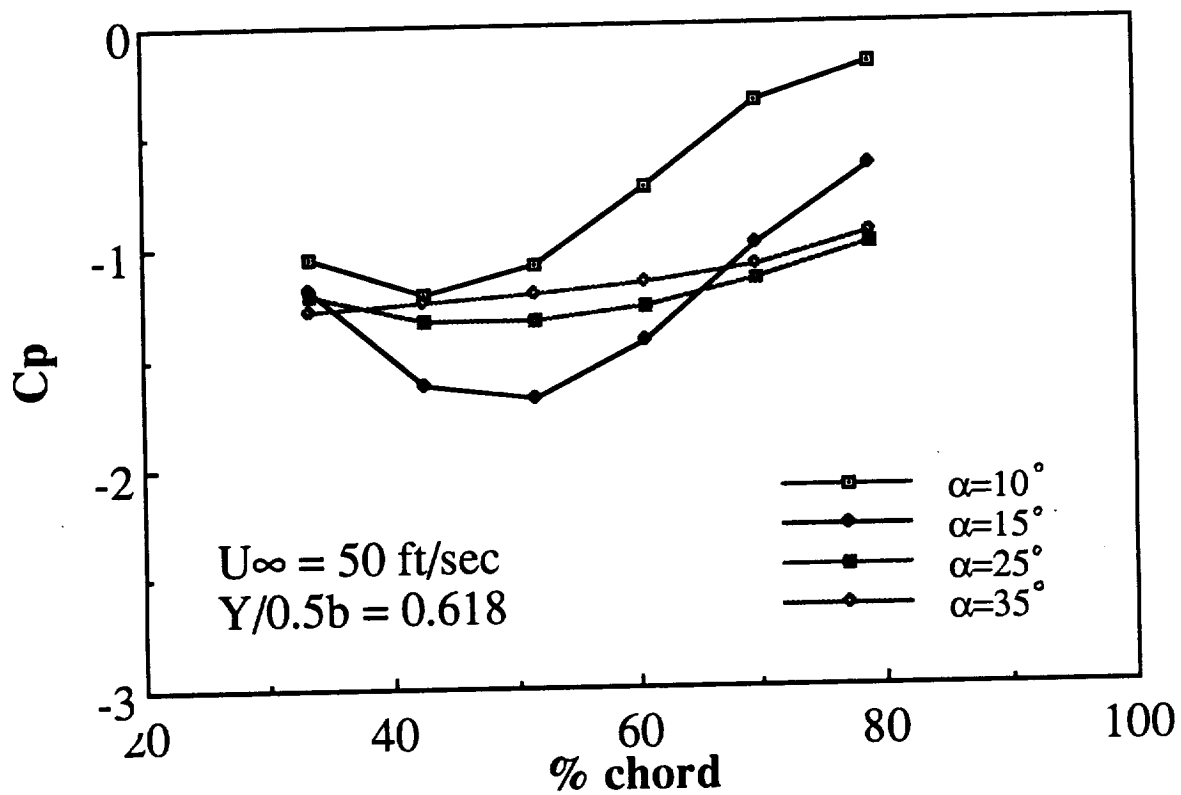
Fig.4.25e   Cp distribution at spanwise station 5 under different model angles
of attack, U_∞=50 ft/sec
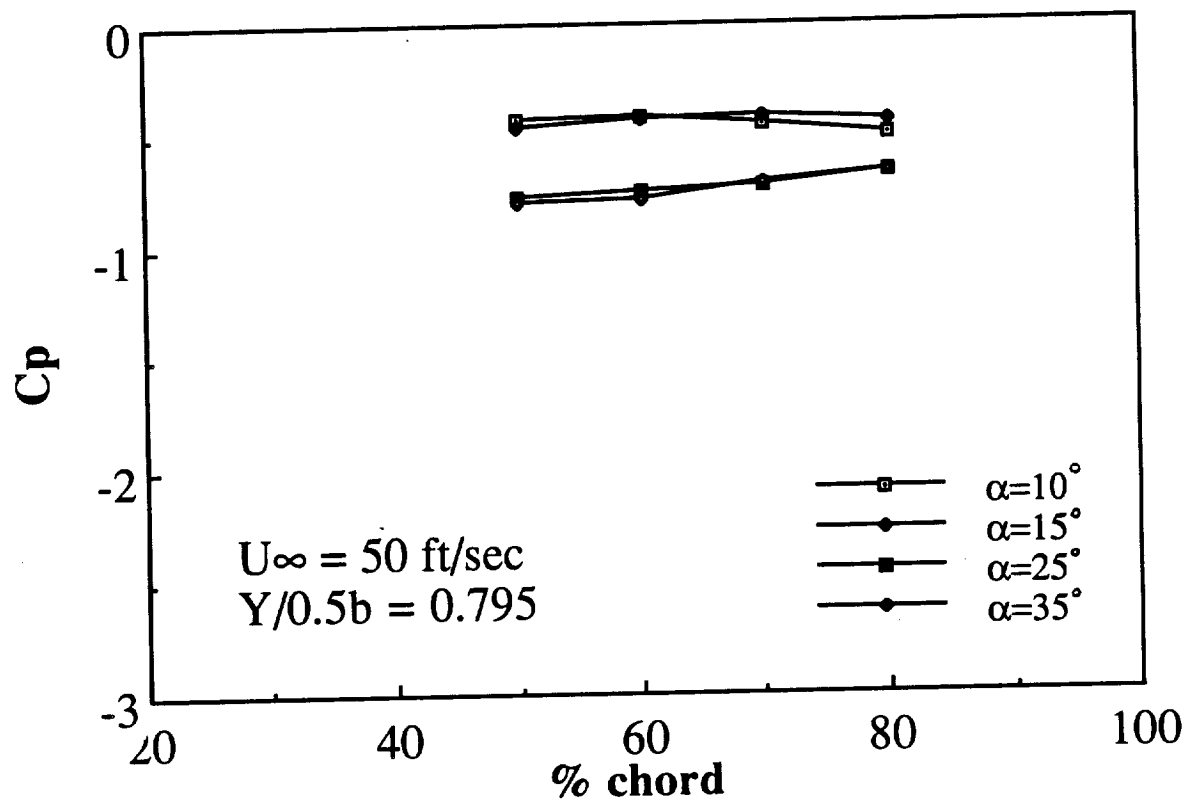
Fig.4.25f   Cp distribution at spanwise station 6 under different model angles of attack, U∞=50 ft/sec
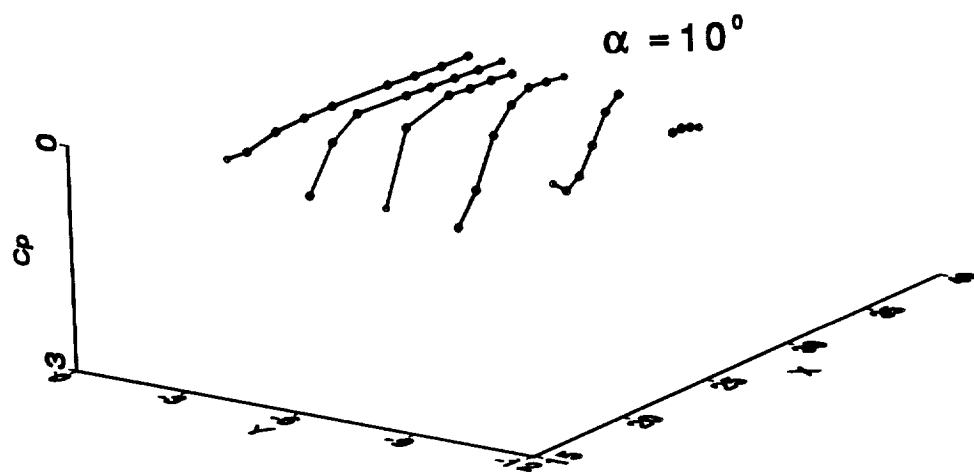
Fig.4.26a   Cp distribution over the left half wing at $\alpha=10^0$
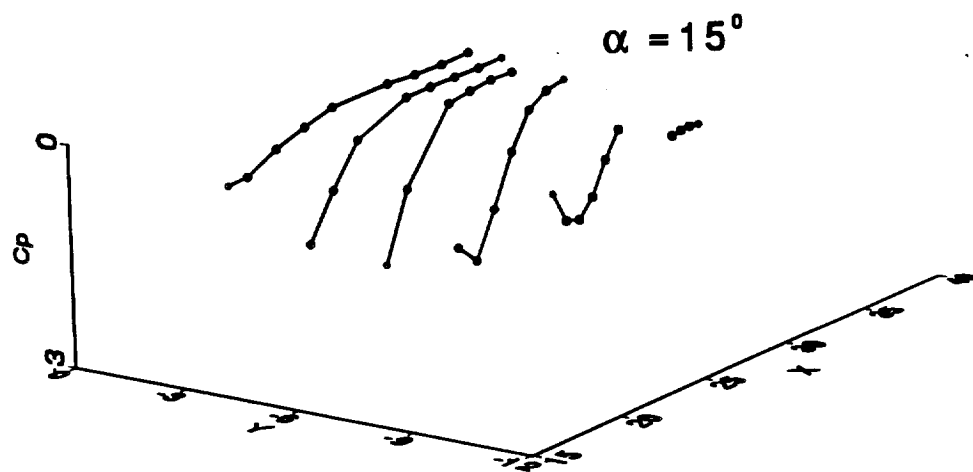
Fig.4.26b   Cp distribution over the left half wing at $\alpha=15^O$
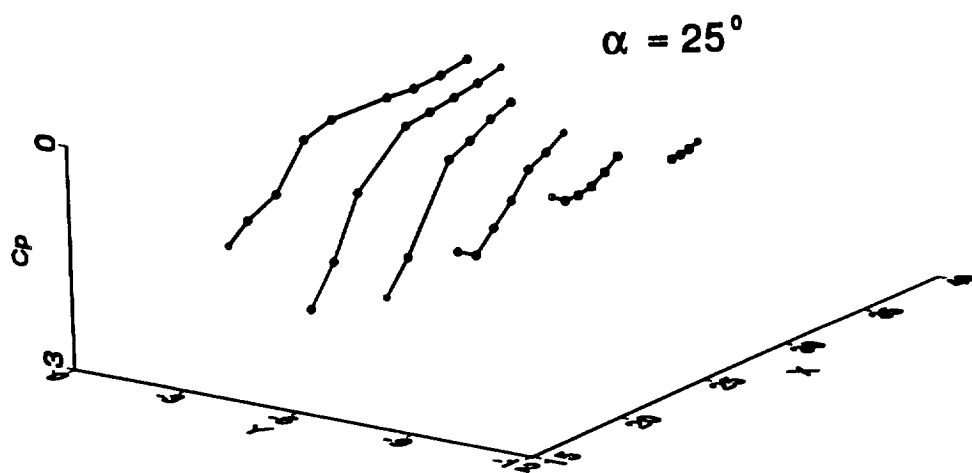
Fig.4.26c   Cp distribution over the left half wing at α=25$^{\text{o}}$
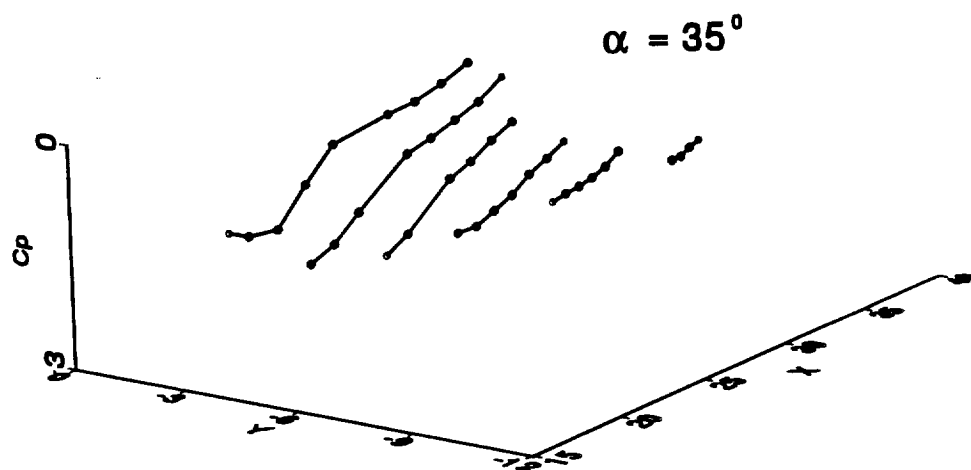
Fig.4.26d   Cp distribution over the left half wing at α=35°
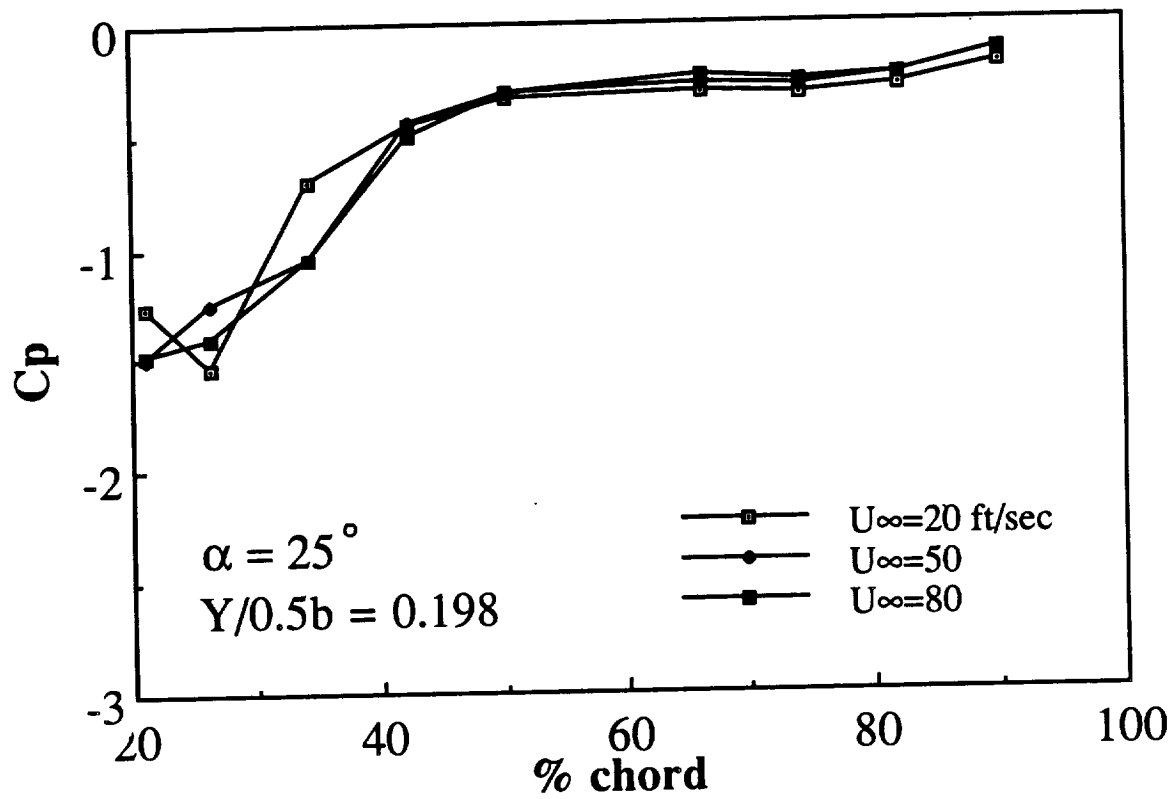
Fig.4.27a   Cp distribution at spanwise station 1 under different freestream
speeds, α=25°
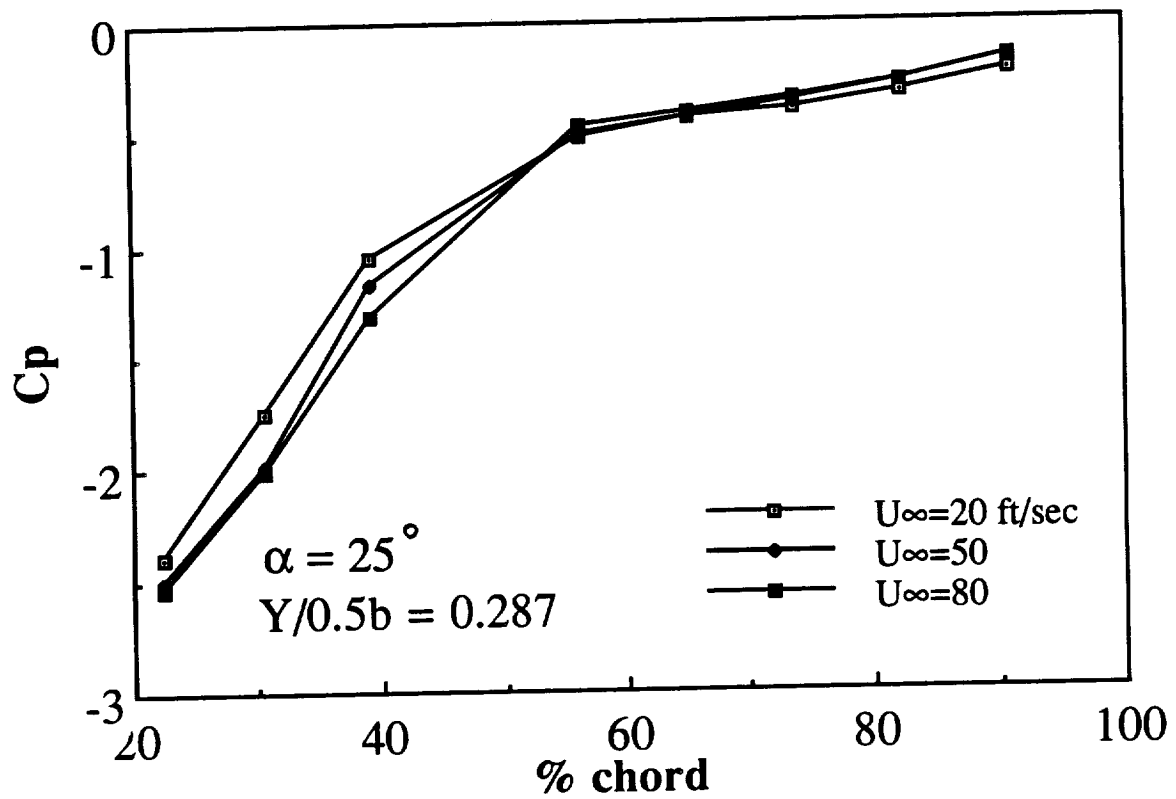
Fig.4.27b   Cp distribution at spanwise station 2 under different freestream speeds, α=25°
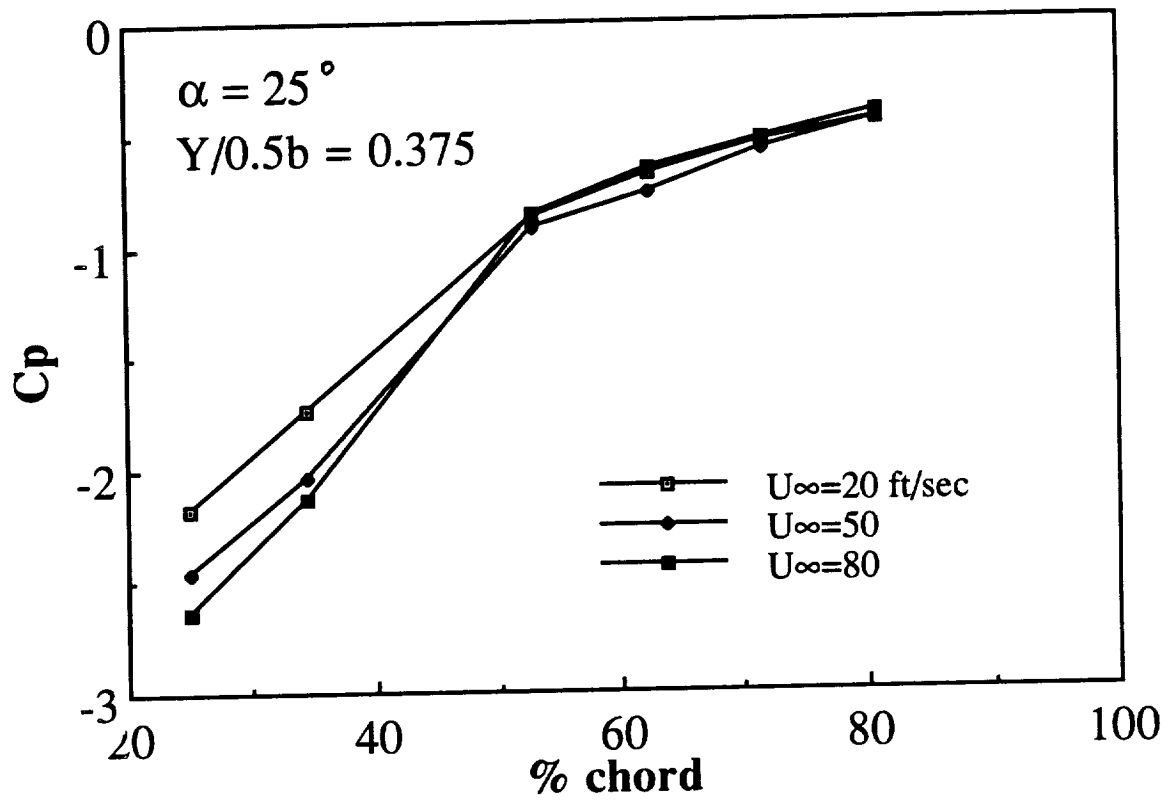
Fig.4.27c   Cp distribution at spanwise station 3 under different freestream speeds, $\alpha=25^{\circ}$
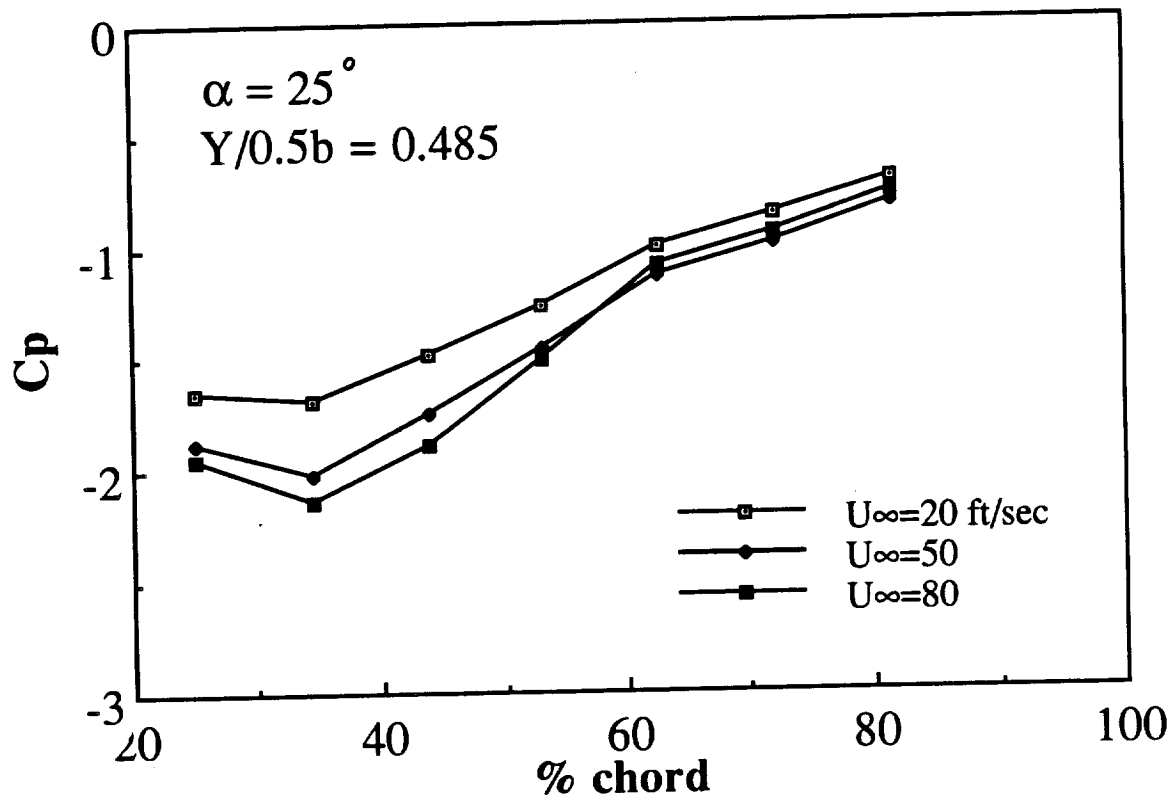
Fig.4.27d   Cp distribution at spanwise station 4 under different freestream speeds, α=25°

C-2
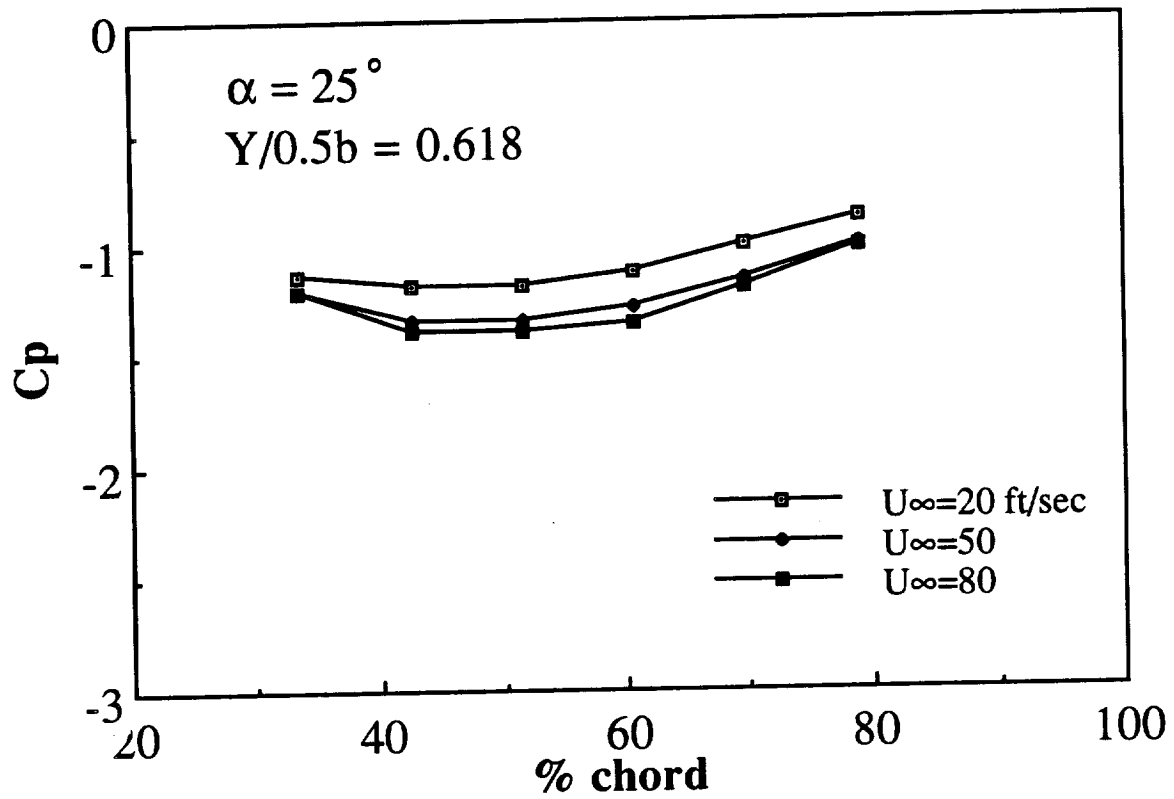
Fig.4.27e Cp distribution at spanwise station 5 under different freestream speeds, α=25°
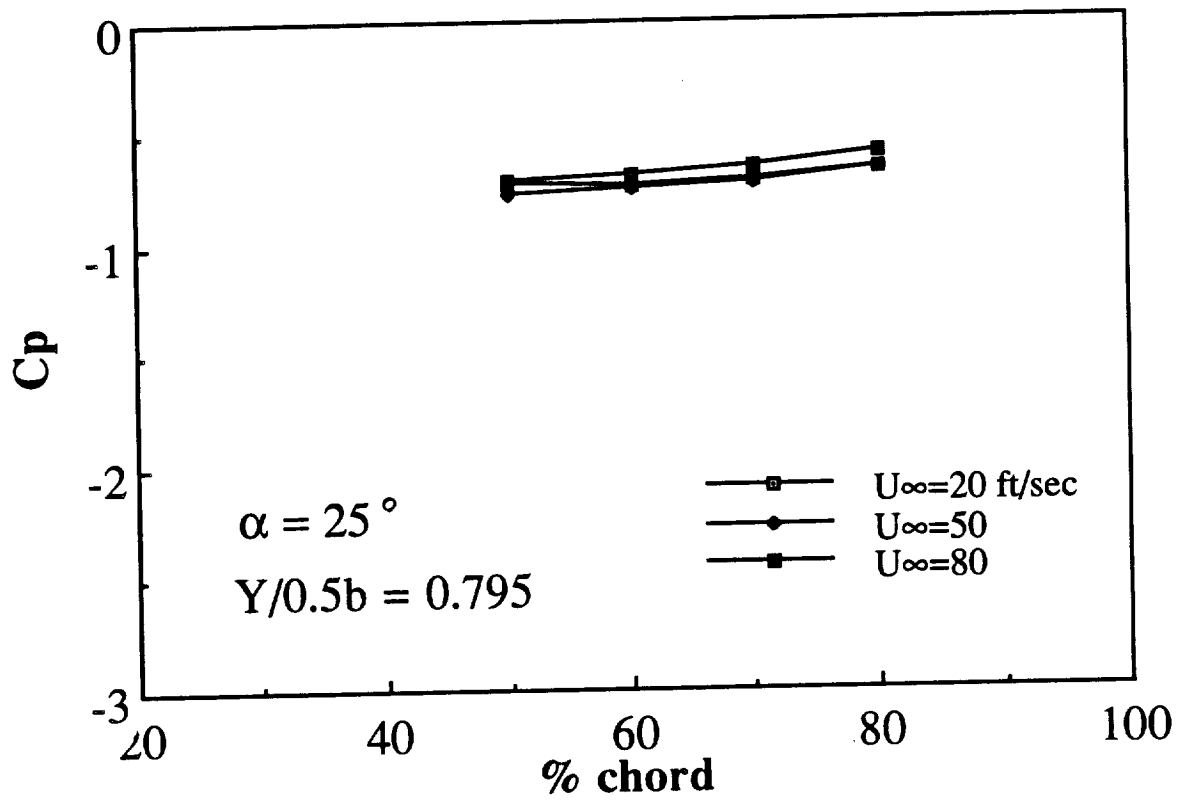
Fig.4.27f   Cp distribution at spanwise station 6 under different freestream
speeds, α=25°

Top View
of Left Wing

.4

·6

·3

5
·

1 2
·
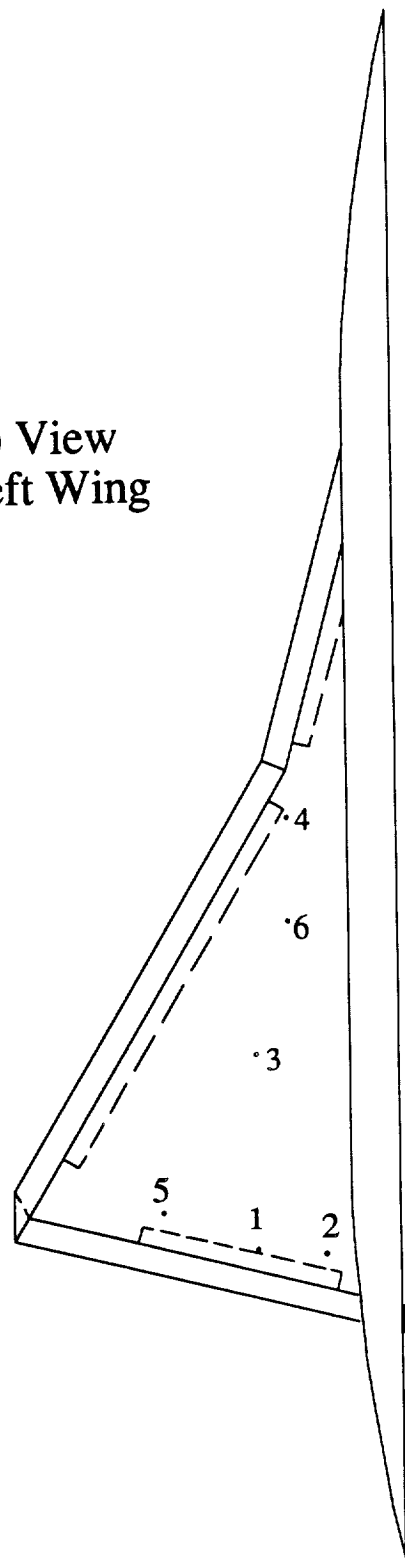
Fig.4.28   Hot-wire measurement locations above the model
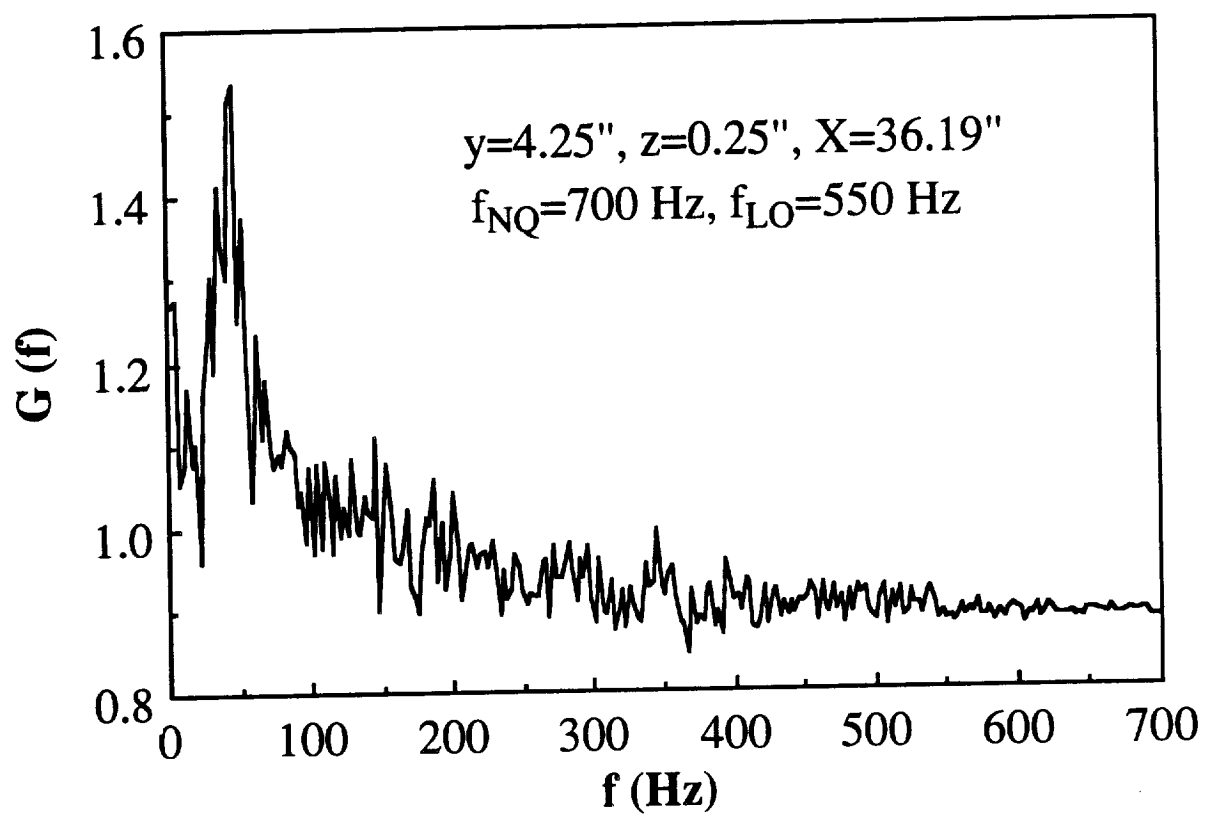
Fig.4.29a   Velocity spectrum measured at HW station 1, z=0.25", U∞=50 ft/sec, α=25°
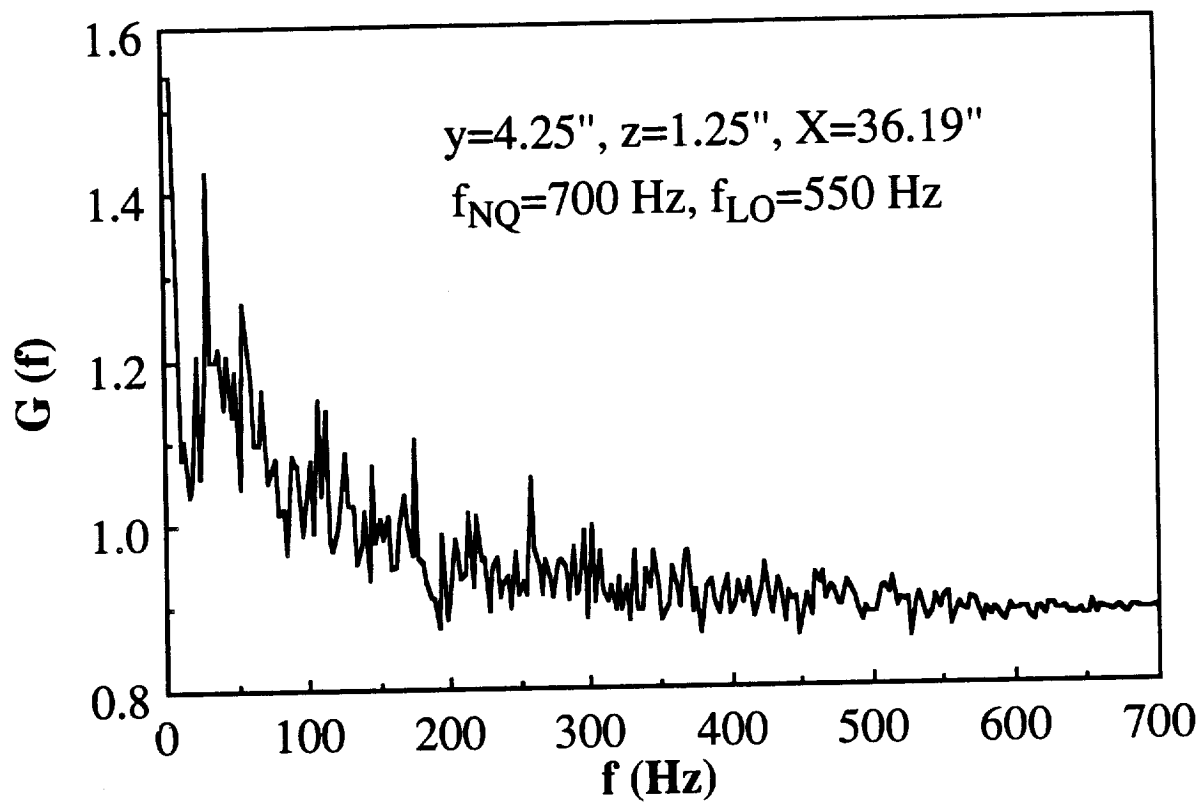
Fig.4.29b   Velocity spectrum measured at HW station 1, z=1.25", U∞=50 ft/sec, α=25°
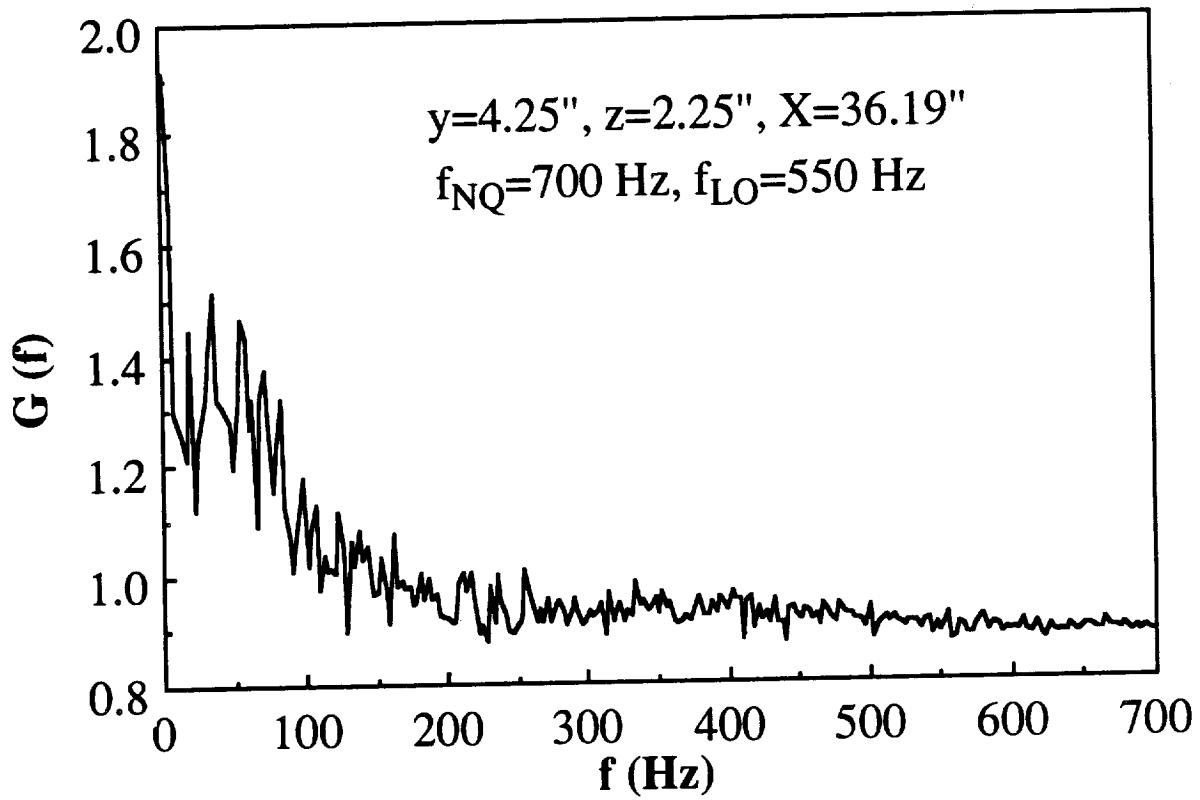
Fig.4.29c   Velocity spectrum measured at HW station 1, z=2.25", U∞=50 ft/sec,
α=25°
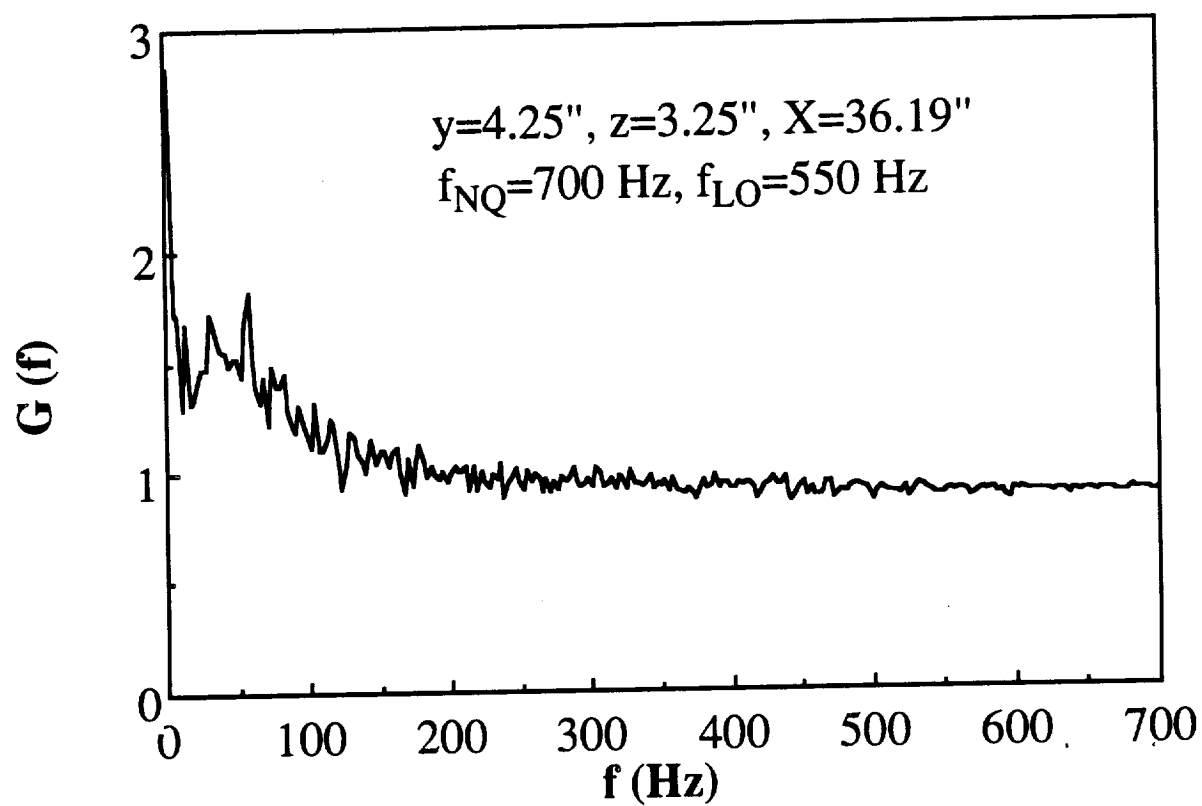
Fig.4.29d   Velocity spectrum measured at HW station 1, z=3.25", U∞=50 ft/sec, α=25°
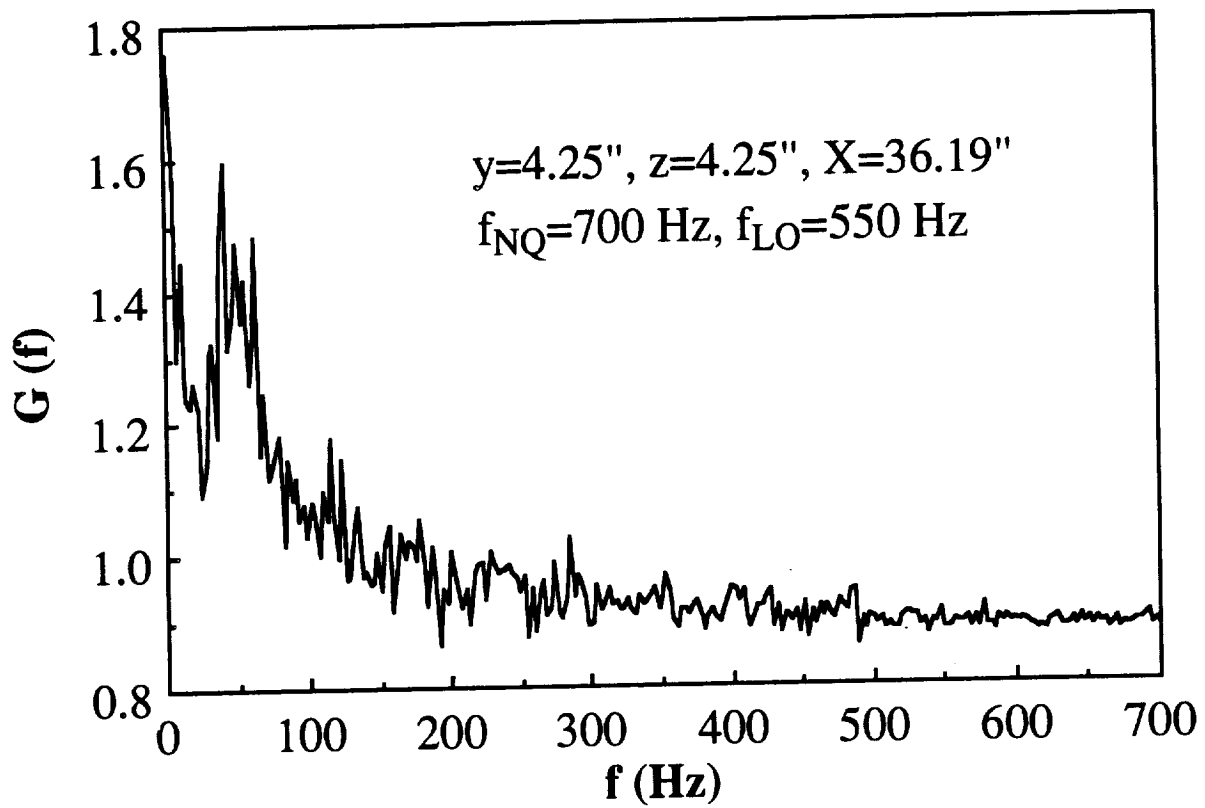
Fig.4.29e Velocity spectrum measured at HW station 1, z=4.25", U∞=50 ft/sec, α=25°
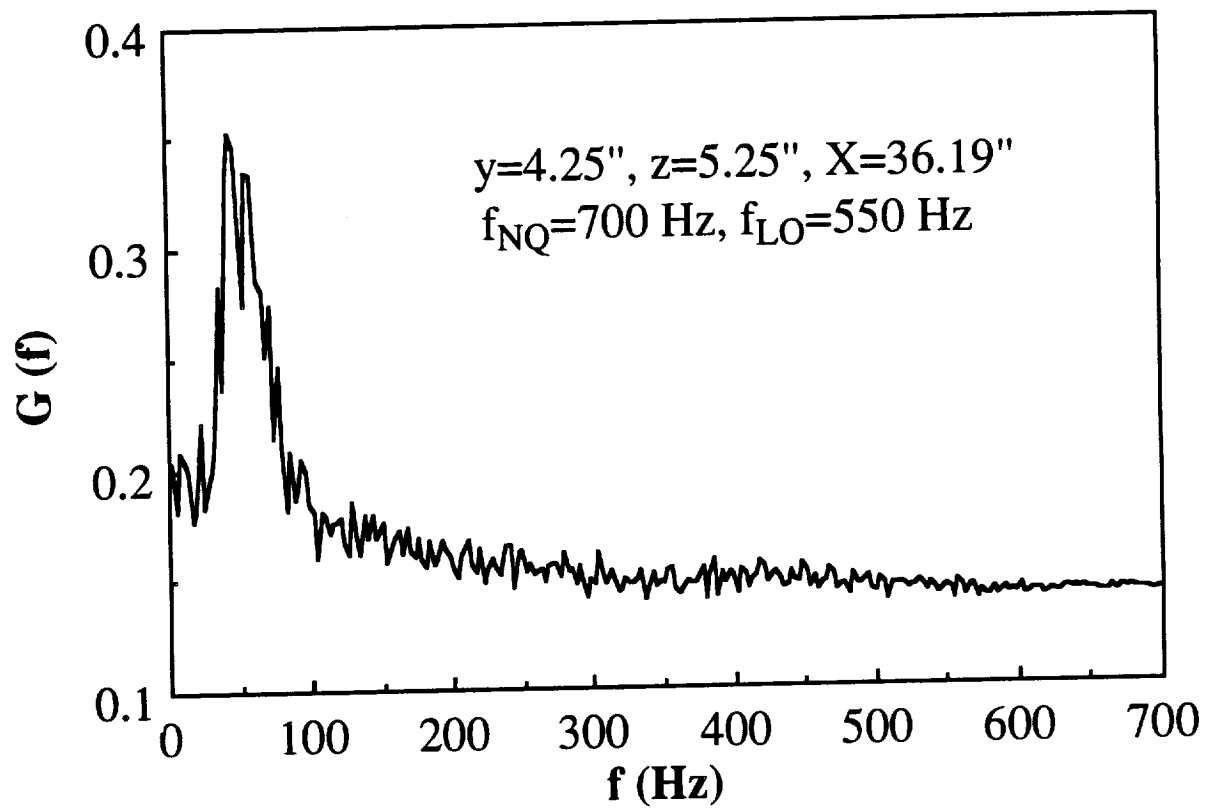
Fig.4.29f   Velocity spectrum measured at HW station 1, z=5.25", U_∞=50 ft/sec,
α=25°
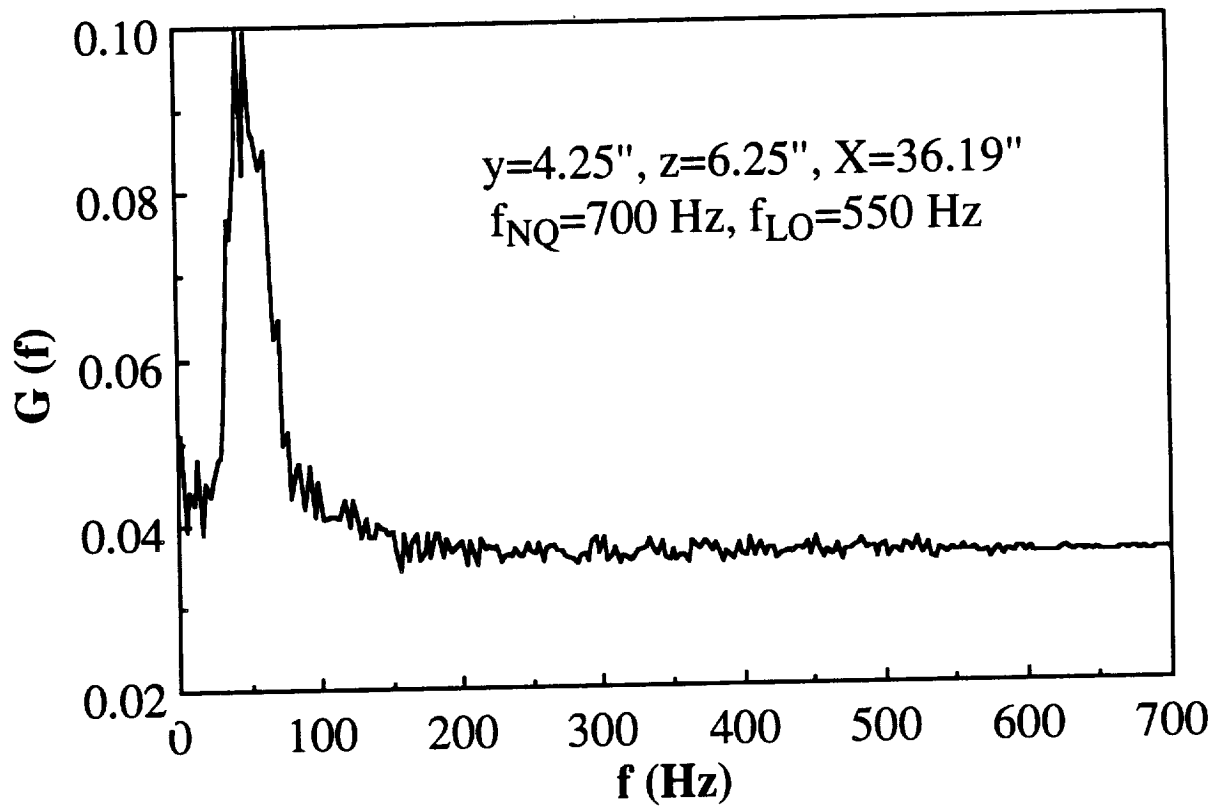
Fig.4.29g   Velocity spectrum measured at HW station 1, z=6.25", U_∞=50 ft/sec, α=25°
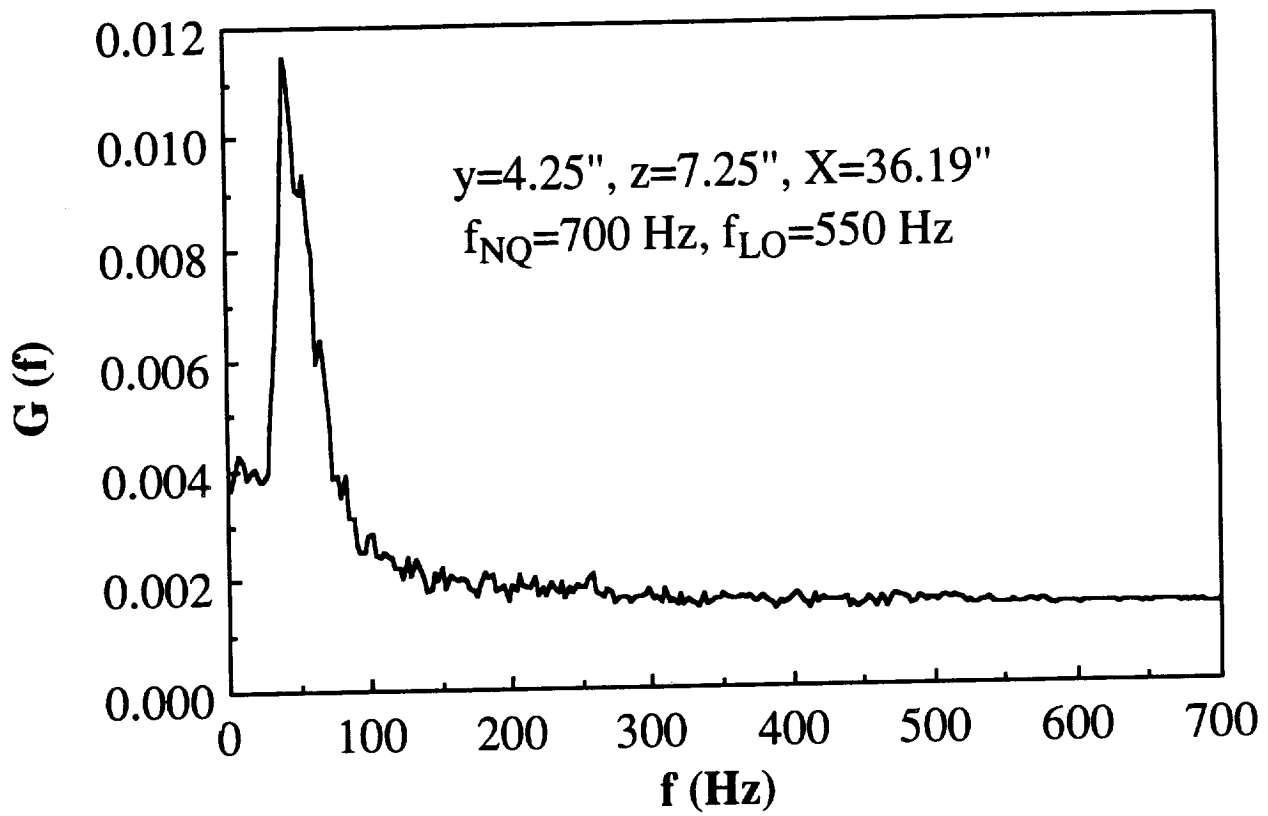
Fig.4.29h   Velocity spectrum measured at HW station 1, z=7.25", U∞=50 ft/sec, α=25°
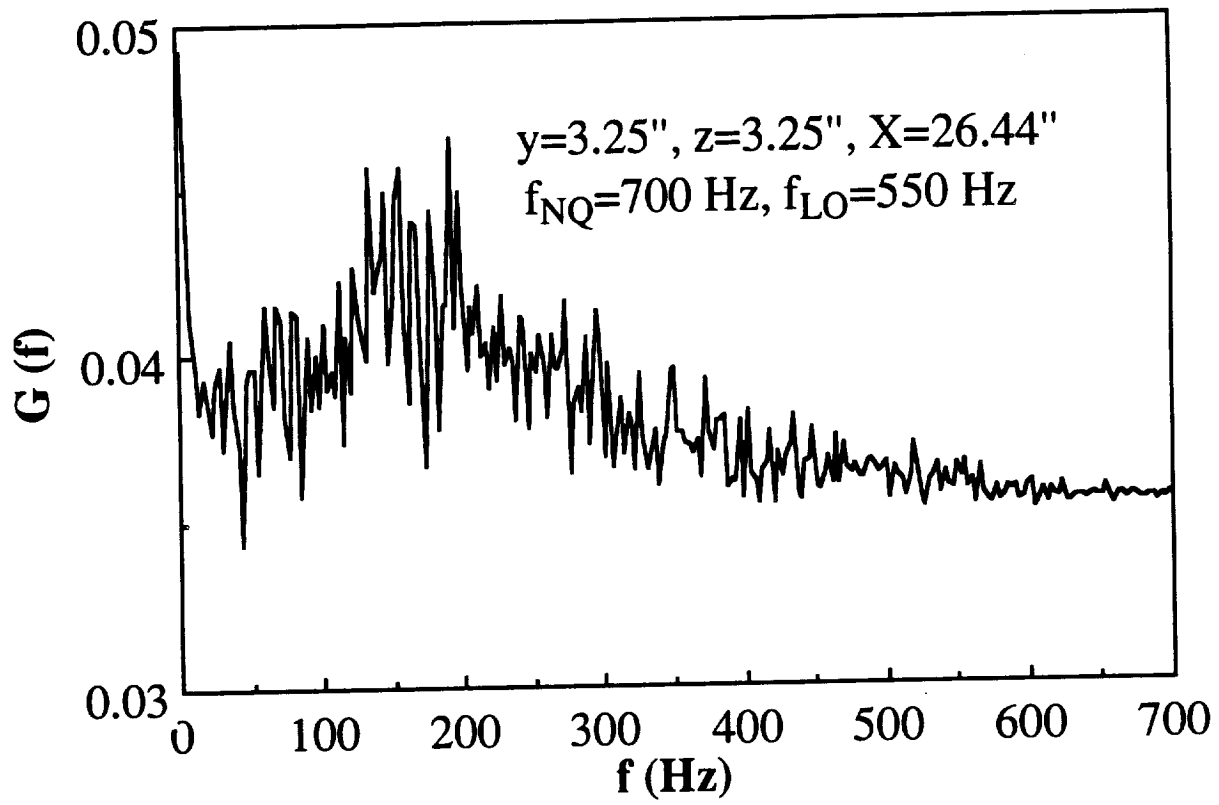
Fig.4.30 Velocity spectrum measured at HW station 6, z=3.25", U_∞=50 ft/sec, α=25°
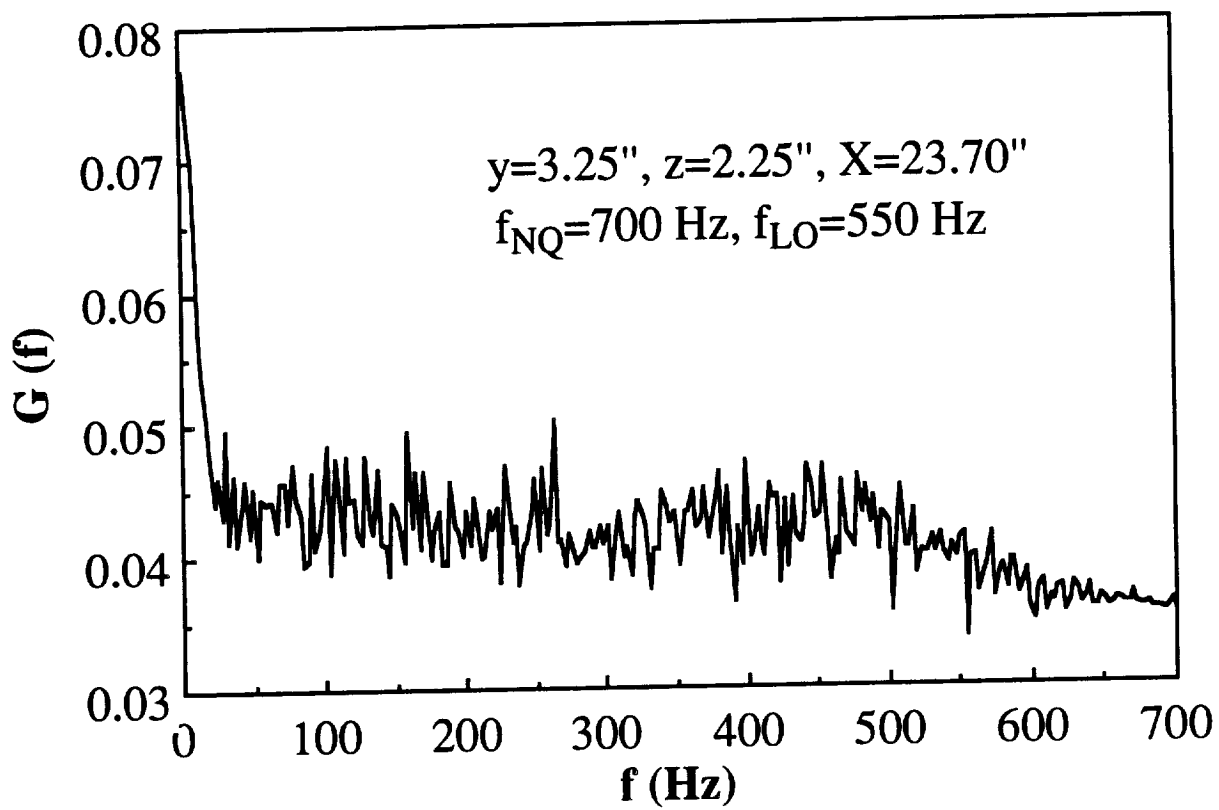
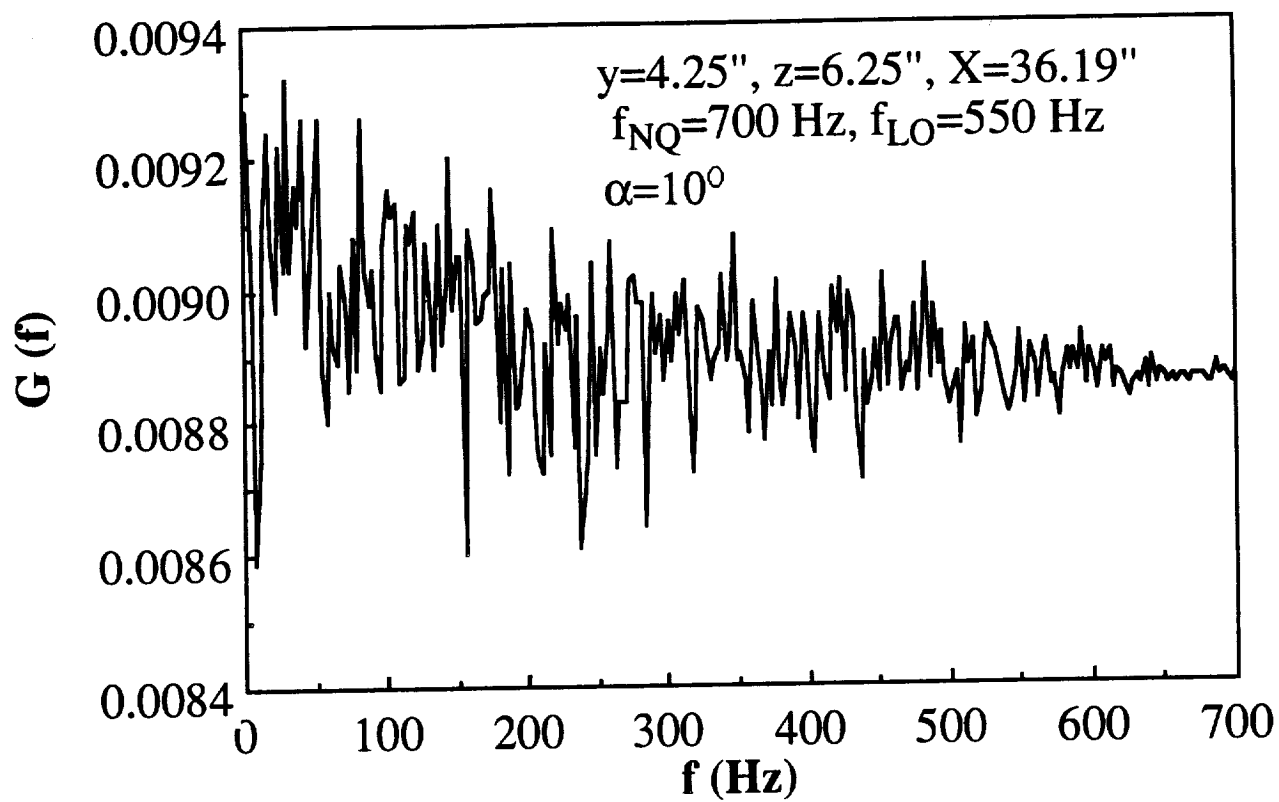Fig.4.31   Velocity spectrum measured at HW station 4, z=2.25", U∞=50 ft/sec, α=25°
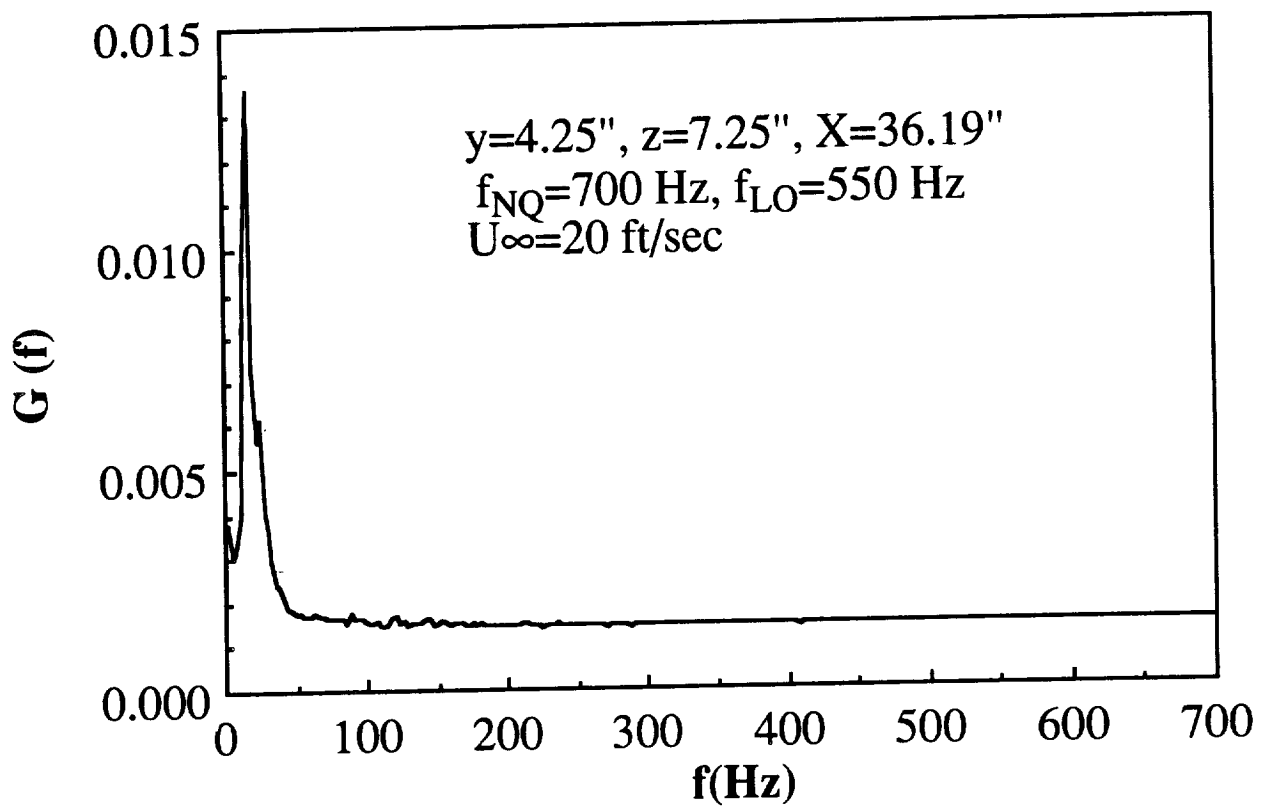
Fig.4.32a   Velocity spectrum measured at HW station 1, z=7.25", U∞=20 ft/sec, α=25°
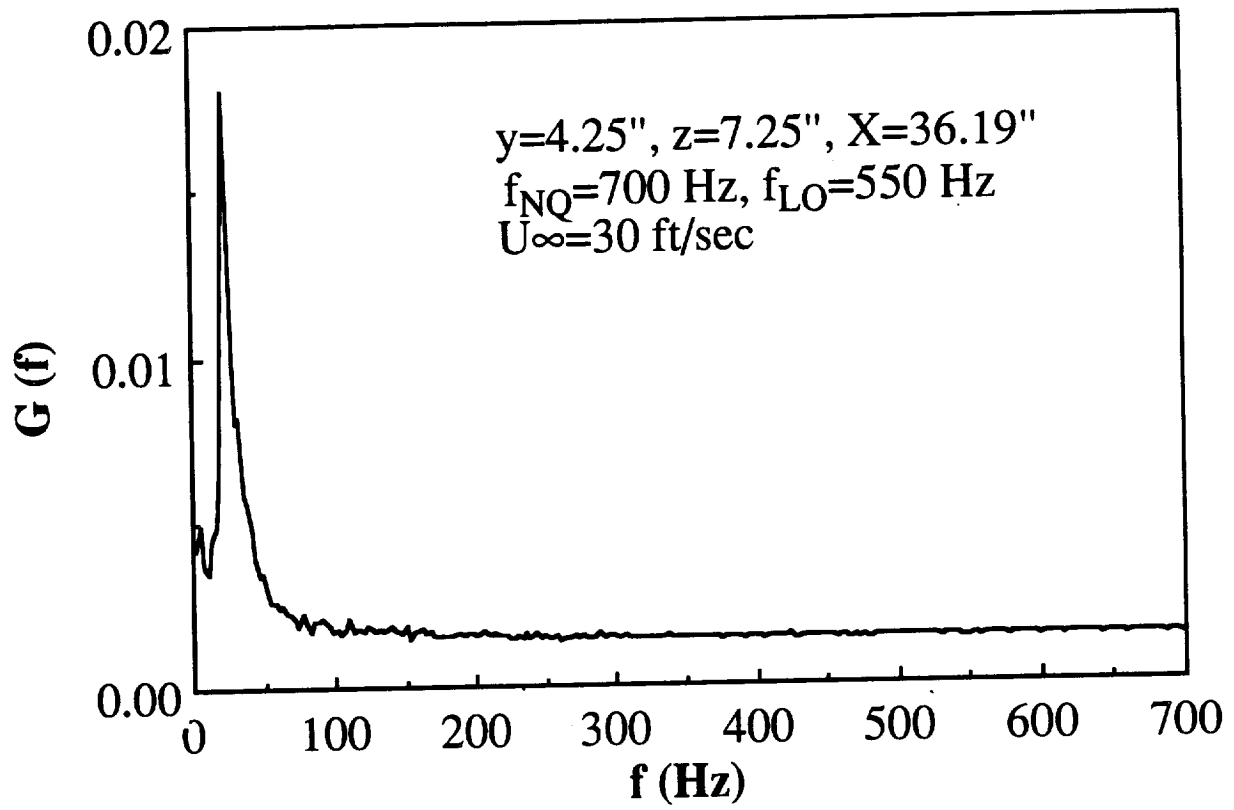
Fig.4.32b Velocity spectrum measured at HW station 1, z=7.25", U∞=30 ft/sec, α=25°
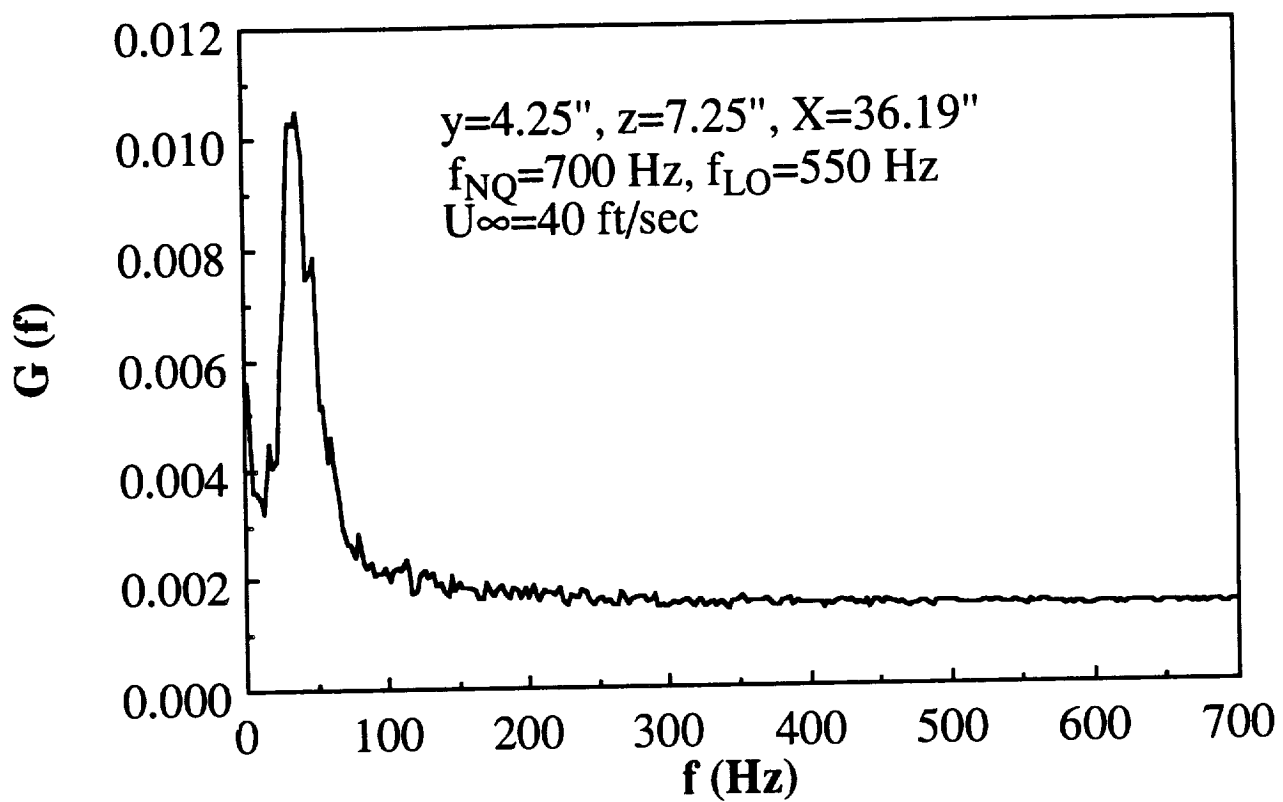
Fig.4.32c   Velocity spectrum measured at HW station 1, z=7.25", U∞=40 ft/sec, α=25°
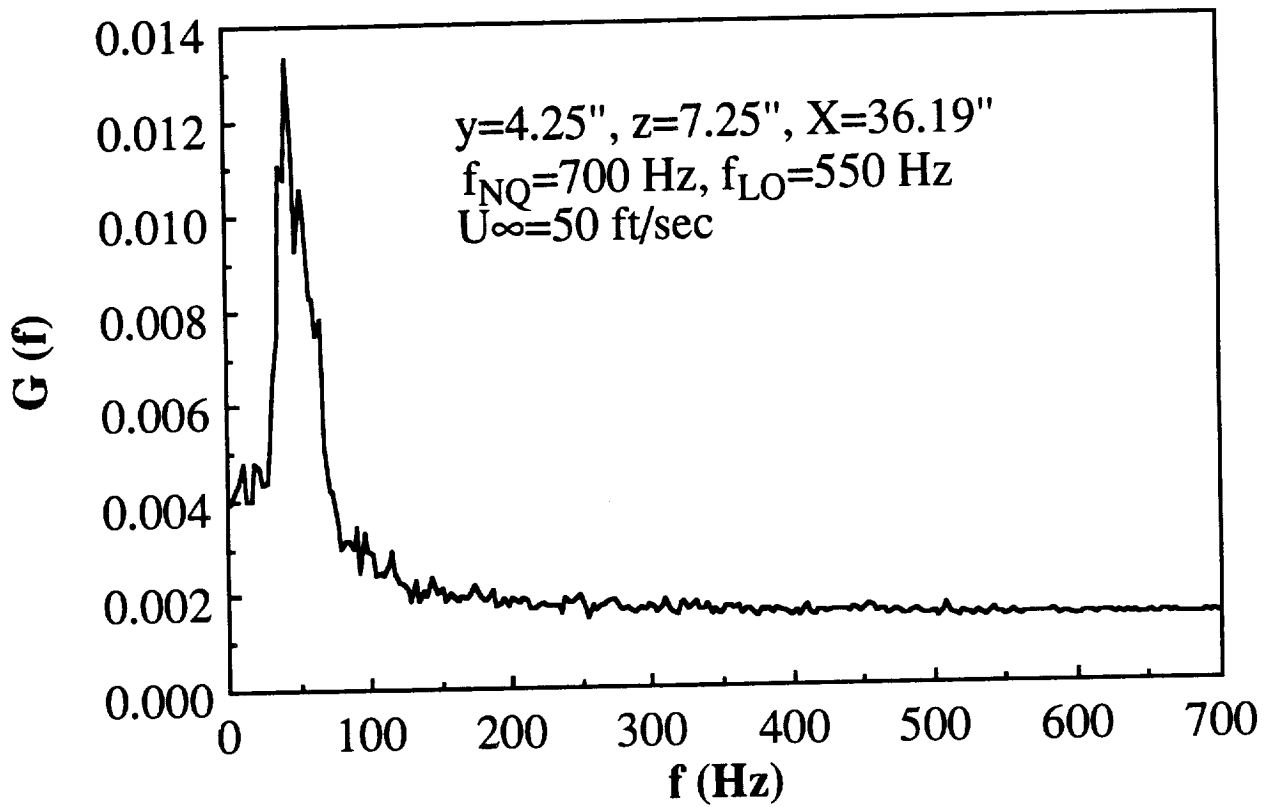
Fig.4.32d   Velocity spectrum measured at HW station 1, z=7.25", U∞=50 ft/sec, α=25°
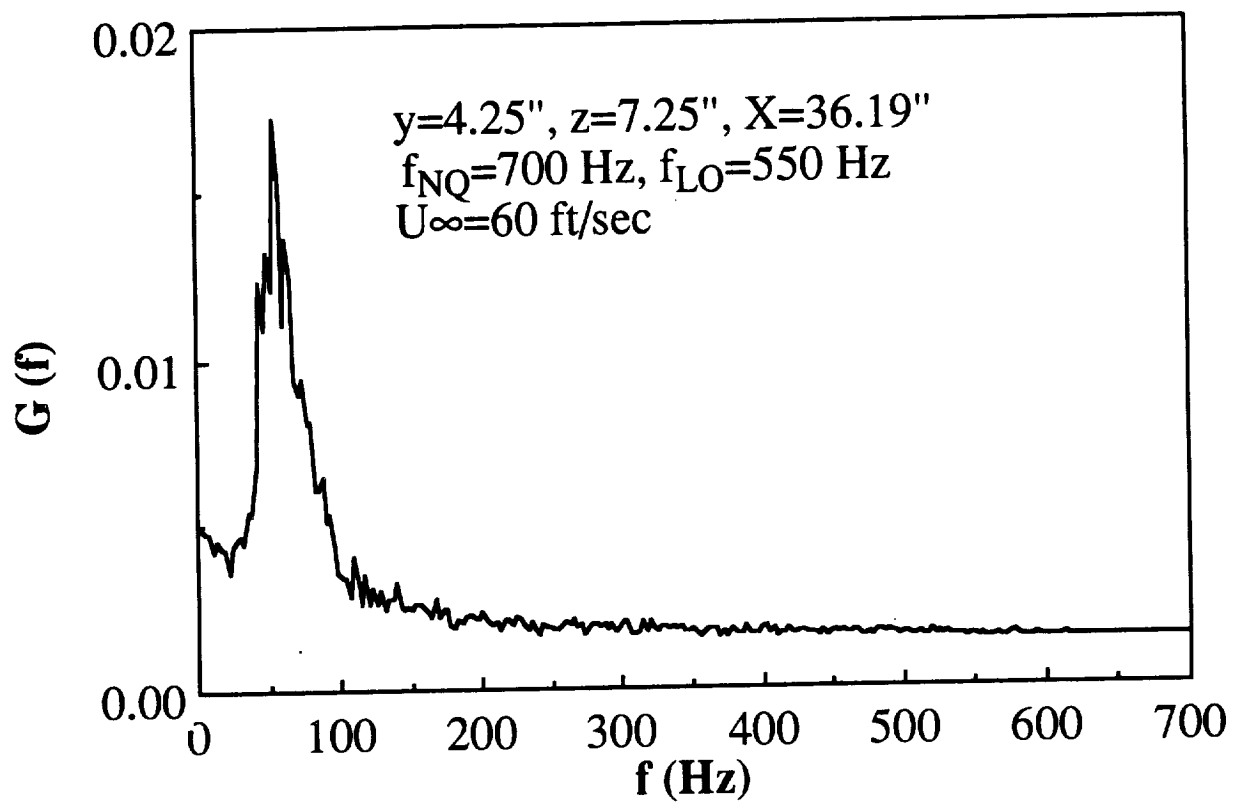
Fig.4.32e   Velocity spectrum measured at HW station 1, z=7.25", U∞=60 ft/sec, α=25°

y=4.25", z=7.25", X=36.19"
f_{NQ}=700 Hz, f_{LO}=550 Hz
U∞=70 ft/sec
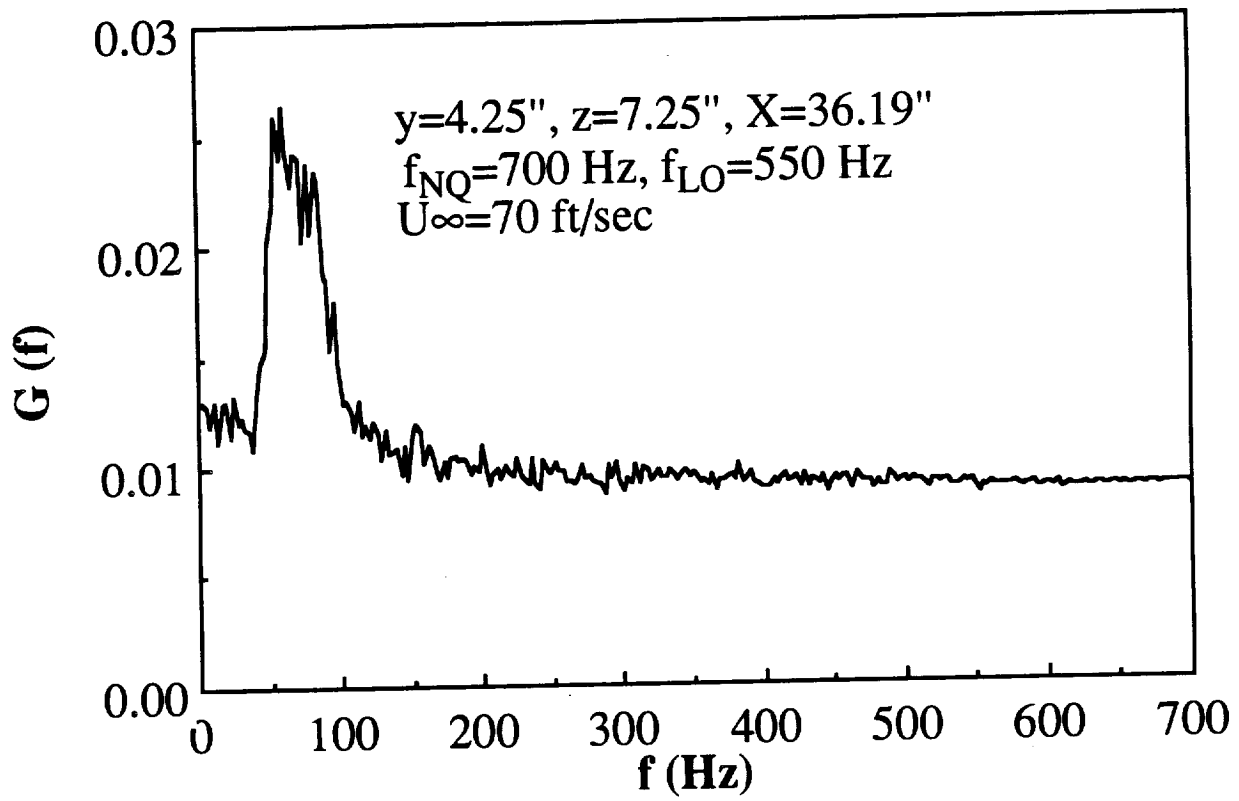
Fig.4.32f   Velocity spectrum measured at HW station 1, z=7.25", U∞=70 ft/sec, α=25°

y=4.25", z=7.25", X=36.19"
f_{NQ}=700 Hz, f_{LO}=550 Hz
U∞=80 ft/sec
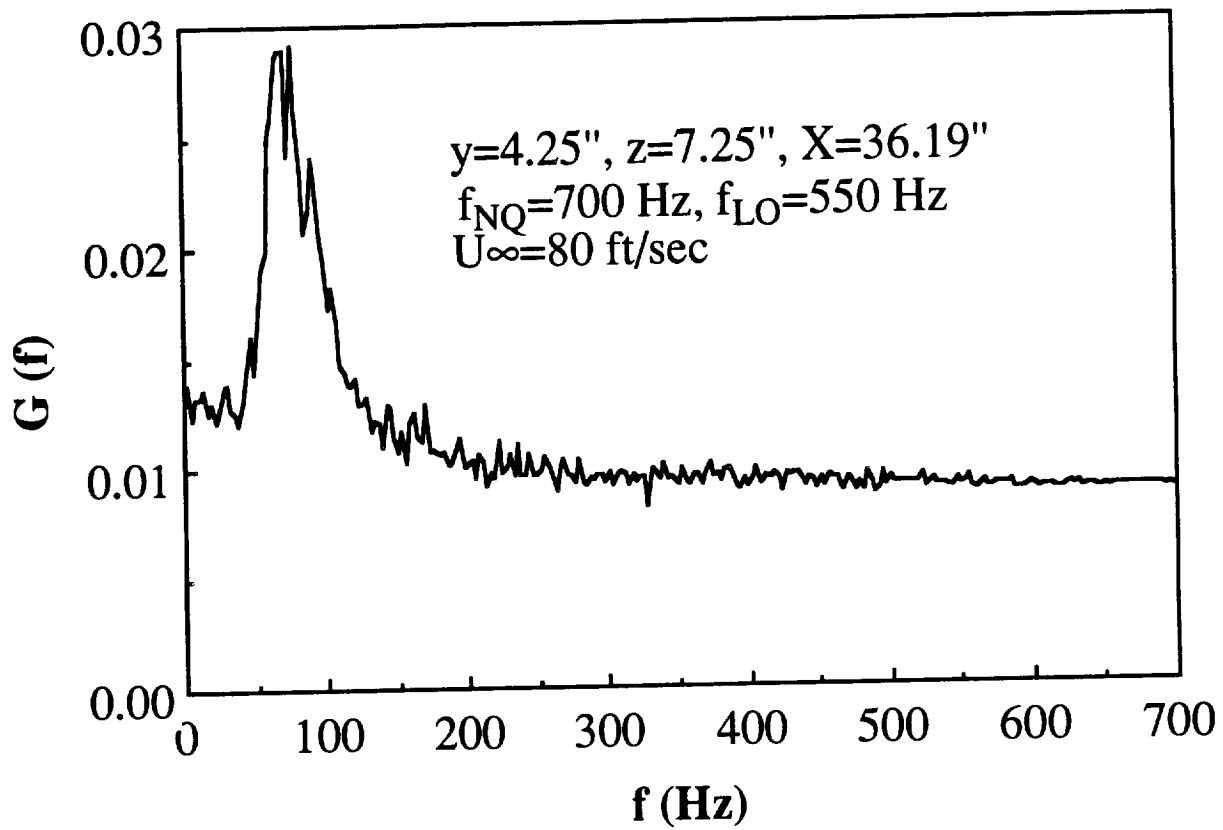
Fig.4.32g   Velocity spectrum measured at HW station 1, z=7.25", U∞=80 ft/sec, α=25°
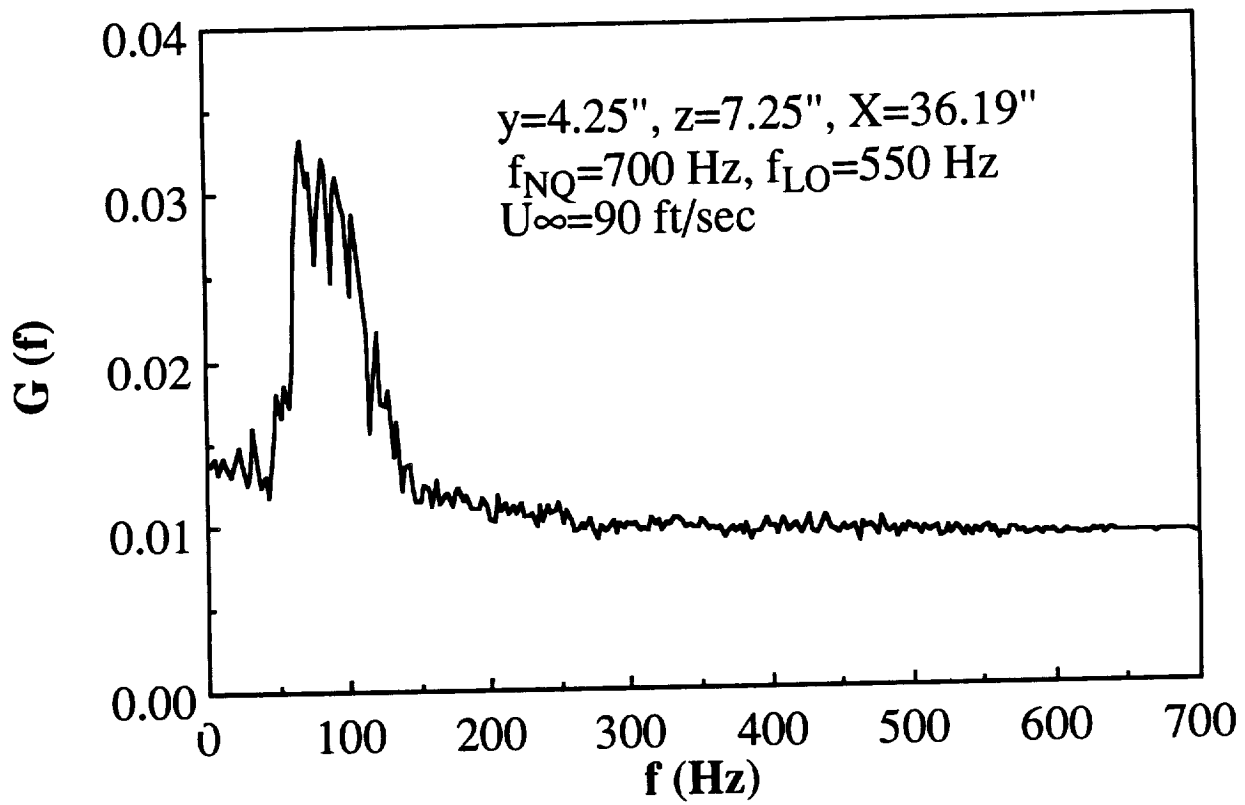
Fig.4.32h   Velocity spectrum measured at HW station 1, z=7.25", U∞=90 ft/sec, α=25°
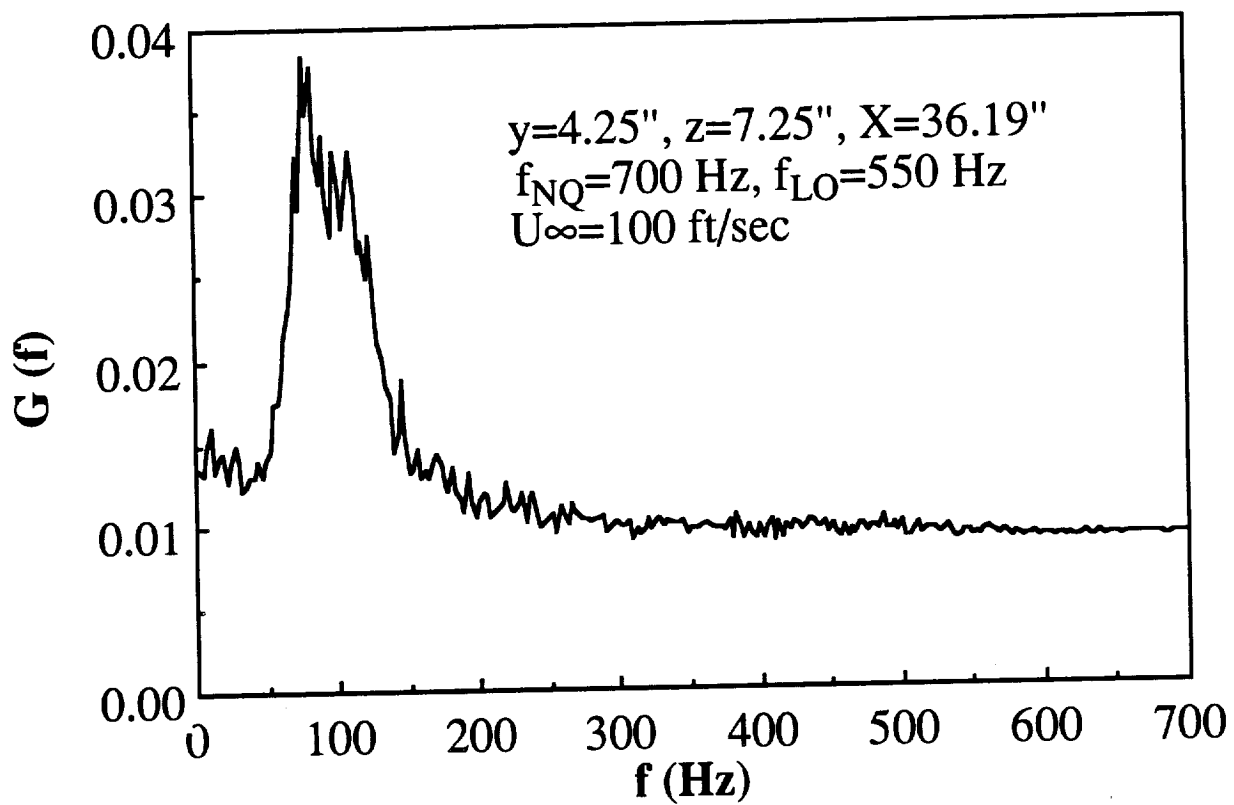
Fig.4.32i Velocity spectrum measured at HW station 1, z=7.25", U∞=100 ft/sec, α=25°
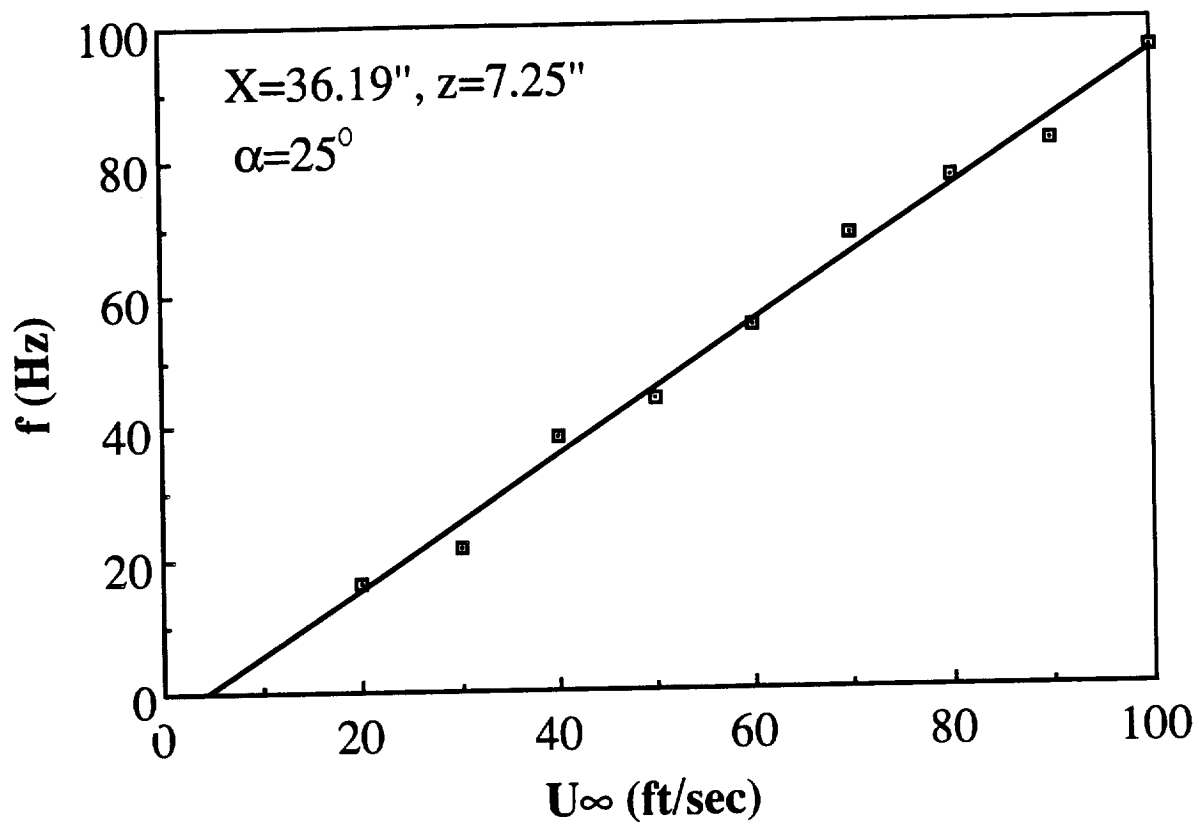
Fig.4.33 Variation of dominant frequency with freestream speed at HW station 1, z=7.25", α=25°

Fig.4.34a Velocity spectrum measured at HW station 1, z=6.25", U_∞=50 ft/sec, α=10°
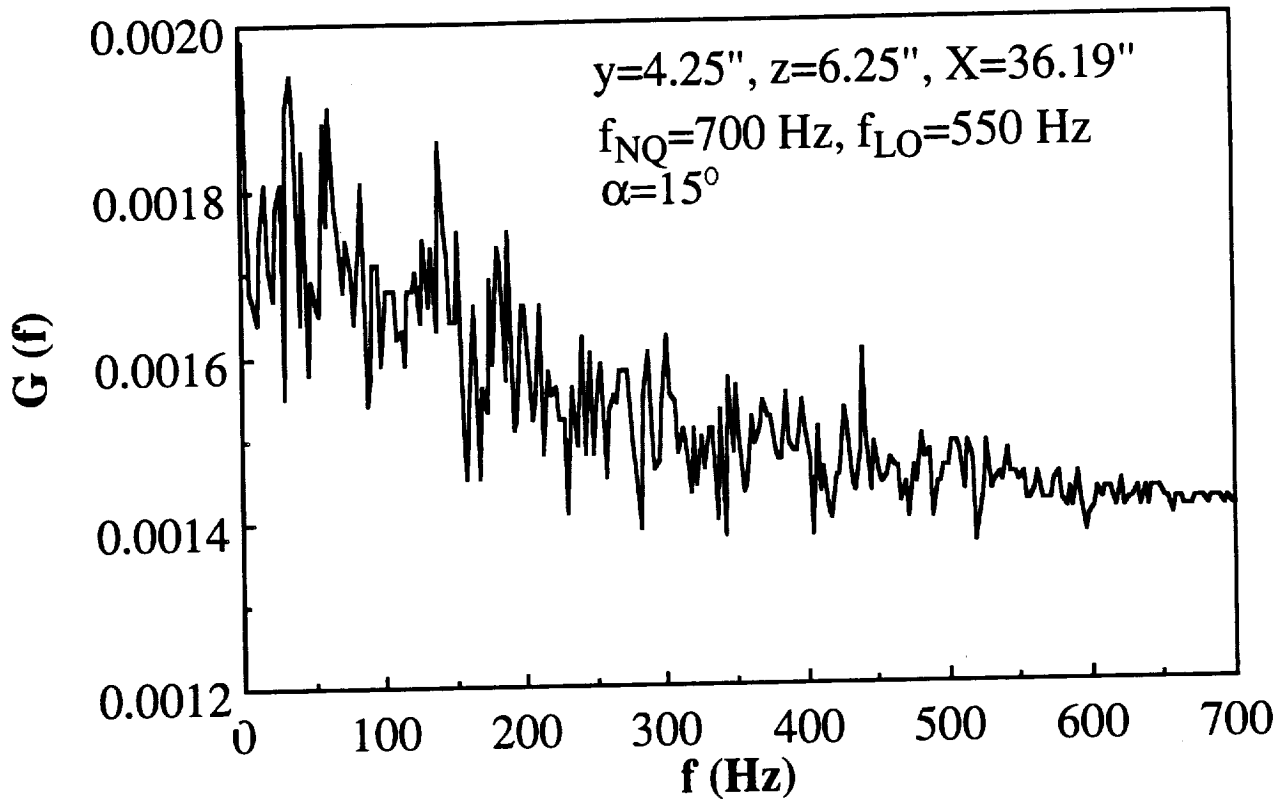
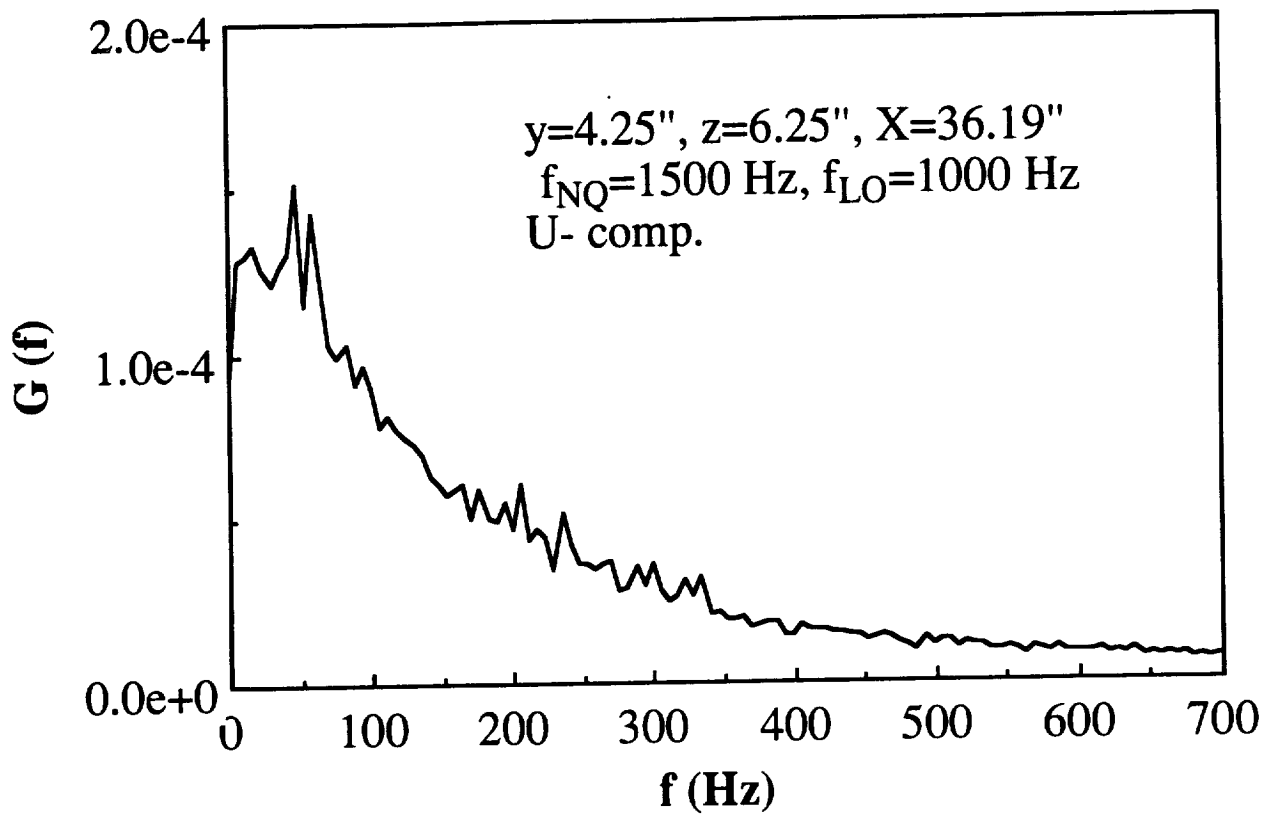Fig.4.34b Velocity spectrum measured at HW station 1, z=6.25", U_∞=50 ft/sec, α=15°
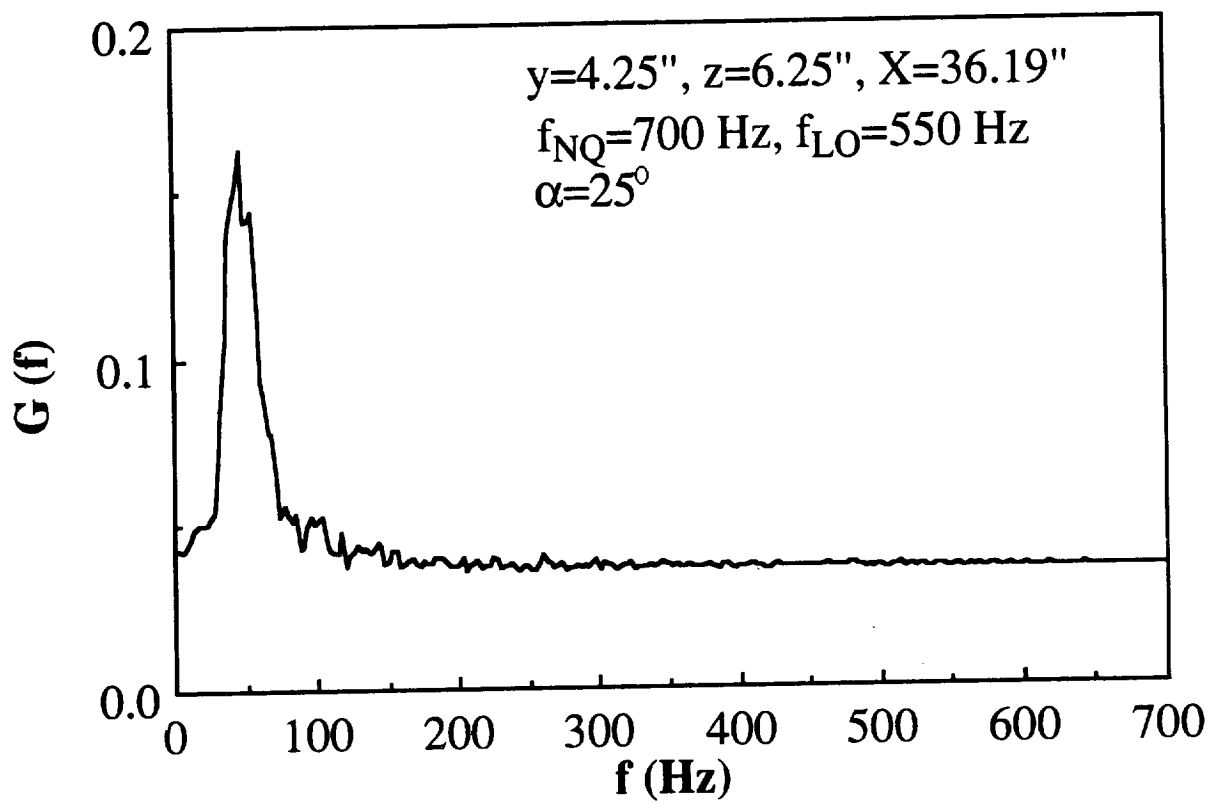
Fig.4.34c   Velocity spectrum measured at HW station 1, z=6.25", U∞=50 ft/sec,

α=25°
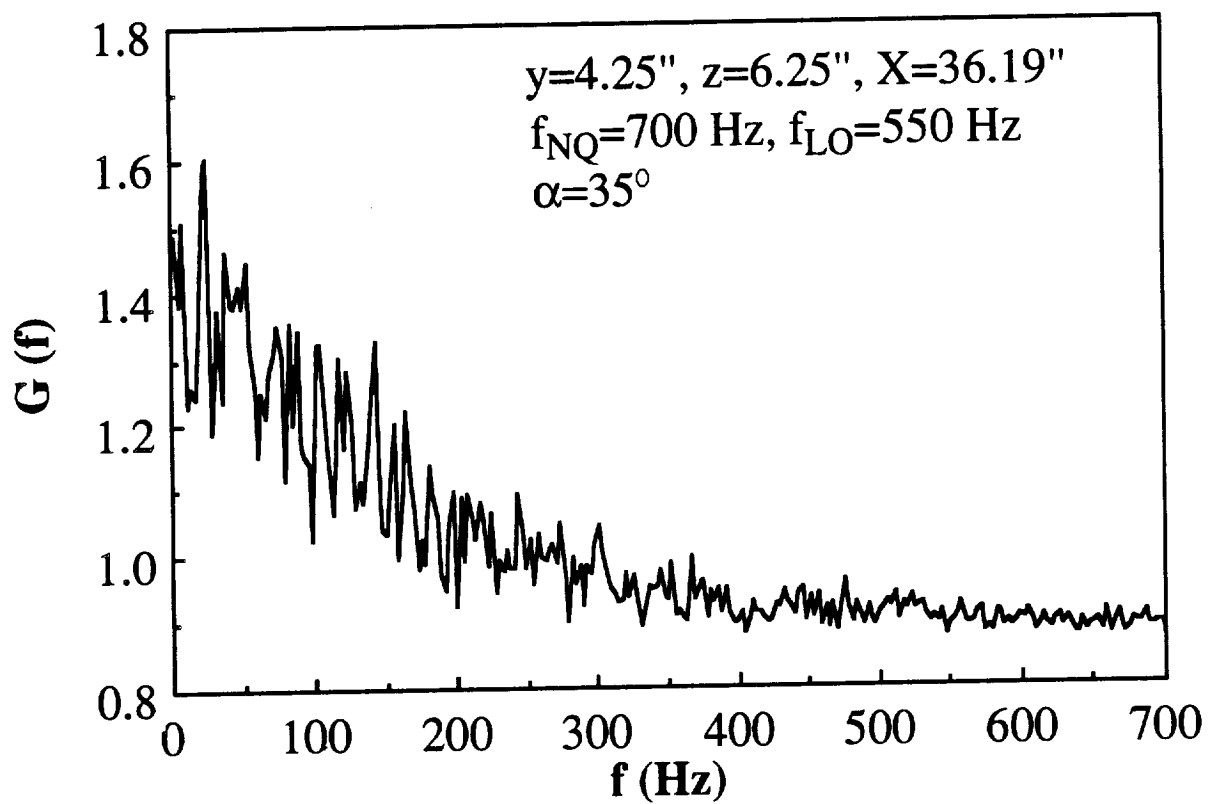
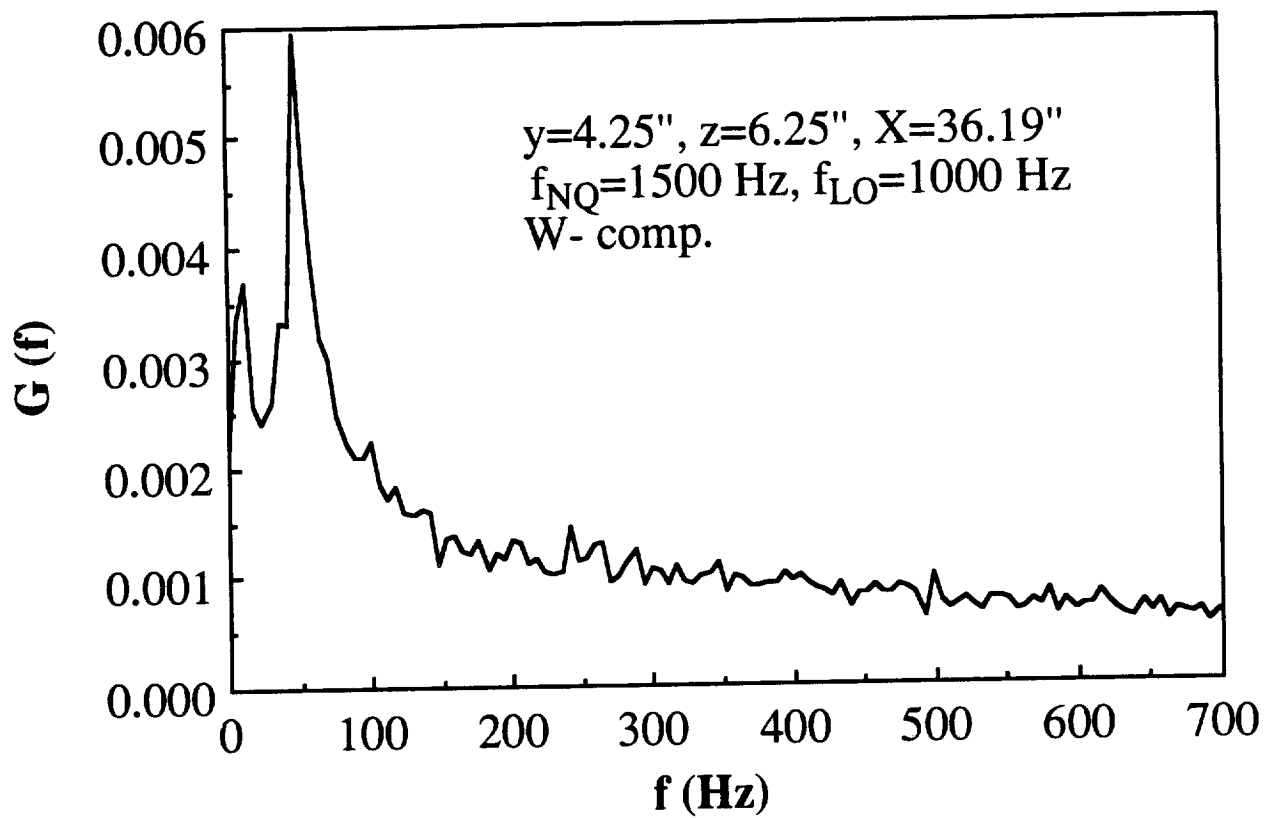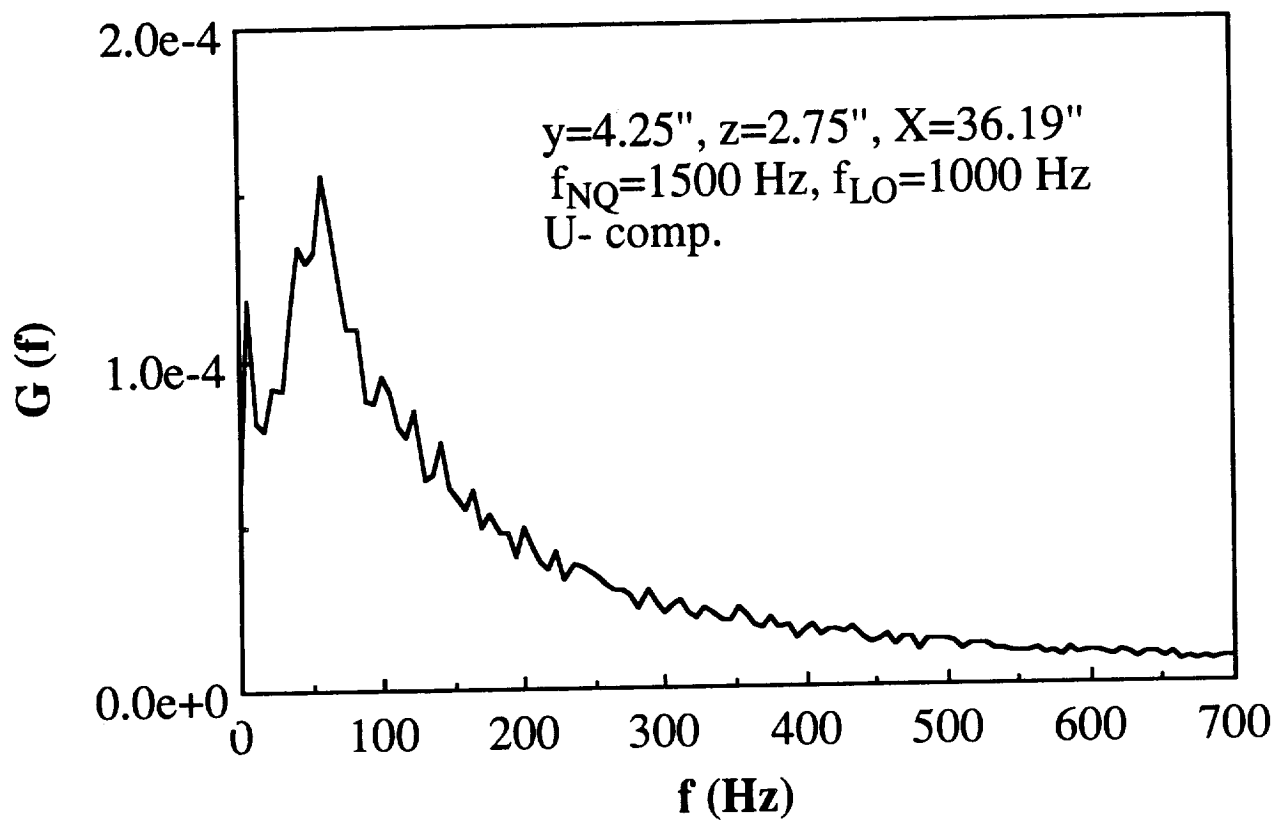Fig.4.34d   Velocity spectrum measured at HW station 1, z=6.25", U∞=50 ft/sec, α=35°

Fig.4.35a   Velocity spectrum obtained from LDV signal at HW station 1, z=6.25", α=25°, U-component
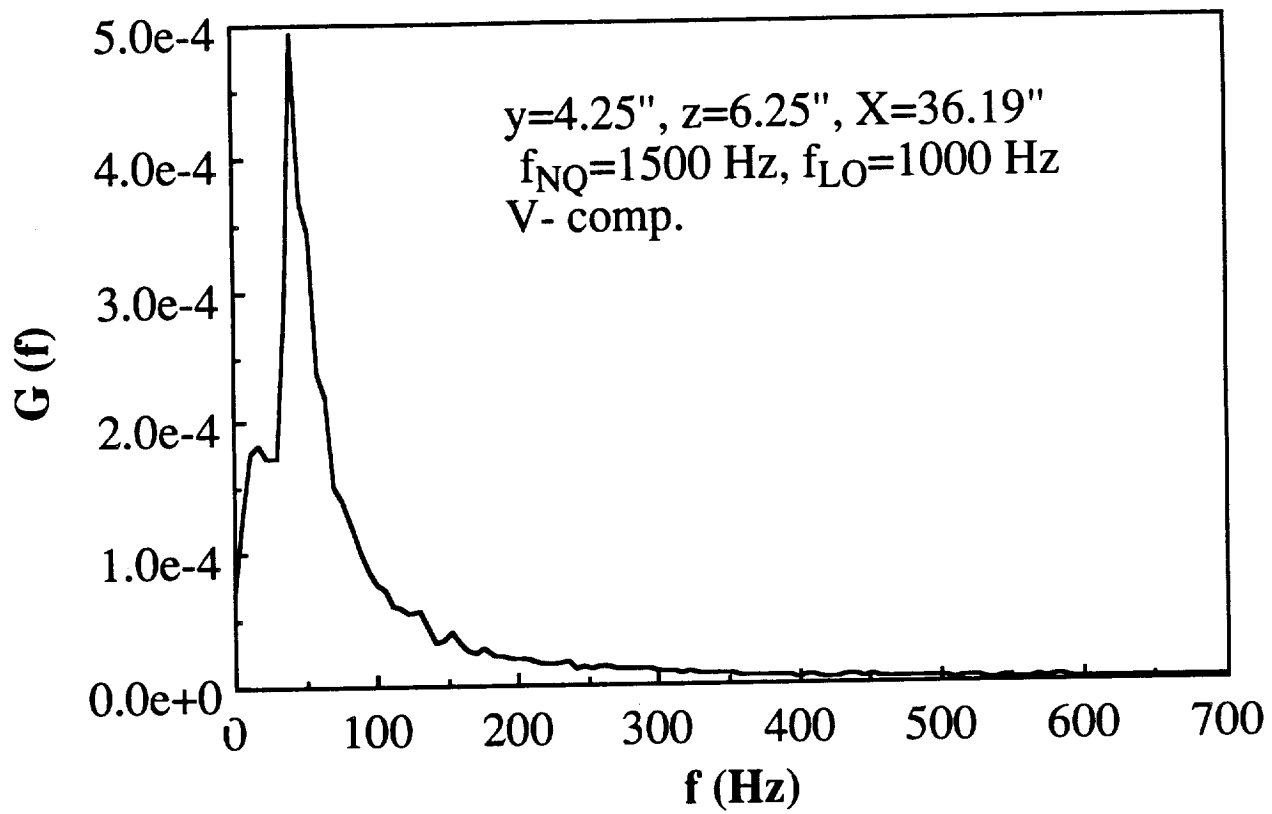
Fig.4.35b Velocity spectrum obtained from LDV signal at HW station 1,
z=6.25", α=25°, V-component

Fig.4.35c Velocity spectrum obtained from LDV signal at HW station 1,
z=6.25", α=25°, W-component

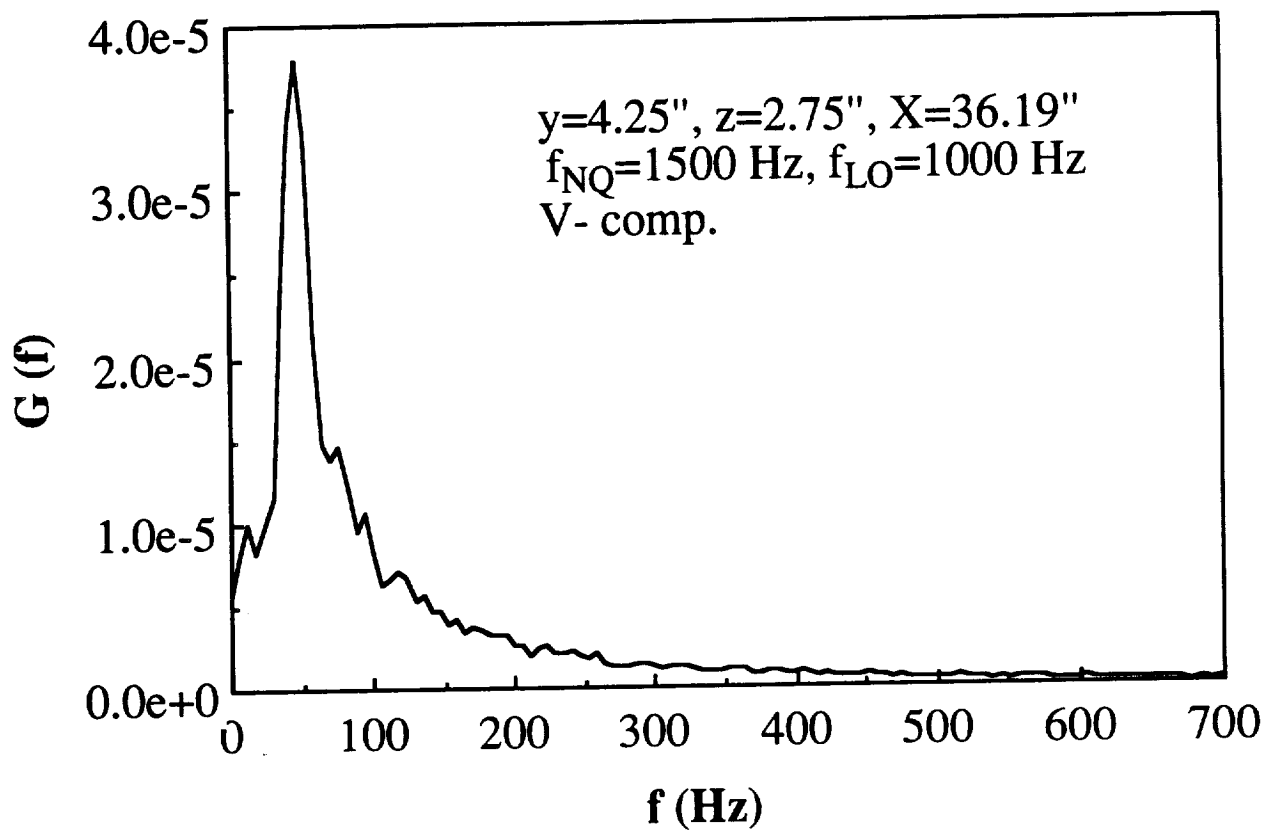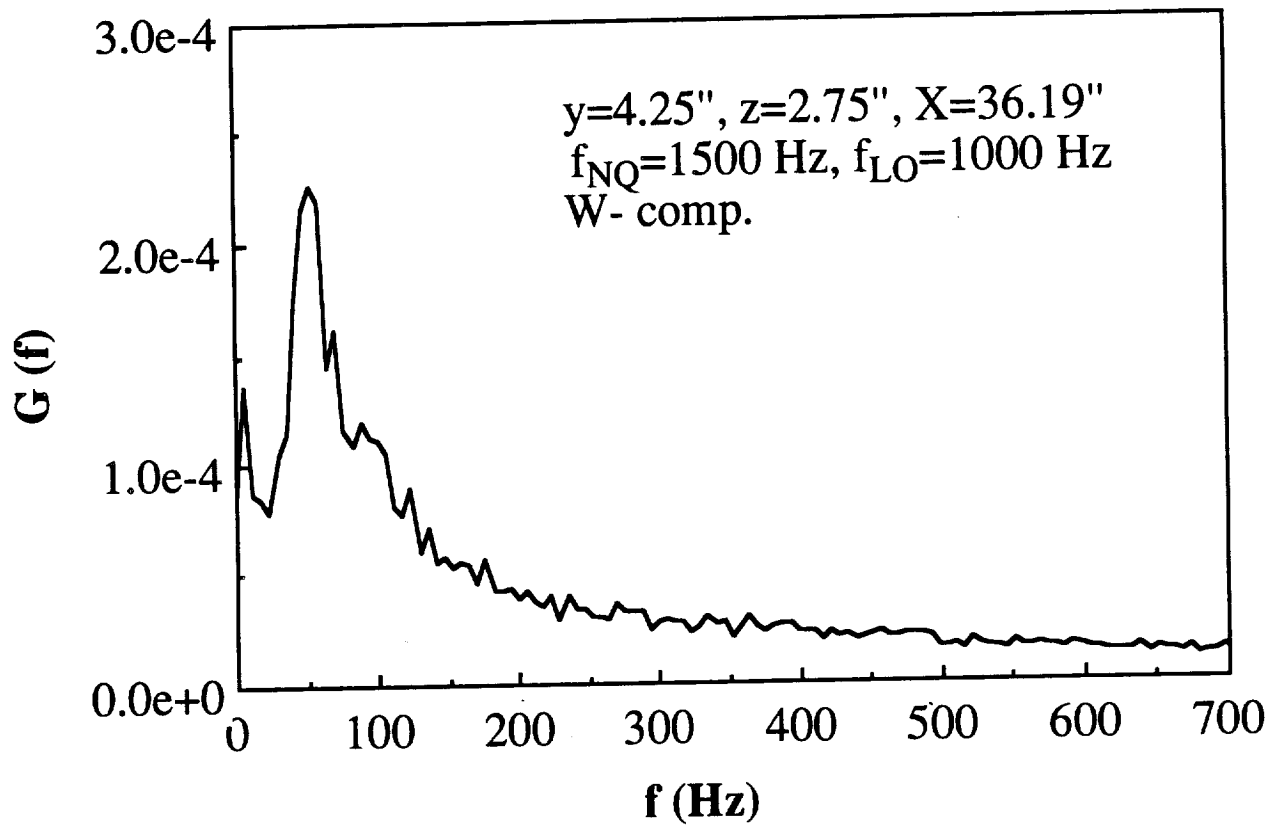Fig.4.36a   Velocity spectrum obtained from LDV signal at HW station 1, z=2.25", α=25°, U-component

Fig.4.36b   Velocity spectrum obtained from LDV signal at HW station 1,
z=2.25", α=25°, V-component

Fig.4.36c   Velocity spectrum obtained from LDV signal at HW station 1, z=2.25", α=25°, W-component